Title
Ice-Crystallization Kinetics during Fuel-Cell Cold-Start

Author
Dursch, Thomas James

Publication Date
2014

Peer reviewed|Thesis/dissertation

Ice-Crystallization Kinetics during Fuel-Cell Cold-Start

By

Thomas James Dursch Jr.

A dissertation submitted in partial satisfaction of the

requirements for the degree of

Doctor of Philosophy

in

Chemical Engineering

in the

Graduate Division

of the

University of California, Berkeley

Committee in charge:

Professor Clayton Radke, Chair
Professor John Newman
Professor Stephen Morris

Spring 2014

Abstract

Ice-Crystallization Kinetics during Fuel-Cell Cold-Start

by

Thomas James Dursch Jr.

Doctor of Philosophy in Chemical Engineering

University of California, Berkeley

Professor Clayton J. Radke, Chair

Proton-exchange-membrane fuel cells (PEMFCs) show promise in automotive applications because of their high efficiency, high power density, and potentially low emissions. To be successful in automobiles, PEMFCs must permit rapid startup with minimal energy from subfreezing temperatures, known as cold-start. In a PEMFC, reduction of oxygen to water occurs in the cathode catalyst layer (CL). Under subfreezing conditions, water generated during startup solidifies and hinders access of gaseous oxygen to the catalytic sites in the cathode CL, severely inhibiting cell performance and potentially causing cell failure. Achieving cold-start is difficult in practice, due to potential flooding, sluggish reaction kinetics, durability loss, and rapid ice crystallization. Currently, however, few studies focus on the fundamentals of ice crystallization during cold-start. Elucidation of the mechanisms and kinetics of ice formation within PEMFC porous media is, therefore, critical to successful cell startup and high performance at low temperatures.

First, an experimental method is presented for obtaining isothermal ice-crystallization kinetics in water-saturated gas-diffusion layers (GDLs). Ice formation is initially studied in the GDL because this layer retains a significant amount of product water during cold-start. Isothermal ice-crystallization and ice-nucleation rates are obtained in commercial Toray GDLs as functions of subcooling using differential scanning calorimetry (DSC). A nonlinear ice-crystallization rate expression is developed using Johnson-Mehl-Avrami-Kolmogorov (JMAK) theory, in which the heat-transfer-limited growth rate is determined from the moving-boundary Stefan problem. Predicted ice-crystallization rates are in excellent agreement with experiment. A validated rate expression is thus available for predicting ice-crystallization kinetics in GDLs.

Ice-crystallization kinetics is also considered under experimental settings similar to real PEMFC operating conditions where ice invariably forms non-isothermally. Non-isothermal ice-crystallization rates and ice-crystallization temperatures are obtained in water-saturated GDLs as a function of cooling rate. Our previously developed ice-crystallization rate expression is extended to non-isothermal crystallization to predict ice-crystallization kinetics at various cooling rates. For non-isothermal ice formation, we find that cooling rate has a negligible effect on the crystallization rate when crystallization times are much faster than the time to decrease the sample temperature by the subcooling. Therefore, a pseudo-isothermal method is proposed for non-isothermal crystallization kinetics using isothermal crystallization kinetics evaluated at the non-isothermal crystallization temperature.

Catalyst layers also retain a significant amount of product water during cold-start. Accordingly, ice nucleation and growth in PEMFC CLs are investigated using isothermal DSC and compared to isothermal galvanostatic membrane-electrode assembly (MEA) cold-starts. Measured ice-crystallization and ice-nucleation rates follow expected trends from classical nucleation theory. Following our previous approach, a quantitative nonlinear ice-crystallization rate expression is developed from the JMAK framework. To validate ice-crystallization kinetics within PEMFCs, we further measure and predict MEA cell-failure time during isothermal galvanostatic cold-start. Using a simplified PEMFC isothermal cold-start continuum model, MEA cell-failure times predicted using the newly obtained rate expression are compared to that predicted using a traditional thermodynamics-based approach. From this comparison, conditions are identified under which including ice-crystallization kinetics is critical and to elucidate the impact of freezing kinetics on low-temperature PEMFC operation.

During cold-start, the time for recovering cell performance strongly depends on the rate of melting residual ice by reactive heat generation. Non-isothermal ice melting in water-saturated GDLs is investigated using DSC with various heating rates. In all cases, ice-melting times decrease nonlinearly with increasing heating rate, whereas melting temperatures remain near the equilibrium melting temperature of bulk ice, demonstrating that melting is thermodynamic-based with a rate limited by heat transfer. Ice-melting endotherms are predicted from overall DSC energy balances coupled with a moving-boundary Stefan problem, where an ice-melting front within a GDL propagates with volume-averaged properties through an effective medium. Agreement between theory and experiment is excellent. Furthermore, an analytical expression is obtained for ice-melting time. Significantly, the new expression elucidates parameters controlling ice melting and allows for better design of both GDL materials and heating strategies to enhance the success of PEMFC cold-start.

Table of Contents

Chapter 5. Non-Isothermal Melting of Ice in the Gas-Diffusion Layer of a Proton-Exchange-Membrane Fuel Cell

Chapter 6. Conclusions

List of Figures

List of Tables

Acknowledgements

When applying to graduate school in the final quarter of 2008, I wrote in my personal statement:

> *"The desire to understand has been my motivation during my years as an undergraduate chemical engineer. My eagerness to learn has given me both a sense of accomplishment and fulfillment. It is from this passion for knowledge that my life-long objectives were developed. As a student in his final year of study at the University of Pennsylvania, I am seeking a doctoral degree in order to make possible my long-term goal: to conduct research and teach."*

Five years later, my career aspirations remain the same, but my sense of direction is even clearer. My time in graduate school has cultivated an even greater feeling of scientific curiosity, and has presented unique opportunities to both learn and teach. I am pleased with my choice to attend UC Berkeley. I am confident that I will remain in academia. I am eternally grateful to both family and friends who made my life so clear-cut and enjoyable; you have been supportive, loving, caring, critical, and thoughtful – more so than I ever had hoped. In this section, I briefly acknowledge family and friends who have, with sincere conviction, played major roles in shaping my career.

I thank my family (i.e., my mom, dad, and two brothers) and my girlfriend, Gina Noh, for being incredibly understanding and endlessly supportive. I appreciate you answering the phone everyday when I inevitably call to discuss teaching, learning, or science. I thank Radke and Weber group members, past and present, for their thoughtful discussions, careful observation, and support. Specical thanks to Colin Cerretani, Tatyana Svitova, Ahmet Kusoglu, David Liu, and Chengchun Peng, the latter two with whom I collaborate regularly. You all make research entertaining and enjoyable and I have learned much from you. I thank the numerous gifted undergraduate students I have had the pleasure of working alongside of, including several who have significantly contributed to my thesis work (i.e., Monica Ciontea, Gregory Trigub, and Jianfeng Liu). I also thank Prof. Prausnitz not only for his scholarship, but also for his continual guidance and mentorship.

Finally, I thank my advisers Clayton Radke and Adam Weber for all of the time, effort, and thought spent over the past five years. I could not have asked for a better adviser duo. Here, I briefly discuss them. During my time in graduate school, I have become incredibly familiar with Adam as a scholar, mentor, and friend. His leadership and collaborative nature is both admiring and remarkable. I am continually amazed by Adam's ability to effectively straddle two unique scientific fields: electrochemistry and polymer membranes. I truly appreciate the effort he has expended on developing my career. Undoubtedly, I look forward to continuing working with Adam in the future.

Clay's knack for devising physical pictures to explain importance scientific problems is stunning. Chapters 2-6 highlight this remarkable skill that I hope to evolve throughout the course

of my career. I am very fortunate to have had Clay as a thesis adviser. His passion and love for teaching is nothing short of inspirational. I wish to say thanks by ending with an excerpt of a nomination letter that I wrote for Clay summzaring what I have learned about mentorship. The letter was for the Carol D. Soc Distinguished Graduate Student Mentoring Award:

> *"Over the past few years, Prof. Radke has regularly demonstrated that he is an exceptional mentor. In my opinion, he is an excellent model for an advisor in the Department of Chemical & Biomolecular Engineering. He is a highly dedicated leader, who motivates his students to strive for excellence; a powerful communicator, who possesses the ability to make complex subjects simple; and an inspiration, who embodies incredible enthusiasm, care, and support. In spite of these incredible gifts, he is a very approachable person who loves to share his extensive knowledge with others, especially his students.*
>
> *As aspiring faculty members, I can say with great certainty that we now understand the attributes of an outstanding mentor."*

Chapter 1

Introduction

1.1. Motivation and Goals

Proton-exchange-membrane fuel cells (PEMFCs) show promise in automotive applications because of their high efficiency, high power density, and potentially low emissions [1-4]. To be successful in automobiles, PEMFCs must permit rapid startup with minimal energy from subfreezing temperatures, known as cold-start [5-8]. In recent years, several cold-start requirements have been established by the Department of Energy [8]. Two key targets are that the PEMFC must successfully start unassisted (e.g., no imposed heating) from: (1) –40 °C, and (2) –20 °C to 50 % net power within 30 s. Achieving such startup is difficult in practice, due to potential flooding, sluggish reaction kinetics, durability loss, and rapid ice crystallization [5-8]. Currently, few studies focus on the fundamentals of ice crystallization during cold-start. Clearly, elucidation of the mechanisms and kinetics of ice formation in PEMFC porous media is necessary. Such knowledge guides the development of both procedural strategies and advanced materials for improved cell performance at subfreezing temperatures.

This dissertation focuses on two central issues: (1) the rate of ice crystallization in PEMFC porous media, and (2) the role of ice-crystallization kinetics during PEMFC cold-start. The first question asks what parameters (e.g., temperature, wettability, and cooling rate) govern the kinetics of ice crystallization in water-saturated PEMFC porous media and what is the governing rate expression. The second question asks what is the impact of ice-crystallization kinetics on low-temperature PEMFC operation and under which cold-start conditions is ice-crystallization kinetics critical. To appreciate these two questions, the following sections provide background information on fuel-cell cold-start, as well as a brief overview of previous research.

1.2. Proton-Exchange-Membrane Fuel Cells (PEMFCs)

Understanding ice crystallization during cold-start requires basic knowledge of fuel cells. This section discusses traditional PEMFC materials and reviews the underlying principles of PEMFC operation under normal, low, and subfreezing temperatures.

1.2.1. Background:

PEMFCs are electrochemical cells that generate electricity by consuming fuel (e.g., hydrogen or methanol) and oxygen, forming water and heat as byproducts. Commonly, fuel cells are stacked in series to increase the output voltage to that specified by the desired application. Here, discussion is limited to single-cell PEMFCs fueled by hydrogen gas. Detailed discussion of PEMFC stacks is found elsewhere [9,10].

Figure 1.1 displays a schematic of a typical PEMFC. The PEMFC consists of a membrane-electrode assembly (MEA) that is sandwiched between two electrically-conductive bipolar plates engraved with single- or multi-pass channels for gas flow (i.e., gas channels, GCs) [11]. The MEA consists of anode and cathode diffusion media (DM) and catalyst layers (CLs), as well as a proton-exchange membrane (PEM). In the anode, supplied hydrogen gas is oxidized to protons and electrons in the CL, often by a platinum catalyst. Generated protons are conducted through the PEM to the cathode, while electrons are forced to travel through an external circuit, thereby producing an electric current. In the cathode, supplied oxygen, typically

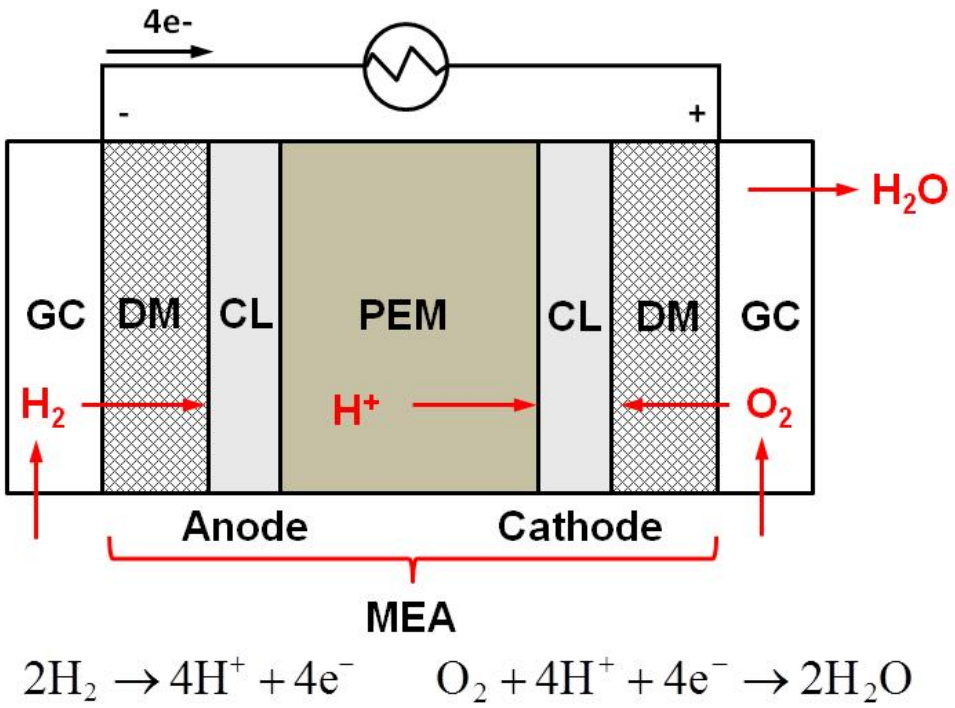

Figure 1.1. Schematic for a single conventional proton-exchange-membrane fuel cell. GC, DM, CL, PEM, and MEA label the gas channels, diffusion media, catalyst layers, proton-exchange membrane, and membrane-electrode assembly, respectively. Drawing is not to scale.

in the form of air, combines with protons to form byproduct water in the CL. For reference, Figure 1.1 reports the anode and cathode half-reactions.

Figure 1.2 shows a schematic of a conventional MEA cathode, which highlights the PEM, a highly-fluorinated membrane containing pendant sulfonic acid groups for enhanced proton conductivity; the CL, irregularly-shaped carbon aggregates with dispersed platinum particles; and the DM, which is an electrically conductive single- or double-layer used to facilitate gas transport to the CL [12]. Squiggly lines in the CL represent ionomer added for improved proton conductivity. Figure 1.2 displays a traditional single-layer DM consisting of only a gas-diffusion layer (GDL). Detailed discussion of bilayer DM (i.e., a GDL backed by a hydrophobic-rich microporous layer (MPL)) is found elsewhere [13].

1.2.2. Normal Operating Temperatures (*>60 °C*):

Fuel-cell performance is often characterized by a polarization curve, or a plot of cell potential versus current density (current normalized by cell active area). By way of example, Figure 1.3 displays a typical polarization curve predicted using a 0-d model by Balliet [14] for a PEMFC operated at a temperature of 65 °C. For reference, the cell power density is included on the secondary ordinate (cell power density, P, is given by: $P = Vi$, where V is cell potential and i is current density). As shown in Figure 1.3, the cell potential is less than the reversible cell potential due to irreversible losses that increase with increasing current density [12,14]. Often, the polarization curve is divided into three regions [12,14]. At low current densities, cell potential is dictated by kinetic losses stemming primarily from the high overpotential of the oxygen-reduction reaction. As current density increases, ohmic losses (e.g., ionic losses in the membrane) become increasingly important. At high current densities, mass-transport limitations contribute, as reactants are unable to reach catalytic sites in the CL. For example, reactant oxygen diffusion can be limited by flooding of the cathode by liquid water [12]. As discussed elsewere [14], power density often exhibits a maximum at high current densities (i.e., near the limiting current).

1.2.2. Low and Subfreezing Operating Temperatures (*<0 to 60 °C*):

Fuel-cell performance generally diminshes with decreasing operating temperature. To illustrate, Figure 1.4 shows polarization curves predicted using a 0-d model by Balliet [14] for a PEMFC operated at temperatures of -40, -20, 0, 20, 40, 60, and 80 °C. The non-monotonic decrease in power density with decreasing temperature is discussed elsewhere [14]. At lower temperatures (i.e., < 50 °C), cell performance decays primarly due to: (1) decreased kinetic rates of the oxygen reduction reaction; (2) decreased ionic conductivity in the catalyst ionomer and membrane; and (3) increased mass-transport limitations due to the presence of ice or flooding of the cathode by liquid water. As indicated in Figure 1.4, under subfreezing conditions, water can solidify to ice in the MEA, further inhibiting cell performance and, in many cases, causing cell failure [15-18].

1.3. PEMFC Cold-Start

1.3.1. Literature Review:

Because of performance loss and cell failure under subfreezing conditions, significant effort has been expended toward understanding cold-start fundamentals and improving PEMFC cold-start capability [6-8,14,15-32]. To date, experiments predominately focus on characterizing

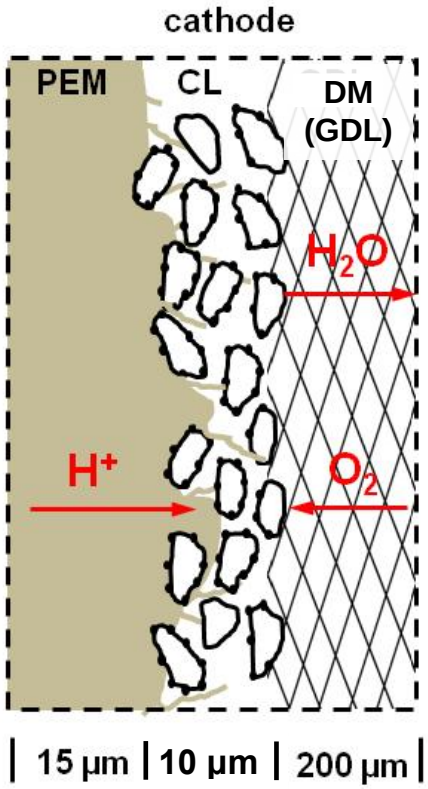

Figure 1.2. Schematic for a traditional cathode of a proton-exchange-membrane fuel cell. DM, CL, and PEM label the diffusion medium, catalyst layer, and proton-exchange membrane, respectively. Drawing is not to scale. Thicknesses are approximate.

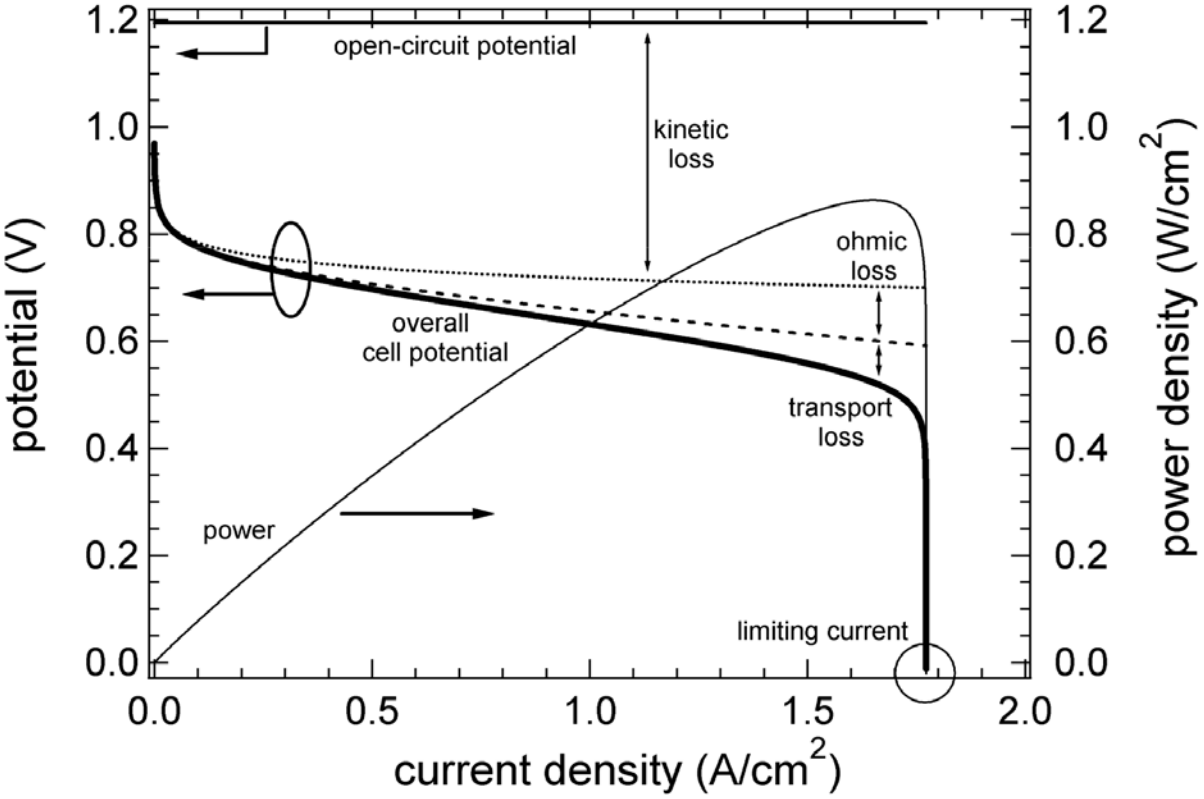

Figure 1.3. Predicted cell potential and power density as a function of current density for a PEMFC operated at a temperature of 65 °C. Fully humidified H_2/air operation is assumed, with 1 bar of total pressure for each gas. From Balliet [14] with permission.

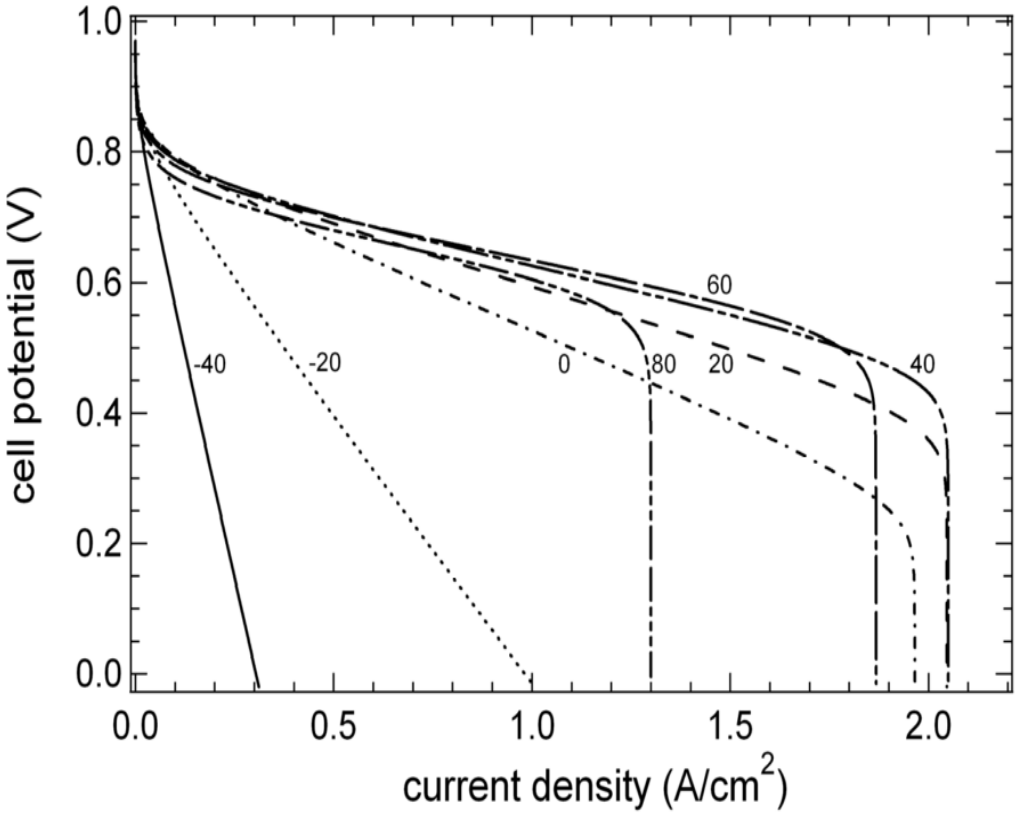

Figure 1.4. Predicted cell potential versus current density for a PEMFC at operating temperatures -40, -20, 0, 20, 40, 60, and 80 °C. Fully humidified H_2/air operation is assumed, with 1 bar of total pressure for each gas. From Balliet [14] with permission.

overall low-temperature cell performance [15-20]. In recent years, however, *in-situ* visualization and detection of ice formation within PEMFC porous media has progressed [21-26]. Visualization methods include neutron radiography [21,22], environmental scanning electron microscopy [23], visible imaging [24-26], and latent-heat detection with infrared thermography [24,25]. In all cases, generation of by-product water is observed in the subcooled state, particularly between –2 and –20 °C. Although the generated liquid water did not freeze instantaneously, the mechanism and kinetics of ice formation were unfortunately not investigated [21-26].

Over the past decade, several numerical continuum cold-start models have been developed [6,8,27-32]. To counter difficulties associated with cold-start, models emphasize both procedural strategies and materials design. For example, Balliet et al. [6,14,31] recommend higher potentials during startup to optimize performance at –20 °C, as well as increased water capacity or reservoirs (e.g., increased porosity). Numerous studies have also examined the stack-level thermal response during cold-start [27,32]. However, relatively few studies model production and flow of water within the PEMFC [27-30]. Early models assume that product water vapor instantaneously solidifies when the vapor partial pressure exceeds the saturation value [27-30]. As a result, they do not account for liquid water within the PEMFC. More recently, Jiao and Li [32] and Balliet et al. [6,14,31] extended cold-start models to include vapor, liquid, and solid phases of water within the PEMFC. The equilibrium freezing point of ice within the GDL, CL, and PEM is based on a characteristic pore size using the Gibbs-Thomson equation. Although the models include liquid water [6,14,31,32], they currently invoke thermodynamics-based freezing and circumvent the use of ice-crystallization kinetics, since at the time, none were available for PEMFC porous media.

1.3.2. Thesis Summary:

Elucidation of the mechanisms and kinetics of ice formation in PEMFC porous media is necessary. Despite significant attention to PEMFC cold-start, a basic understanding of ice-crystallization kinetics in PEMFC porous media is lacking. Chapters 2-4 advance knowledge of the mechanisms and kinetics of ice formation in water-saturated GDLs and CLs.

In Chapter 2, an experimental method is presented to quantify isothermal ice-crystallization kinetics in commercial GDLs. Following the experimental section, a validated nonlinear ice-crystallization rate expression is outlined following the Johnson-Mehl-Avrami-Kolmogorov (JMAK) framework [33-36], in which the heat-transfer-limited growth rate is determined from the moving-boundary Stefan problem [37]. The newly-proposed ice-crystallization rate expression agrees well with experiment.

Chapter 3 deals with non-isothermal ice crystallization in water-saturated GDLs. First, non-isothermal ice-crystallization kinetics is measured in commercial GDLs. The newly developed ice-crystallization rate expression is then extended to non-isothermal ice crystallization in GDLs. Here too, the ice-crystallization model agrees well with experiment. Following the theoretical section, a simplified pseudo-isothermal method is outlined for obtaining non-isothermal crystallization kinetics using isothermal crystallization kinetics evaluated at the non-isothermal crystallization temperature.

In Chapter 4, isothermal ice-crystallization kinetics is measured in water-saturated CLs with varying carbon-support materials, ionomer fraction, and platinum loading. Similar to Chapter 2, a quantitative nonlinear ice-crystallization rate expression is developed for ice

crystallization in CLs. To validate ice-crystallization kinetics in PEMFCs, in Chapter 4, cell-failure time is measured and predicted using a cold-start continuum model during isothermal galvanostatic cold-start. Cell-failure times predicted using ice-freezing kinetics are in good agreement with experiment. Significantly, the PEMFC continuum cold-start model demonstrates that ice-crystallization kinetics is critical when induction times are long (i.e., in the "nucleation-limited" regime for $273 > T > 263$ K).

During cold-start, the time for recovering cell performance strongly depends on the rate of melting residual ice by reactive heat generation. In Chapter 5, a method is presented to obtain non-isothermal ice-melting rates in water-saturated GDLs. Ice-melting endotherms are predicted from overall DSC energy balances coupled with a moving-boundary Stefan problem. Following the theoretical section, an analytical expression is derived for the ice-melting time. Significantly, the new expression elucidates parameters controlling ice melting and allows for better design of both GDL materials and heating strategies to enhance the success of PEMFC cold-start.

Chapter 6 of the dissertation concludes with a summary of the new findings on ice-crystallization kinetics during PEMFC cold-start. Broader impacts are discussed and future work is suggested.

1.4. References

[1] V. Mehta, J.S. Cooper, Review and analysis of PEM fuel cell design and manufacturing, J. Power Sources 114 (2003) 32-53.

[2] B. Smitha, S. Sridhar, A.A. Khan, Solid polymer electrolyte membranes for fuel cell applications - a review, J. Membrane Sci. 259 (2005) 10-26.

[3] H. Li, Y. Tang, Z. Wang, Z. Shi, S. Wu, D. Song et al., A review of water flooding issues in the proton exchange membrane fuel cell, J. Power Sources 178 (2008) 103-117.

[4] W. Schmittinger, A. Vahidi, A review of the main parameters influencing long-term performance and durability of PEM fuel cells, J. Power Sources 180 (2008) 1-14.

[5] Hydrogen, Fuel Cells & Infrastructure Technologies Program; Multi-Year Research, Development and Demonstration Plan, U.S. Department of Energy, 2007.

[6] R. Balliet, J. Newman, Cold start of a polymer-electrolyte fuel cell I. Development of a two-dimensional model, J. Electrochem. Soc. 158 (2011) B927-B938.

[7] K. Tajiri, Y. Tabuchi, F. Kagami, S. Takahashi, K. Yoshizawa, C.Y. Wang, Effects of operating and design parameters on PEFC cold start, J. Power Sources 165 (2007) 279-286.

[8] T.J. Dursch, G.J. Trigub, R. Lujan, J.F. Liu, R. Mukundan, C.J. Radke, A.Z. Weber, Ice-crystallization kinetics in the catalyst layer of a proton-exchange-membrane fuel cell, J. Electrochem. Soc. 161 (2014) F199-F207.

[9] R. Jiang, D. Chu, Stack design and performance of polymer electrolyte membrane fuel cells, J. Power Sources 93 (2001) 25-31.

[10] S.G. Kandlikar, Z. Lu, Thermal management issues in a PEMFC stack - a brief review of current status, Appl. Thermal Eng. 29 (2009) 1276-1280.

[11] X. Li, I. Sabir, Review of bipolar plates in PEM fuel cells: flow-field designs, Int. J. Hydrogen Energy 30 (2005) 359-371.

[12] A.Z. Weber, J. Newman, Modeling transport in polymer-electrolyte fuel cells, Chem. Rev. 104 (2004) 4679-4726.

[13] A.Z. Weber, J. Newman, Effects of microporous layers in polymer electrolyte fuel cells, J. Electrochem. Soc. 152 (2005) A677-A688.

[14] R. Balliet, Modeling cold-start in a polymer-electrolyte fuel cell, PhD thesis, University of California, Berkeley, CA, 2010, chapter 1.

[15] E. Cho, J.J. Jo, H.Y. Ha, S. Hong, K. Lee, T. Lim, I. Oh, Characteristics of the PEMFC repetitively brought to temperatures below 0 °C, J. Electrochem. Soc. 150 (2003) A1667-A1670.

[16] S. Ge, C-Y. Wang, In situ imaging of liquid water and ice formation in an operating PEFC during cold start, Electrochem. Sold-State Lett. 9 (2006) A499-A503.

[17] S. Ge, C.Y. Wang, Cyclic voltammetry study of ice formation in the PEFC catalyst layer during cold start, J. Electrochem. Soc. 154 (2007) B1399-B1406.

[18] Y. Hiramitsu, N. Mitsuzawa, K. Okada, M. Hori, Effects of ionomer content and oxygen permation of the catalyst layer on proton exchange membrane fuel cell cold start-up, J. Power Sources 195 (2010) 1038-1045.

[19] Y. Hishinuma, T. Chikahisa, F. Kagami, T. Ogawa, The design and performance of a PEFC at a temperature below freezing, Japan Soc. Mech. Eng. Int. J. 47 (2004) 235-241.

[20] Y. Tabe, M. Saito, K. Fukui, T. Chikahisa, Cold start characteristics and freezing mechanism dependence on start-up temperature in a polymer electrolyte membrane fuel cell, J. Power Sources 208 (2012) 366-373.

[21] P. Oberholzer, P. Boillat, R. Siegrist, R. Perego, A. Kästner, E. Lehmann, G.G. Scherer, A. Wokaun, Cold-start of a PEFC visualized with high resolution dynamic in-plane neutron imaging, J. Electrochem. Soc. 159 (2011) B235-B245.

[22] R. Satija, D.L. Jacobson, M.A. Arif, S. A. Werner, In situ neutron imaging technique for evaluation of water management sytems in operating PEM fuel cells, J. Power Sources 129 (2003) 238-245.

[23] G. Hwang, H. Kim, R. Lujan, R. Mukundan, D. Spernjak, R.L. Borup, M. Kaviany, M.H. Kim, A.Z. Weber, Phase-change-related degradation of catalyst layers in proton-exchange-membrane fuel cells, Electrochim. Acta 95 (2013) 29-37.

[24] Y. Ishikawa, T. Morita, K. Nakata, K. Yoshida, M. Shiozawa, Behavior of water below the freezing point in PEFCs, J. Power Sources 163 (2007) 708-712.

[25] Y. Ishikawa, H. Hamada, M. Uehara, M. Shiozawa, Super-cooled water behavior inside polymer electrolyte fuel cell cross-section below freezing temperature, J. Power Sources 179 (2008) 547-552.

[26] S. Ge, C.Y. Wang, Characteristics of subzero startup and water/ice formation on the catalyst layer in a polymer electrolyte fuel cell, Electrochim. Acta 52 (2007) 4825-4835.

[27] H. Meng, A PEM fuel cell model for cold-start simulations, J. Power Sources 178 (2008) 141-150.

[28] L. Mao, C.Y. Wang, Y. Tabuchi, A multiphase model for cold start of polymer electrolyte fuel cells, J. Electrochem. Soc. 154 (2007) B341-B351.

[29] L. Mao, C.Y. Wang, Analysis of cold start in polymer electrolyte fuel cells, J. Electrochem. Soc. 154 (2007) B139-B146.

[30] M. Khandelwal, S. Lee, M.M. Mench, One-dimensional thermal model of cold-start in a polymer electrolyte fuel cell stack, J. Power Sources 172 (2007) 816-830.

[31] R. Balliet, K.E. Thomas-Alyea, J. Newman, Water movement during freezing in a polymer-electrolyte-membrane fuel cell, ECS Trans. 16 (2008) 285-296.

[32] K. Jiao, X. Li, Three-dimensional multiphase modeling of cold start processes in polymer electrolyte membrane fuel cells, Electrochim. Acta 54 (2009) 6876-6891.

[33] M. Avrami, Kinetics of phase change I general theory, J. Chem. Phys. 7 (1939) 1103-1112.

[34] M. Avrami, Kinetics of phase change II transformation-time relations for random distribution of nuclei, J. Chem. Phys. 8 (1940) 212-224.

[35] W.A. Johnson, R.F. Mehl, Reaction kinetics in processes of nucleation and growth, AIME Trans. 135 (1939) 416.

[36] A.N. Kolmogorov, Selected Works of A.N. Kolmogorov, vol. 1, Kluwer Academic Publishers, Dodrecht, 1985, pp. 530-560.

[37] L.I. Rubinstein, The Stefan Problem, AMS, Providence, Rhode Island, 1971, chapter 1.

Chapter 2

Isothermal Ice-Crystallization Kinetics in the Gas-Diffusion Layer of a Proton-Exchange-Membrane Fuel Cell

T.J. Dursch, M.A. Ciontea, C.J. Radke, A.Z. Weber, Isothermal Ice-Crystallization Kinetics in the Gas-Diffusion Layer of a Proton-Exchange-Membrane Fuel Cell, Langmuir 28 (*2012*) *1222-1234.*

2.1. Abstract

Nucleation and growth of ice in the fibrous gas-diffusion layer (GDL) of a proton-exchange membrane fuel cell (PEMFC) are investigated using isothermal differential scanning calorimetry (DSC). Isothermal crystallization rates and pseudo-steady-state nucleation rates are obtained as a function of subcooling from heat-flow and induction-time measurements. Kinetics of ice nucleation and growth are studied at two polytetrafluoroethylene (PTFE) loadings (0 and 10 wt %) in a commercial GDL for temperatures between 240 and 273 K. A nonlinear ice-crystallization rate expression is developed using Johnson-Mehl-Avrami-Kolmogorov (JMAK) theory, in which the heat-transfer-limited growth rate is determined from the moving-boundary Stefan problem. Induction times follow a Poisson distribution and increase upon addition of PTFE, indicating that nucleation occurs more slowly on a hydrophobic fiber than on a hydrophilic fiber. The determined nucleation rates and induction times follow expected trends from classical nucleation theory. A validated rate expression is now available for predicting ice-crystallization kinetics in GDLs.

2.2. Introduction

Proton-exchange-membrane fuel cells (PEMFCs) show promise in automotive applications because of their high efficiency, high power density, and potentially low emissions. In a PEMFC, reduction of oxygen to water occurs in the cathode. Under subfreezing conditions, water solidifies and hinders access of reactant gases to the catalytic sites in the cathode, thereby severely inhibiting cell performance and possibly causing cell failure [1]. For this reason, understanding the mechanism and kinetics of ice formation is critical to achieving successful cell startup and sustaining high performance at low temperatures.

Because of cell failure under subfreezing conditions, much attention has been given to understanding the fundamentals of cold-start. To date, experimental studies of PEMFC cold-start primarily focus on characterizing overall low-temperature cell performance including: degradation after freeze-thaw cycles [1], effects of cell material properties [2-6], and *in-situ* visualization of ice formation [7,8]. Numerous studies show that the cell electrical potential decays rapidly at low temperatures and/or at high current densities due to ice formation at the reactive area of the cathode [1-6]. Few studies, however, focus on understanding the mechanism of ice crystallization. In two cases, the formation of liquid water and ice within the cathode was visualized using infrared and visible imaging [7,8]. It was shown that water was generated in the subcooled state at −10 °C [8]. Although water did not freeze immediately in the cathode, crystallization kinetics and its dependence on subcooling were not investigated.

Several multiphase, multidimensional cold-start continuum models have been developed [9,10]. These models assume that product water vapor instantaneously solidifies when the vapor partial pressure exceeds the saturation value. As a result, liquid water within the PEMFC is not accounted for. Recently, cold-start models have been extended to include all phases of water, using the equilibrium Gibbs-Thomson equation to predict freezing-point depressions [11,12]. These models estimate the amount of water and ice in a distribution of pores. However, they invoke thermodynamics-based freezing and circumvent ice-crystallization kinetics, since at this time, validated ice-crystallization kinetics do not exist within PEMFC media.

Previous work on ice-crystallization kinetics in porous media is also limited in scope with primary applications to frost heave in soils [13,14]. Bronfenbrener and Korin [13,14] experimentally determined kinetic and thermodynamic parameters for ice formation in fine-grained soil. They assumed that the water-crystallization rate is first-order in water content. Other studies of crystallization kinetics in porous media include solidification of water in gel networks and cement pastes, and characterization of polymer-crystallization kinetics in silica gels [15-18]. Because the properties of fuel-cell materials differ considerably from the aforementioned media in wettability, pore size, and microstructure, the proposed crystallization rates are not necessarily applicable.

The goal of the present work is to provide a rate equation for ice formation as a function of ice amount, temperature, and wettability valid within the gas-diffusion layer (GDL) of a PEMFC. Specifically, ice formation is studied within a GDL because this layer retains a significant amount of product water upon cell shutdown [7,8]. We present a general method for experimentally determining crystallization and nucleation rates using isothermal differential scanning calorimetry (DSC). Furthermore, we develop a nonlinear ice-crystallization rate expression using the Johnson-Mehl-Avrami-Kolmogorov (JMAK) framework that allows extension to the other porous transport layers within the PEMFC.

2.3. Materials and Methods

2.3.1. GDL Characterization:

GDLs containing 0 and 10-wt % polytetrafluoroethylene (PTFE) were obtained from Toray (Toray Corp., Tokyo, Japan) and Fuel Cell Earth (FCE, Stoneham, MA), respectively. The FCE GDL is a Toray GDL that contains 10-wt % (PTFE), and GDLs are referred to as GDL(0) and GDL(10), respectively. Relevant material properties are listed in Table 2.1.

Table 2.1. GDL Properties

GDL	Thickness (μm)	PTFE (wt %)	Porosity, ε	Water Saturation, S
GDL(0)	190	0	[a]80.0 %	[b]84±3 %
GDL(10)	190	10	[a]72.8 %	[b]78±2 %

[a] Mercury-intrusion-porosimetry data provided by Los Alamos National Laboratory
[b] From equation 2.1

Figure 2.1 shows scanning-electron-microscopy (SEM) images of a dry GDL(0) (a) and a dry GDL(10) (b). These commercial GDLs are highly porous carbon-fiber papers with porosities ranging from 70 to 90 % and fiber sizes varying between 5 and 10 μm [19]. GDLs are generally treated with nonwetting PTFE to allow for efficient water removal and to prevent flooding. However, addition of PTFE decreases both the medium electrical conductivity and porosity. As a result, there exists a wettability that optimizes overall cell performance [19].

2.3.2. Sample Preparation:

GDL samples were bored into 3.75-mm diameter circles and saturated with Ultrapure Milli-Q® (Millipore, Billerica, MA) distilled/deionized water in a home-built vacuum chamber for 45 min at 4.7 kPa. Excess surface water was blotted with Fisherbrand® (Fisher Scientific, Pittsburg, PA) weighing paper. Water content was determined gravimetrically and measured values were consistent with integrated peak areas generated from DSC. Water loss by evaporation during DSC experiments was determined to be negligible. Additionally, capillary-pressure-saturation measurements show that water does not drain from the GDL interior under atmospheric pressure [20]. Water content was converted to saturation by the expression

$$S = \frac{V_o}{V_p} = \frac{m_l}{m_{dry}} \frac{\rho_{dry}}{\varepsilon \rho_l} \tag{2.1}$$

where S is liquid-water saturation, V_o is the initial-water volume, V_p is the pore volume, m is mass, ε is porosity, ρ_l is the mass density of water, and ρ_{dry} is the mass density of the dry GDL. Porosities and dry densities were estimated following Lim and Wang [21]. From the material properties in Table 1.1 and equation 2.1, GDL water saturations were calculated between 75 and 85%, consistent with the end points of corresponding capillary-pressure-saturation measurements [20].

2.3.3. Differential Scanning Calorimetry:

A PerkinElmer 6000 DSC (PerkinElmer Inc., Waltham, MA) with a liquid-nitrogen chiller measured the heat-flow rate from the sample over time. The DSC was calibrated from the melting points of 99.999% indium (429.78 K) and zinc (692.68 K) (PerkinElmer Inc., Waltham, MA), as well as from dodecane (263.55 K) (Sigma Chemical Co., St. Louis, MO) at lower temperatures. Heat flow to the calorimeter was calibrated using the heat of fusion of indium (28.47 J/g), following Gmelin and Sarge [22]. Nitrogen served as the purge gas at a flow rate of 20 mL/min. Water-saturated GDL samples, weighing between 3 and 5 mg, were placed into 20-μL PerkinElmer hermetically-sealed aluminum pans.

Isothermal crystallization was carried out in the temperature range of 240 to 273 K. Water-saturated GDL samples were placed into the DSC at 300 K and cooled to the desired temperature at 105 K/min. This rapid cooling rate was chosen such that the lowest temperature was reached well before the onset of crystallization. Samples were then held at the subcooled temperature until crystallization was complete. Experiments were performed at two PTFE loadings (0 and 10 wt %) and at various subcoolings, ΔT, defined as the magnitude of the difference in the temperature of freezing and 273 K.

(a)

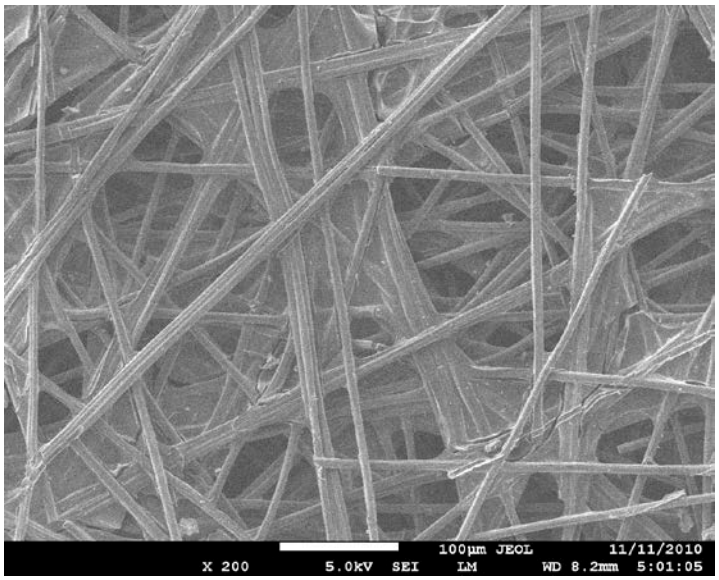

(b)

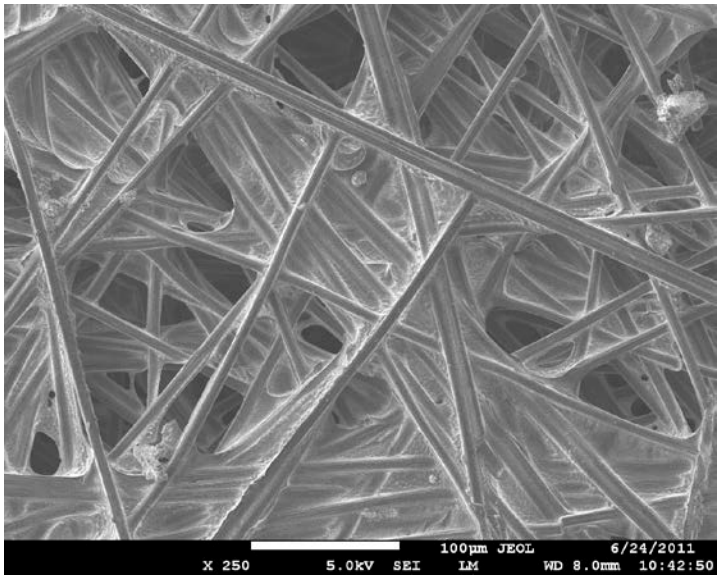

Figure 2.1. SEM images of the GDL(0) (a) and the GDL(10) (b). Both are Toray carbon papers that have either 0 or 10-wt % PTFE, respectively.

2.4. Results

2.4.1. Isothermal Ice-Crystallization Kinetics:

Figure 2.2 shows a typical exotherm of heat flow and sample temperature versus time for the GDL(0). Baseline heat flow was adjusted by subtracting the heat measured for the same cycle in an empty furnace. The sample was cooled at 105 K/min to 247 K, where isothermal crystallization commenced (point A in Figure 2.2). Heat flow due to liberation of the enthalpy of crystallization from point A is evident until a maximum is observed at point B, after which crystallization slows significantly until complete crystallization occurs at point C. To obtain the gas-free volume fraction of ice within the GDL pores, ϕ, as a function of time, crystallization exotherms were integrated from point A to point C according to the expression

$$\phi = \frac{\int_0^t \dot{Q}(t)dt}{\int_0^\infty \dot{Q}(t)dt} \tag{2.2}$$

where $\dot{Q}(t)$ is the heat-flow rate (mW) from the DSC. Agreement is excellent between total-heat flow for complete crystallization divided by the heat of fusion and the gravimetric water content of the sample. From Figure 2.2, it is observed that crystallization is preceded by an induction time, τ_i. We define τ_i as the time elapsed between the sample temperature becoming isothermal and the onset of the crystallization peak (point A), about 8 s in Figure 2.2.

Figures 2.3 and 2.4 show the crystallization kinetics, ϕ versus *t*, calculated from equation 2.2 at three values of ΔT for GDL(0) and GDL(10), respectively. At each subcooling, τ_i was subtracted from the total time so that all curves are compared on a single time scale. Open symbols represent an average of two exotherms measured for two distinct samples. An integrated exotherm for the GDL(0) at a ΔT of 22 K is included in Figure 2.4 for ease of comparison (filled triangles). Solid lines in the figures are best least-squares fits to the data as described below. From Figure 2.4, we observe that at about 20-K subcooling, the time for complete crystallization increases from 9.2 to 14 s for the GDL(0) and GDL(10), respectively. This result suggests that the wettability of the fiber surface plays a role in the crystallization process. More importantly in both figures, the characteristic time for complete crystallization (beyond τ_i) decreases significantly as ΔT increases, indicating that the crystallization rate depends strongly on ΔT.

In many DSC studies, the Avrami relation is adopted to describe crystallization kinetics [23-26]

$$\phi = 1 - \exp\left(-k(T)(t-\tau_i)^n\right) \tag{2.3}$$

where *k* is the overall rate constant and *n* is the Avrami exponent. To obtain *k* as function of *T*, equation 2.3 is fit to the integrated crystallization exotherms in Figures 2.3 and 2.4. Based on heat-transfer-limited volume growth, as justified below, we take *n* = 5/2. Resulting fit values of

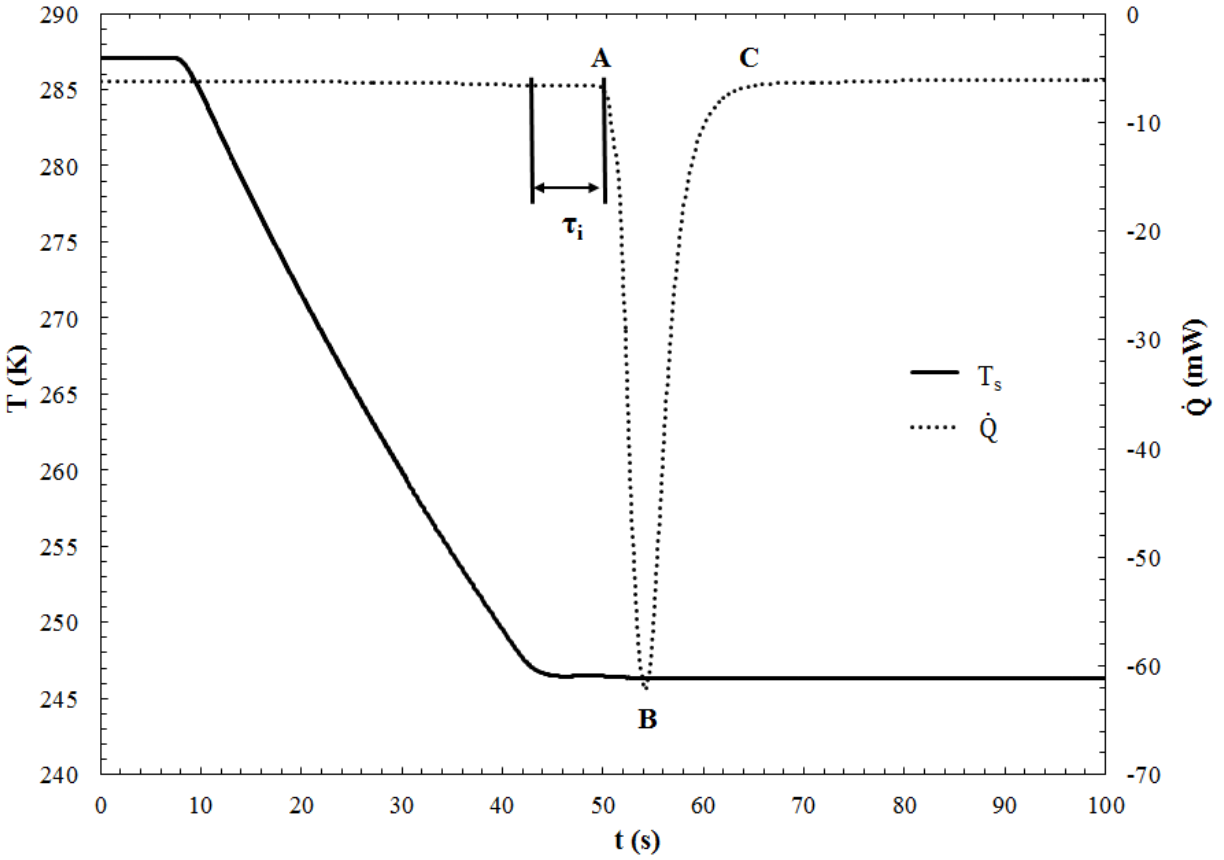

Figure 2.2. Typical isothermal DSC cooling exotherm of GDL(0) at 247 K. The solid line corresponds to the sample temperature, whereas the dotted line represents heat flow. The symbol τ_i labels the induction time. A-C label the onset, extremum, and completion of water freezing, respectively.

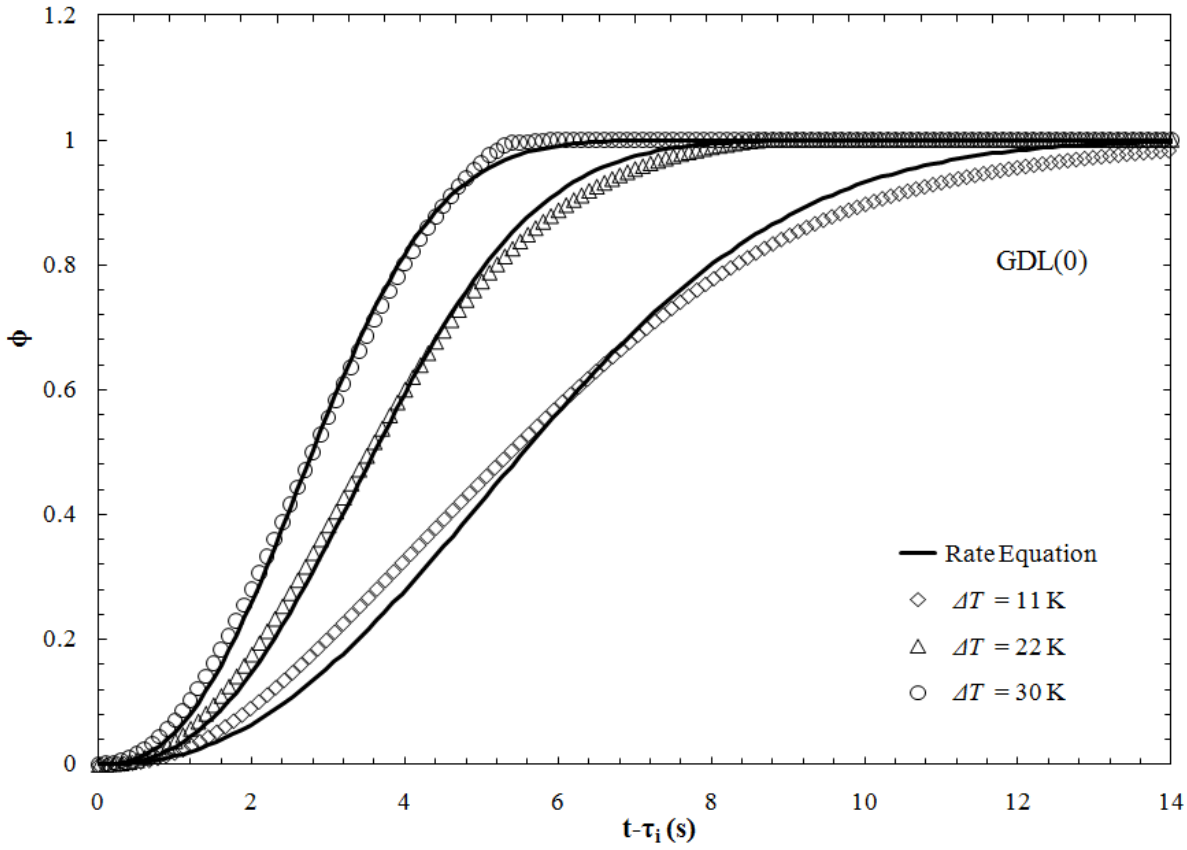

Figure 2.3. Isothermal freezing kinetics for GDL(0), containing 0-wt % PTFE, at three subcoolings. Solid lines represent best least-squares fits of equation 2.3 to the experimental data.

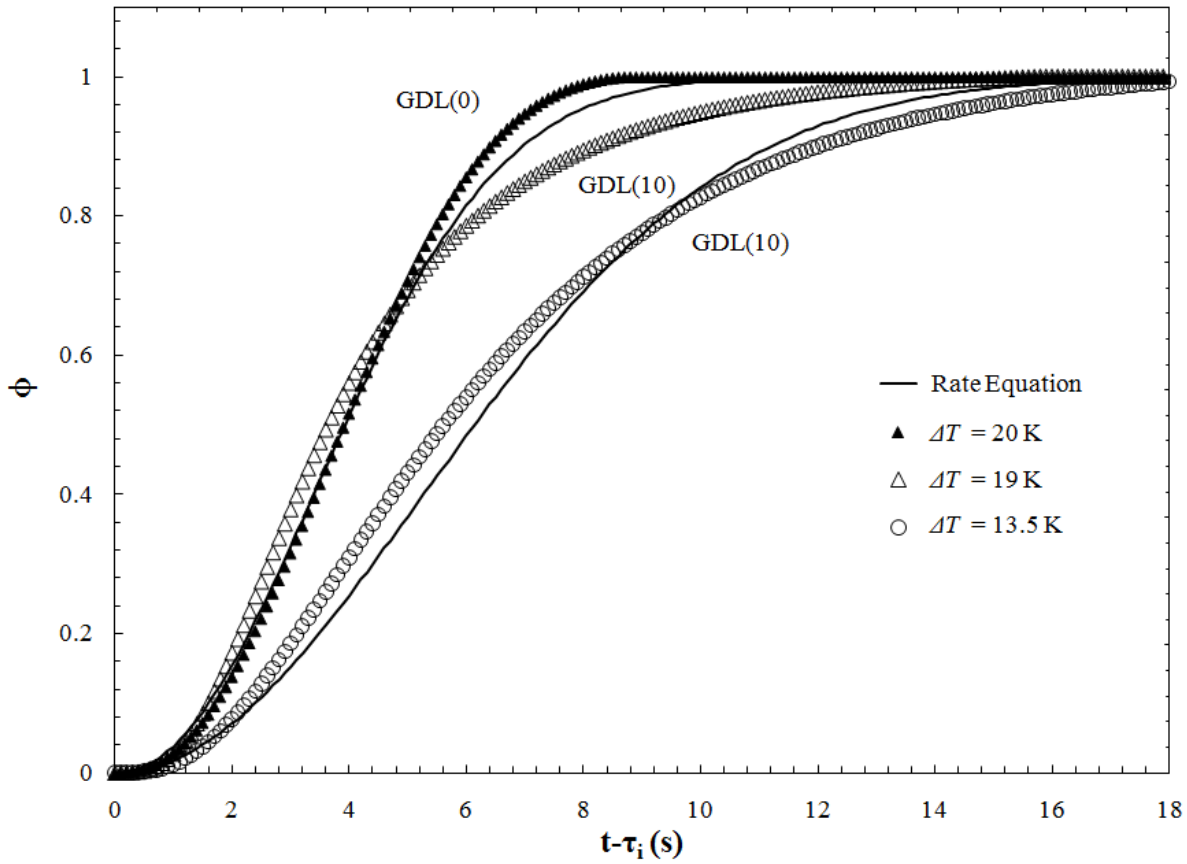

Figure 2.4. Isothermal freezing kinetics for GDL(10) containing 10-wt% PTFE at two subcoolings (open symbols). Closed symbols represent GDL(0), containing 0-wt % PTFE for comparison. Solid lines represent best least-squares fits of equation 2.3 to the experimental data.

$k(T)$ from the solid lines in Figures 2.3 and 2.4 are listed in Table 2.2. In agreement with the trends observed in the figures, k increases as ΔT increases and decreases upon addition of PTFE. With n = 5/2, the Avrami equation is in good agreement with integrated exotherms for both GDL(0) and GDL(10).

Table 2.2. Crystallization Rate Constant, k, for GDL(0) and GDL(10)

GDL(0), k ($s^{-2.5}$)	**GDL(10), k ($s^{-2.5}$)**	**Subcooling, ΔT (K)**
0.009	-	11
-	0.008	13.5
-	0.017	19
0.023		20
0.029	-	22
0.053	-	30

2.4.2. Induction Time:

Repeated crystallization exotherms reveal that τ_i is not constant at a given value of ΔT. To investigate the statistical nature of the crystallization process, τ_i was measured repeatedly (a minimum of 35 measurements) at each of four values of ΔT. Figure 2.5 shows 38 induction times measured at subcoolings of (a) 11 K and (b) 22 K, where the dotted line indicates the number-average induction time, $\bar{\tau}_i$. For both subcoolings, τ_i generally lies below the mean with intermittent excursions to long times. The average induction time decreases significantly from 34.7 s at a subcooling of 11 K to 5.0 s at 22 K. This result suggests that similar to the crystallization rate, the induction process also depends strongly on ΔT.

To investigate further the effect of subcooling on τ_i, single induction-time measurements were performed at a number of intermediate values of ΔT. Figure 2.6 displays τ_i as a function of ΔT for GDL(0). Filled symbols denote a single-τ_i measurement, whereas open symbols represent the number-average induction time, $\bar{\tau}_i$, for at least 35 measurements. Error bars on the open symbols indicate the maximum range of observed τ_i and are included from Figure 2.5 for reference. The solid line is drawn according to classical nucleation theory (CNT) and is discussed later. As with the data in Figure 2.5, as ΔT increases, τ_i decreases substantially. Our measured values are qualitatively similar to induction times reported by Heneghan et al. [27] for bulk water and for AgI-seeded water.

To quantify the effect of PTFE on crystallization, similar τ_i measurements were performed on GDL(10). Figure 2.7 shows a plot of single-τ_i measurements as a function of ΔT

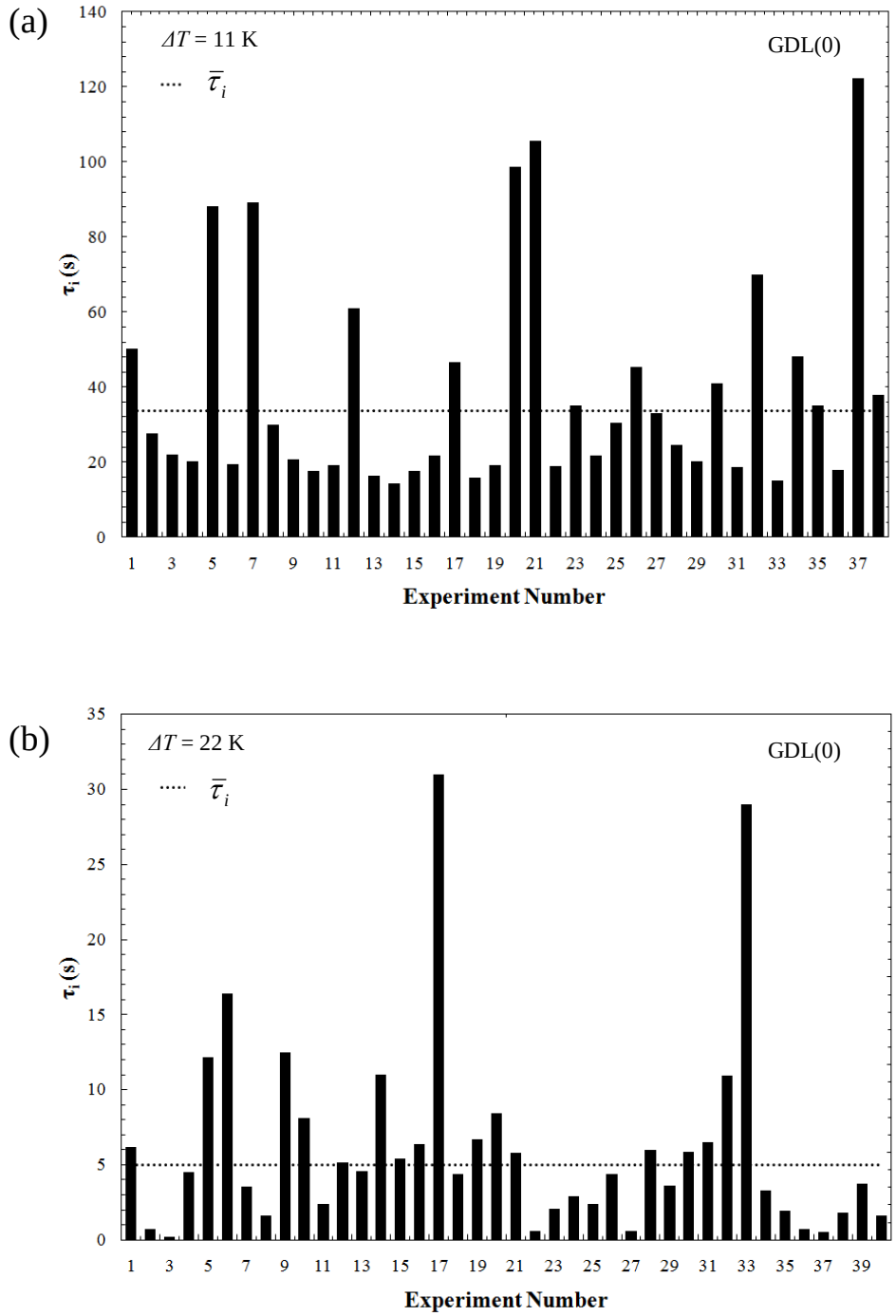

Figure 2.5. 38 induction-time measurements at a subcooling of (a) 11 K and (b) 22 K for GDL(0). A dotted line indicates the number-average induction time.

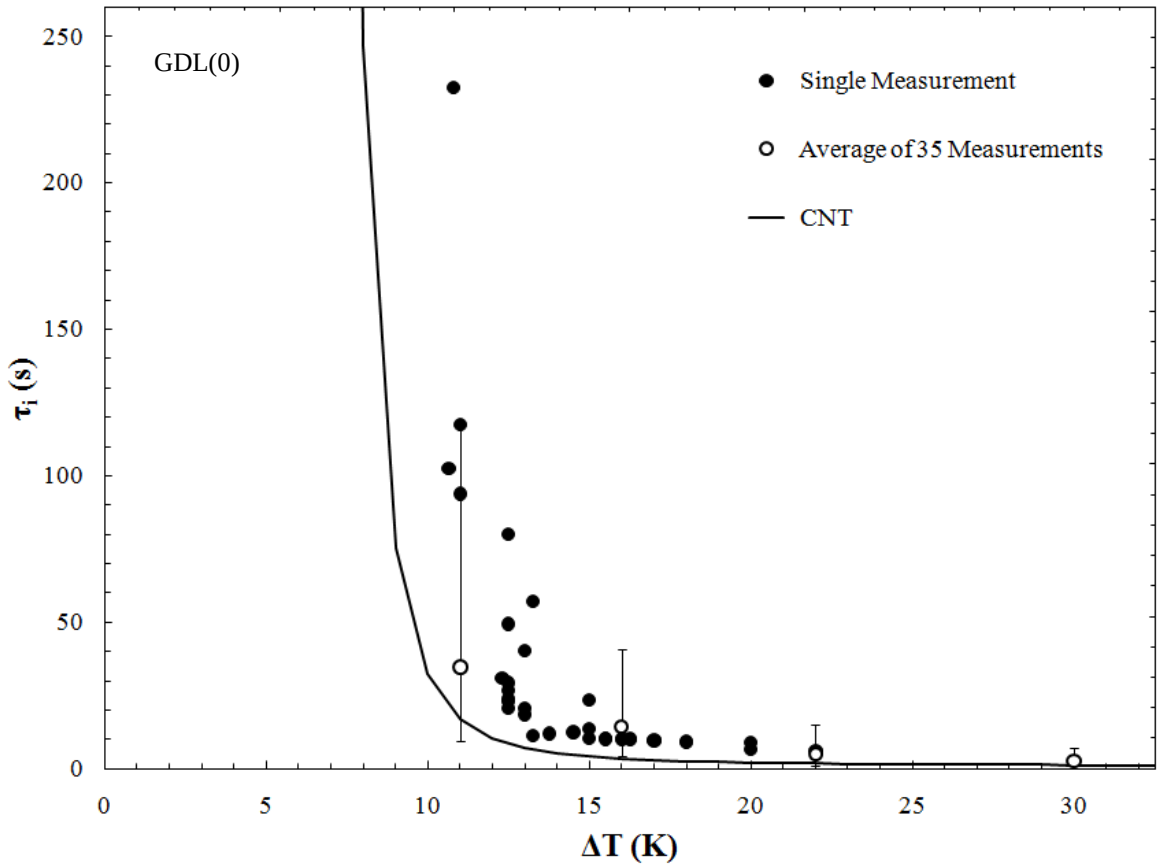

Figure 2.6. Induction times as a function of subcooling for GDL(0). Filled symbols are single induction-time measurements ($\tau_{i,O}$), whereas open symbols represent the number-average induction times over a minimum of 35 measurements ($\bar{\tau}_{i,O}$). Error bars indicate the maximum range of observed induction times. The solid line is a prediction for $\bar{\tau}_{i,O}$ from classical nucleation theory (CNT).

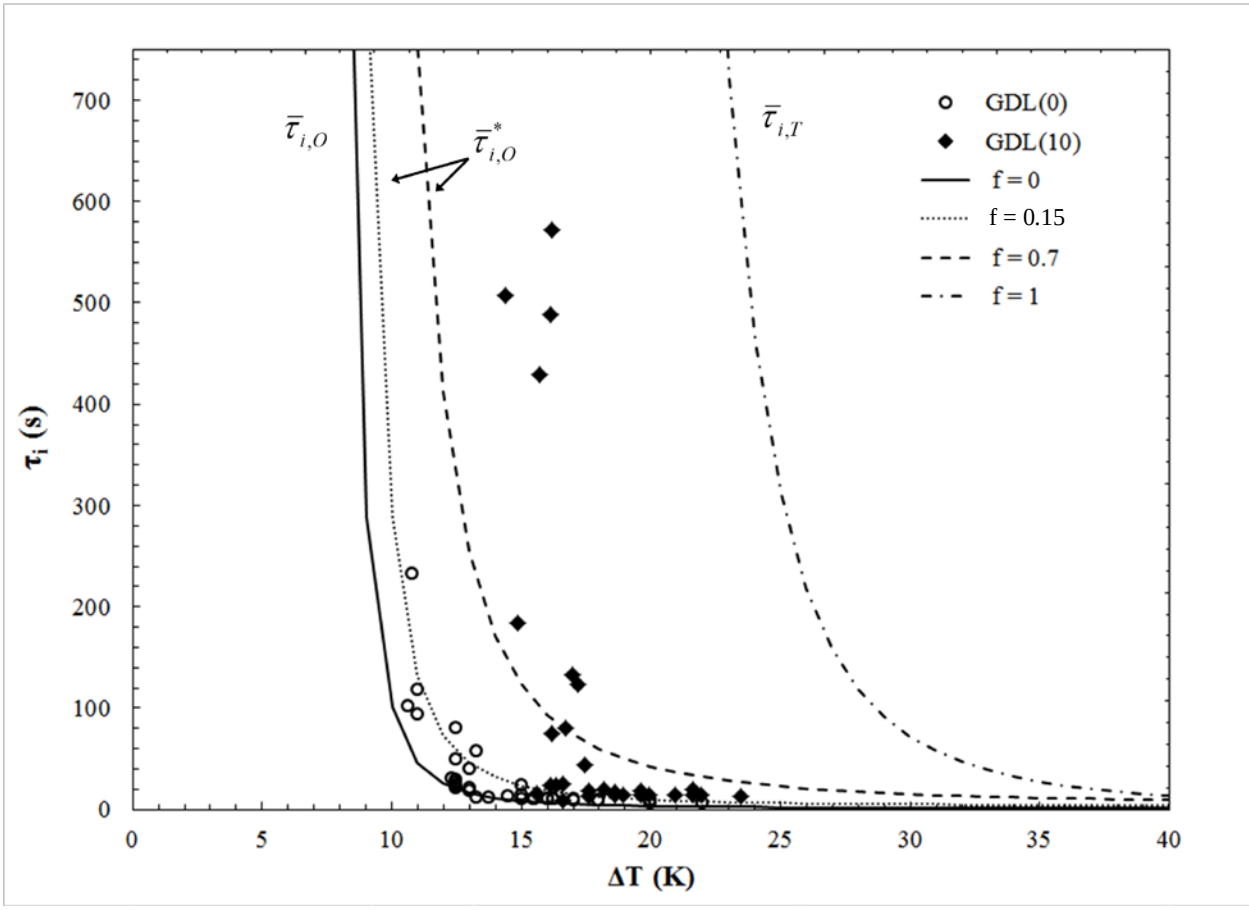

Figure 2.7. Induction times as a function of subcooling for GDL(0) (open symbols) and GDL(10) (closed symbols). Solid, dotted, and dashed lines are predictions for $\bar{\tau}_i^*$ from CNT (equation 2.20) for nucleation on oxidized carbon fibers at varying f, where f is the surface-area fraction of PTFE in the GDL. The dash-dotted line is a prediction for $\bar{\tau}_i^*$ from CNT (equation 2.19) for nucleation on completely PTFE-coated fibers.

for GDL(10) with the results included from Figure 2.6 for reference. Open symbols reflect GDL(0), whereas closed symbols correspond to GDL(10). The solid, dashed, and dotted lines are from classical nucleation theory (CNT) as discussed below. Addition of PTFE to the carbon-fiber network increases τ_i at nearly all values of ΔT. The GDL(0) curve is identical to the GDL(10) curve, but is shifted to longer ΔT by about 4.5 K. Thus, the formation of ice on hydrophobic fibers commences at a longer induction time for a given subcooling. Similar results have been reported elsewhere [28,29] showing that the time for complete ice crystallization is longer on a hydrophobic surface than on a hydrophilic surface.

2.5. Theory

Parameters *k* and τ_i in equation 2.3 are obtained empirically. As shown in Table 2.2 and in Figures 2.3 through 2.7, these parameters are strong functions of both subcooling and wettability. To obtain a predictive rate equation, however, *k* and τ_i must be specified *a priori*. For this task, we adopt Johnson-Mehl-Avrami-Kolmogorov (JMAK) theory.

2.5.1. Ice-Crystallization Kinetics:

Within the JMAK framework, crystallization occurs via a continuing two-step process [23-26], shown schematically in Figure 2.8. Crystallization begins in Figure 2.8a with nucleation (as outlined in Appendix 2A) during which time a critical nucleus forms at the critical radius, r^*, corresponding to an average nucleation rate, *J* (nuclei/volume-time), and to a contact angle, θ (measured through the solid phase). Following nucleation, the critical nucleus grows in Figure 2.8b to a macroscopic size, *r*(*t*), during the growth step. This two-step process repeats stochastically until the liquid completely solidifies. At long times, impingement (i.e., size exclusion) of growing nuclei becomes increasingly important. To account for impingement, the so-called Avrami extended or overlapping volume is used, where theoretically overlapping volumes are allowed to grow into remaining free volume. Using this reasoning, JMAK show that in a time, *t*, the volume fraction of solid transformed, ϕ, is well-described by a convolution integral over nucleation and growth rates [23-26]

$$\phi = 1 - \exp\left(-\frac{4\pi}{3} g(\theta) \int_{\bar{\tau}_i}^{t} J(T(t'))\, r^3(t-t')\, dt' \right) \tag{2.4}$$

where [30]

$$g(\theta) = \frac{1}{4}(2+\cos\theta)(1-\cos\theta)^2, \tag{2.5}$$

and $J(T)$ is the overall pseudo-steady-state nucleation rate, θ is the contact angle, and $r(t) > r^*$ is the radius of a growing nucleus as a function of time. The explicit time dependence of the nucleation rate is ignored because the time to establish pseudo-steady state nucleation is extremely fast [31]. Equation 2.5 corresponds to a solid spherical segment growing on a flat surface. A flat surface is a good approximation since the radius of a critical nucleus (nm) is orders of magnitude smaller than the radius of a GDL fiber (μm).

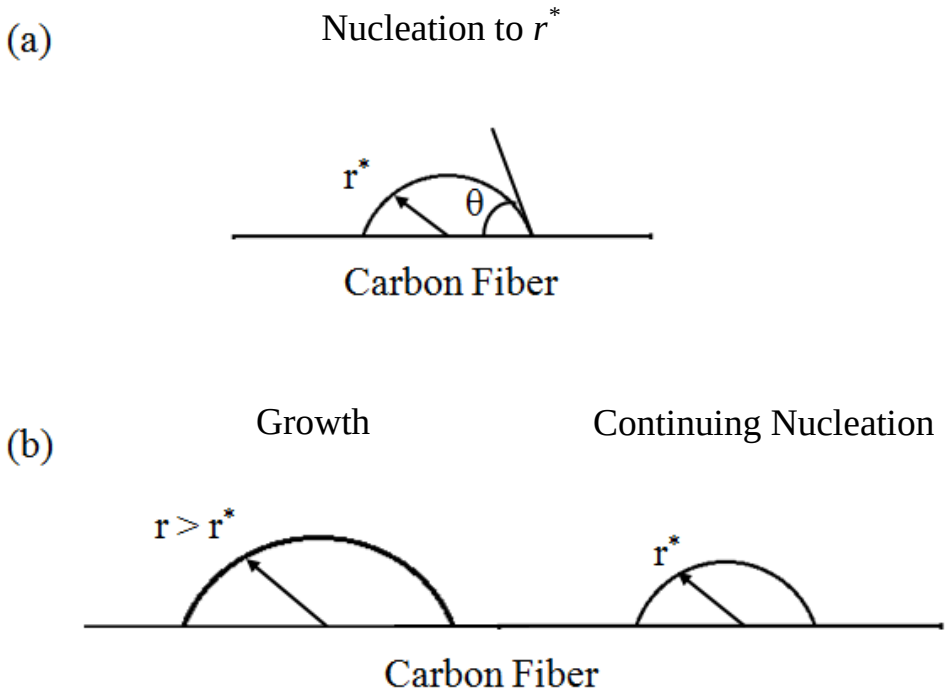

Figure 2.8. Schematic of the continuous two-step crystallization process occurring within a subcooled liquid: (a) nucleation and (b) growth with continuing nucleation. r^* is the critical nucleation radius, and θ is the contact angle of the ice/water/substrate triple line measured through solid ice.

Nuclei described by equation 2.4 form heterogeneously on GDL fibers at time, *t'*, and grow isotropically in three-dimensions from *t'* to *t*. GDLs impregnated with PTFE exhibit hydrophobic patches of coated fibers and hydrophilic regions of uncoated fibers at a geometric scale (μm) much larger than that of the nucleating ice crystals (nm). Therefore, we do not estimate an average contact angle, but rather consider two distinct wetting domains for nucleation. To a first approximation, the overall nucleation rate is a sum of individual nucleation rates on oxidized carbon, J_O, and on PTFE-coated carbon, J_T, weighted by their respective surface-area fractions

$$J = f\ J_T + (1-f)\ J_O \tag{2.6}$$

where *J* is the overall nucleation rate and f is the surface-area fraction of the PTFE coating. Due to the non-uniformity of the PTFE-impregnation process, the surface-area fraction of PTFE is difficult to assess. Consequently, we examine the sensitivity of equation 2.6 to the choice of f.

Once nuclei form, growth is limited by heat transfer for small Stefan numbers, defined as the ratio of sensible to latent heat [32]

$$Ste = \frac{\hat{C}_{p,l}\Delta T}{\Delta \hat{H}_f} \tag{2.7}$$

where $\hat{C}_{p,l}$ is the liquid specific heat capacity and $\Delta\hat{H}_f$ is the magnitude of the heat of fusion per mass of solid. For a single heat-transfer-limited growing hemisphere within a subcooled liquid, the so-called Stefan problem [33], the growing solid radius is given by [32]

$$r(t) = 2\eta_o\sqrt{\alpha_l t} \tag{2.8}$$

where α_l is the liquid thermal diffusivity and η_o is a temperature-dependent growth parameter defined by

$$\eta_o^2 \exp\left(\eta_o^2\right)\left[\exp\left(-\eta_o^2\right) - \sqrt{\pi}\eta_o \operatorname{erf}\left(\eta_o\right)\right] = \frac{1}{2}Ste\,. \tag{2.9}$$

Equations 2.8 and 2.9 apply strictly at early growth times before single ice crystals impinge and meld with those growing nearby. At later times, precise prediction of the crystal growth rate is not necessary as liquid exhaustion demands a net zero freezing rate.

Substitution of equations 2.6 and 2.8 into equation 2.4 gives

$$\phi = 1 - \exp\left[-\ f\ k_T (t-\bar{\tau}_{i,T}^*)^{5/2} - (1-f)k_O (t-\bar{\tau}_{i,O}^*)^{5/2}\right] \tag{2.10}$$

with

$$k_T(T) = \frac{64\pi}{15} g(\theta_T) J_T \eta_o^3 \alpha_l^{3/2}, \tag{2.11}$$

and

$$k_O(T) = \frac{64\pi}{15} g(\theta_O) J_O \eta_o^3 \alpha_l^{3/2}, \tag{2.12}$$

where $\bar{\tau}_i^*$ is a number-average induction time (defined in the subsequent section), with the superscript * representing an induction time in a GDL containing mixed-wetting domains. Subscripts *T* and *O* denote PTFE and oxidized carbon, respectively. To enable a deterministic prediction in equation 2.10, we replace the single-event induction time appearing in equation 2.3 by the number-average of the distribution.

Equation 2.10 does not correspond directly to the Avrami relation in equation 2.3 used to fit the crystallization kinetics in Figures 2.3 and 2.4. However, for GDL(10) and the range of ΔT used in this study, equation 2.10 simplifies considerably. As shown in detail below, $J_T f << J_O(1-f)$. Hence, the first term in equation 2.6 and in the exponential argument of equation 2.10 is negligible. Application of this approximation in equation 2.10 leads to the Avrami expression in equation 2.3 with n = 5/2, $k = (1-f)k_O$, and $\tau_i = \bar{\tau}_{i,O}^*$. Therefore, equations 2.10 (or 2.3) and 2.12 provide the tools to predict the overall crystallization rate once the unknown parameters J_O, θ_O, and $\bar{\tau}_{i,O}^*$ are specified.

2.5.2. Parameter Determination:

Equation 2.12 contains the pseudo-steady-state nucleation rate, J_O. We evaluate J_O from experimental data independent of the measured freezing kinetics in Figures 2.3 and 2.4. Jiang and Horst [34] show that the cumulative probability, $P(\tau_{i,O})$, that crystals are detected between time zero and the induction time, $\tau_{i,O}$, is

$$P(\tau_{i,O}) = \frac{M^+(\tau_{i,O})}{M} \tag{2.13}$$

where M is the total number of experiments and $M^+(\tau_{i,O})$ is the number of experiments in which a crystallization peak is detected at an induction time less than or equal to $\tau_{i,O}$. From equation 2.13, $P(\tau_{i,O})$ is thus available from repeated induction-time measurements. Figure 2.9 shows the calculated cumulative probability distributions for GDL(0) as open symbols using the data in Figure 2.5, as well as distributions for two additional values of $\Delta T = 16$ and 30 K.

Jiang and Horst also demonstrate that the cumulative distribution function is well-described by a Poisson distribution [34]

$$P(\tau_{i,O}) = 1 - \exp\left(-J_O V_o (\tau_{i,O} - \tau_g)\right) \tag{2.14}$$

where V_o is the initial volume of liquid and τ_g is the time for a critical nucleus to grow to a size detectable by the DSC instrument. Therefore, J_O and τ_g are available by fitting equation 2.14 to the measured cumulative-probability distributions in Figure 2.9. Solid lines in this figure correspond to the best least-squares fit of equation 2.14 and provide values of J_O and τ_g (i.e., the value of *P* at $\tau_{i,O} = 0$) as functions of ΔT. Obtained values are listed in Table 2.3, along with the number-average induction time, $\bar{\tau}_{i,O}$. Figure 2.9 confirms that that the nucleation process in a GDL is well-described by a Poisson distribution.

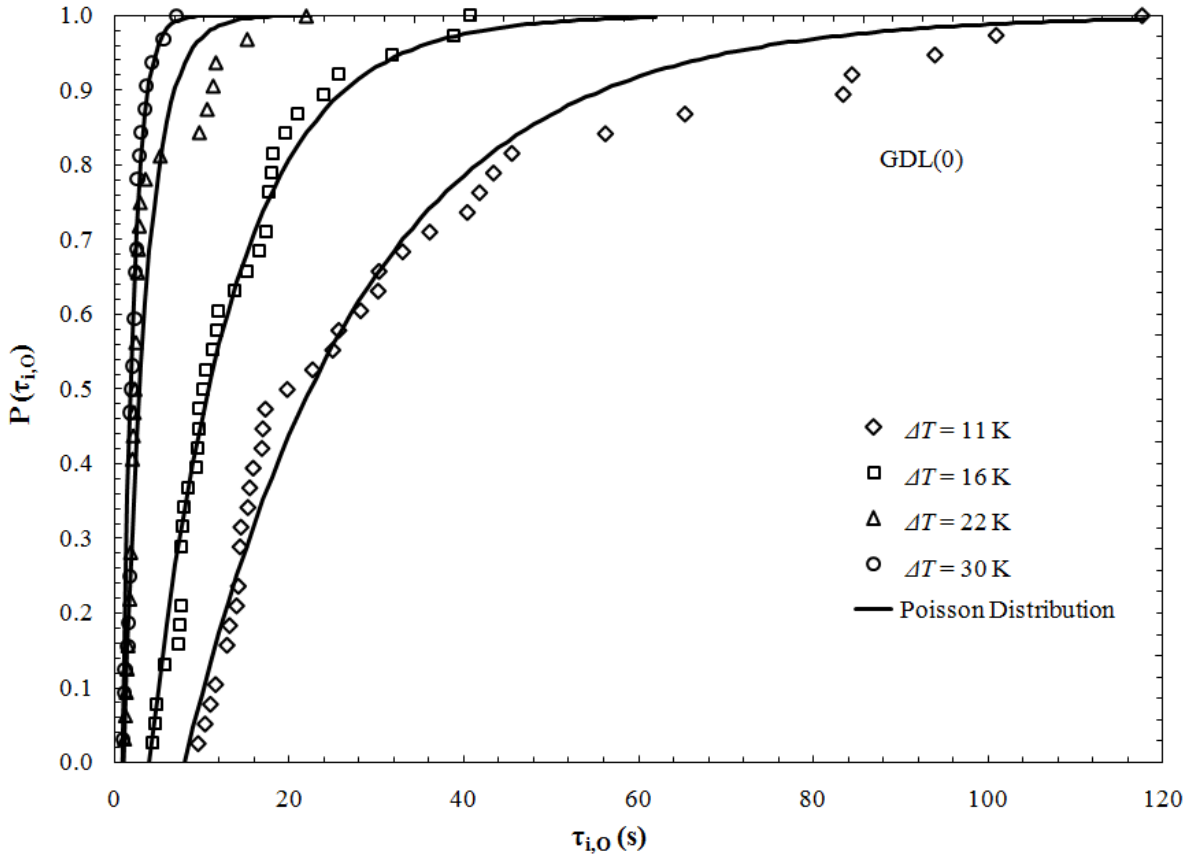

Figure 2.9. Cumulative probability distributions for the induction times shown in Figure 2.5 for GDL(0) along with two additional subcoolings at $\Delta T = 16$ and 30 K. Solid lines are a fit to the probability distribution in equation 2.14.

Table 2.3. Nucleation Rates, Average Induction Times, and Growth Times for GDL(0)

Subcooling, ΔT **(K)**	**Nucleation Rate,** J_O **(×10^{-7} nuclei m^{-3}s^{-1})**	**Induction Time,** $\bar{\tau}_{i,O}$ **(s)**	**Growth Time,** τ_g **(s)**
11	3.3	34.7	7.5
16	12.0	14.3	4.2
22	40.0	5.0	0.7
30	63.0	2.7	0.6

The dependence of J on ΔT is most often described by classical nucleation theory (CNT) [30,35]

$$J = A\exp\left[-\frac{B}{T(\Delta T)^2}\right] \tag{2.15}$$

where

$$B = \frac{4\pi\gamma_{sl}^3 T_o^2 \hat{v}_s^2}{3\Delta\hat{H}_f^2 k_b} g(\theta), \tag{2.16}$$

k_B is the Boltzmann constant, γ_{sl} is the solid/liquid interfacial energy, $\hat{v}_s$ is the specific volume of the solid, T_o is the equilibrium freezing temperature, and $g(\theta)$ is given by equation 2.5. The pre-exponential factor, A, is assumed to be constant, since its temperature dependence is weak compared to the exponential term [30,35]. The functional dependence of J on ΔT described by equations 2.15 and 2.16 indicates that a plot of $\ln J$ versus $T^{-1}\Delta T^{-2}$ produces a straight line with an intercept $\ln A$ and slope $-B$. The resulting plot is shown in Figure 2.10 for the J_O values listed in Table 2.3. The constants, estimated from linear regression, are $A = 7.9\times10^8$ nuclei m^{-3}s^{-1} and $B_O = 9.4\times10^4$ K^3, which yield an average nucleation rate for GDL(0) of

$$J_O = 7.9\times10^8 \exp\left(\frac{-9.4\times10^4}{T(\Delta T)^2}\right) \text{ nuclei m}^{-3}s^{-1}. \tag{2.17}$$

Thus, given an estimate of θ_O, $k_O(T)$ is known from equations 2.9, 2.12, and 2.17. Values for θ are not independently known. We take $\theta_O = 60°$ and $\theta_T = 140°$, as justified below. These contact angles were chosen such that ice preferentially wets oxidized carbon over PTFE; this preference assumes that ice maintains the same relative surface wetting as water against air, i.e., the average ice contact angle increases with the addition of PTFE to the GDL [28,29].

With J_O for GDL(0) now known and the contact angles set, we estimate J_T using equations 2.5 and 2.15-2.17. From the known value of B_O (equation 2.17) for GDL(0) with $\theta_O = 60°$, J_T is determined for all ΔT, since A is independent of θ. We find that

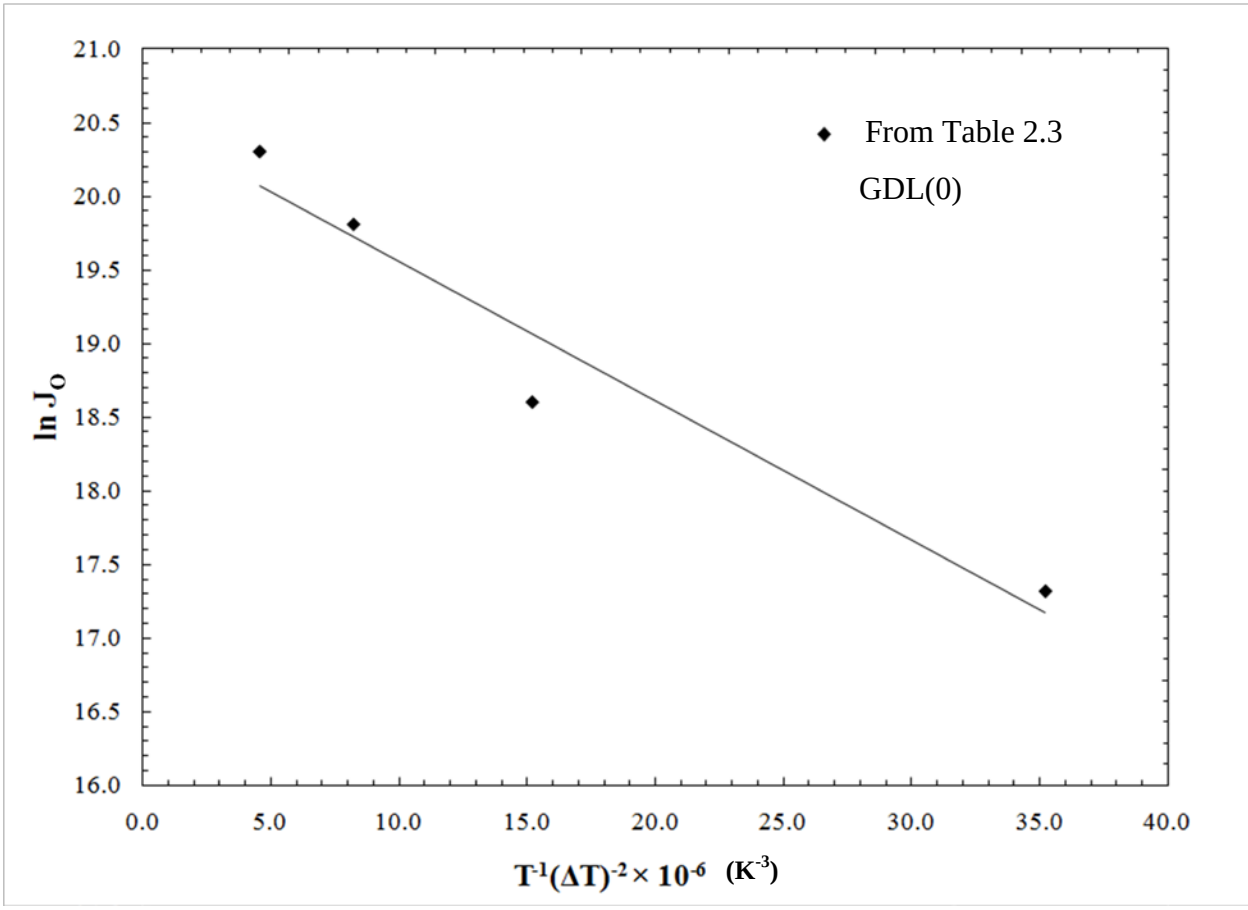

Figure 2.10. Logarithm of the nucleation rate in GDL(0) as a function of $T^{-1}\Delta T^{-2}$ for the values given in Table 2.3. The intercept of the straight line gives ln$A$ and the slope gives $-B_O$, following equation 2.15 and 2.16.

$B_T = 7.3\times10^5$ K^3 for PTFE compared to $B_O = 9.4\times10^4$ K^3 for oxidized carbon. Accordingly, $J_T / J_O << 1$ and nucleation occurs much more slowly on a hydrophobic surface.

The oxidized-carbon number-average induction time, $\bar{\tau}^*_{i,O}$, appearing in equation 2.10 remains to be determined. To obtain $\bar{\tau}_i$, the definition suggested by Kaschiev [36] is adopted with slight modification

$$\bar{\tau}_i = \frac{1}{JV_o} + \tau_g . \tag{2.18}$$

The first term in equation 2.18 represents the mean time for the formation of a critical nucleus, and the second term is included to account for the time elapsed between the formation of a critical nucleus and its growth to a size detectable by the DSC. Values of τ_g lying between those at measured temperatures in Table 2.3 were obtained by linear interpolation. Let $\bar{\tau}^*_i$ represent the number-average induction time in a GDL containing mixed-wetting regions. Substitution of equation 2.6 into equation 2.18 provides the desired expression

$$\bar{\tau}^*_i = \frac{1}{\left(f\ J_T + (1-f)\ J_O\right)V_o} + \tau_g\ . \tag{2.19}$$

Equation 2.19 reduces to induction times for nucleation on surfaces of exclusively oxidized carbon, $\bar{\tau}_{i,O}$, and PTFE, $\bar{\tau}_{i,T}$, when $f = 0$ and $f = 1$, respectively. For these cases, the superscript * is omitted because the GDLs each contain a single-wetting domain.

Since $J_T / J_O << 1$, the first bracketed factor in the denominator of equation 2.19 is negligible provided that $f < 1 - J_T / J_O$. Application of this simplification yields

$$\bar{\tau}^*_i = \bar{\tau}^*_{i,O} \equiv \frac{1}{(1-f)J_O V_o} + \tau_g \qquad \text{for} \quad J_T / J_O << 1 \tag{2.20}$$

where $\bar{\tau}^*_{i,O}$ denotes the number-average induction time only for nucleation on oxidized carbon in a mixed-wetting GDL. Equation 2.20 determines $\bar{\tau}^*_{i,O}$ in equation 2.10. Because nucleation occurs more quickly on oxidized carbon than on PTFE, only $\bar{\tau}^*_{i,O}$ is measured in our work. The solid line in Figure 2.6 compares $\bar{\tau}^*_{i,O} = \bar{\tau}_{i,O}$ for GDL(0) with theory using equation 2.20 with $f = 0$. Good agreement is achieved between theory and experiment: the entire temperature dependence is correctly captured through independent assessment of J_O.

Figure 2.7 shows measured single-induction times for both GDL(0) (open symbols) and GDL (10) (closed symbols). Solid and dash-dotted lines correspond to $\bar{\tau}_{i,O}$ ($f = 0$) and $\bar{\tau}_{i,T}$ ($f = 1$) calculated from equation 2.19, given the measured value of J_O and the estimated value of J_T. Likewise, dotted and dashed lines are calculations of $\bar{\tau}^*_{i,O}$ from equation 2.20 with $f = 0.15$ and $f = 0.7$, respectively. Exact positions of the theoretical predictions depend strongly on the choice of J_O for GDL(0). In Figure 2.7, the average value of J_O is used from

Table 2.3. Since nucleation on the PTFE-coated regions of GDL(10) is negligible in equation 2.19, the increase in $\bar{\tau}_{i,O}^{*}$ with f is attributed to the decrease in the available surface-area fraction of oxidized carbon. Dotted $(f = 0.15)$ and dashed lines $(f = 0.7)$ illustrate the sensitivity of $\bar{\tau}_{i}^{*}$ to the choice of the surface-area parameter f. Again, the experimental data in Figure 2.7 are single-τ_i measurements that lie within the Poisson distribution of τ_i. Due to GDL non-uniformity, it is not possible to determine f independently. As a result, it is difficult to assess quantitative agreement between theory and experiment. Thus in Figure 2.7, comparison between predicted and measured $\bar{\tau}_{i,O}^{*}$-values is qualitative. Nevertheless, as f increases, $\bar{\tau}_{i,O}^{*}$ shifts to longer ΔT, in agreement with measured trends.

2.6. Discussion

2.6.1. Comparison to Experiment:

With the values of J_O, θ_O, and $\bar{\tau}_{i,O}^{*}$ now specified, crystallization kinetics, $\phi(t)$, follow from equation 2.10 for both GDL(0) and GDL(10). In the calculations $k_T = 0$, and k_O obeys equation 2.12, since $k_O(T) >> k_T(T)$. Additionally, $\bar{\tau}_{i,O}^{*}$ is given by equation 2.20, and k_O is calculated using J_O from equation 2.17 and with $\theta_O = 60°$. Accordingly, equation 2.10 reduces to the Avrami expression in equation 2.3.

Figure 2.11 plots k for GDL(0) (filled circles) and GDL(10) (filled triangles) as a function of ΔT from Table 2.2. Solid and dashed lines are theoretical predictions of $k = (1 - f)k_O$ using equation 2.12 with $\alpha_l = 1.4 \times 10^{-7}$ m^2/s, equation 2.9 for η_o, $f = 0$ for GDL(0), and $f = 0.5$ for GDL(10). Error bars on the theoretical lines represent the range of k values calculated using the minimum and maximum nucleation rates as upper and lower bounds. Error increases as ΔT increases because the nucleation rate increases rapidly as ΔT increases. From Figure 2.11, good agreement is observed between fitted and predicted rate constants, particularly at high values of ΔT (22 and 30 K). Similar to the empirical rate constants in Table 2.2, k increases as ΔT increases. This result is primarily due to the temperature dependence of the nucleation rate. As PTFE is added to the GDL, the decrease in k is quantitatively consistent with experimentally measured values.

Figures 2.12 and 2.13 show predicted crystallization kinetics, ϕ versus t, for GDL(0) and GDL(10), respectively. At each subcooling, the single-event induction time was subtracted from the total time so that curves are compared on a similar time scale. Open symbols represent an average of two exotherms measured for two distinct samples. Solid lines represent model predictions using calculated k values from Figure 2.11 in equation 2.10, with $f = 0$ and $f = 0.5$ for GDL(0) and GDL(10), respectively. Good agreement is seen between theoretical and measured crystallization rates in both Figures 2.12 and 2.13. In all cases, the time for complete crystallization is accurately predicted. Crystallization times in Figure 2.12 range from 5 to 12 s, increasing as subcooling decreases from 30 to 11 K. The dependence of the crystallization time (above induction time) on the amount of subcooling suggests that the controlling resistance for removing heat is at the interface of the growing crystal. Similar to the findings of Feuillebois et al. [37], nondimensionalizing the ice-crystal/water interface energy balance gives

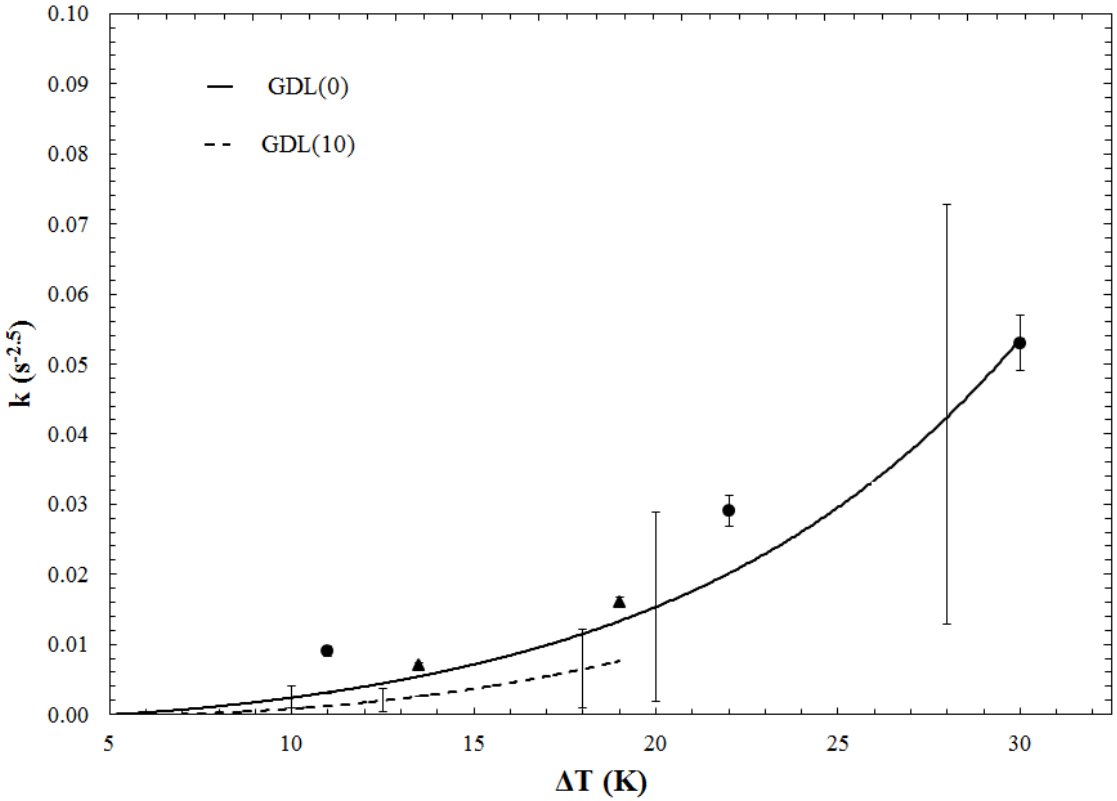

Figure 2.11. Overall rate constant, *k*, for GDL (0) (filled circles) and GDL(10) (filled triangles) as a function of subcooling. Filled symbols correspond to fitted values from equation 2.3. Solid and dashed lines are theoretical predictions of $k = (1 - f)k_O$ with $\alpha_l = 1.4 \times 10^{-7}\,\mathrm{m^2/s}$, $\theta_O = 60°$, an average value for J_O, and $f = 0$ and $f = 0.5$ for GDL(0) and GDL(10), respectively. Error bars on lines indicate the range of calculated *k* using the minimum and maximum J_O obtained from Figure 2.6.

crystallization times in agreement with those found in Figure 2.12. Thus, the characteristic time for ice crystallization is limited by heat conduction away from the growing ice-crystal front, not by heat conduction out of the sample.

For GDLs of differing water wettability, the time for complete crystallization in Figure 2.13 increases from 9.2 to 14 s at a ΔT of 20 K for GDL(0) (no PTFE) and GDL(10) (10 wt% PTFE), respectively. Similarly, the predicted time for complete crystallization increases from 9.8 to 14.3 s. Agreement with theory for GDL(10) indicates that, similar to the induction time, the decrease in crystallization rate is a result of the decrease in the available surface-area fraction of oxidized carbon.

2.6.2. Physical Signifance:

To validate the parameter *B*, equation 2.16 was used to estimate the value of the interfacial free energy, γ_{sl}. For $\Delta\hat{H}_f = 335.6\,\text{J/g}$, $\hat{v}_s = 0.916\,\text{g/cm}^3$, $T_o = 273\,\text{K}$, and $\theta_o = 60°$, γ_{sl} was calculated to be 20 mN/m. Although the value for the ice/water interfacial free energy is not directly measureable, commonly cited values [17,27,38] lie between 20 and 45 mN/m, indicating reasonable agreement. The determined pre-exponential factor is on the same order of measured nucleation prefactors [27,34,39,40], although it is orders of magnitude smaller than values predicted by CNT (typical CNT prefactors are on the order of 10^{30} nuclei $\text{m}^{-3}\text{s}^{-1}$) [29]. Experimentally determined values for *A* are commonly lower than values predicted by CNT [27,34,39,40].

To assess the confidence of the reported nucleation rates, a statistical evaluation of the sample size was performed using a power analysis [41]. We estimate that with 90 % confidence and for a sample size of 35, the reported nucleation rate is within 10 % of the actual rate. Because the nucleation rate depends strongly on temperature, temperature fluctuations are expected to be the most prominent source of error. Our DSC provides measurements with a temperature accuracy of ± 0.1 K, which leads to a maximum uncertainty of, for example, $2.2\times10^{7} \pm 1.7\times10^{6}$ nuclei $\text{m}^{-3}\text{s}^{-1}$ at a ΔT of 10 K.

2.6.3. Relevance to Cold-Start:

To illustrate the importance of ice-formation kinetics in automotive cold-start modeling, equations 2.10 and 2.20 were used to estimate the time required for 99% crystallization in GDL(0), $t_{99\%}$, for varying ΔT. A plot of $t_{99\%}$ as a function of ΔT for the GDL(0) is shown in Figure 2.14. The dotted line estimates the time required for the onset of crystallization (equation 2.20 with $f = 0$) and the dashed line denotes the time required (from the onset of crystallization) to form 99% of ice (equation 2.10 with $k_T(T) = 0$ and $k_O(T)$ given by equation 2.12). The solid line, $t_{99\%}$, is the sum of the dashed and dotted lines. This estimate is drawn using the average value for J_O, neglecting the Poisson distribution of τ_i. $t_{99\%}$ values in Figure 2.14 are conservative due to neglect of the thermal mass of the PEMFC, water transport, and the assumption that the temperature instantaneously lowers to the subcooled temperature.

Two limiting regimes for $t_{99\%}$ are shown in Figure 2.14. At temperatures above 263 K, $t_{99\%}$ is nucleation-rate limited, whereas for temperatures below 263 K $t_{99\%}$ is growth-rate limited. To determine accurately the temperature of transition between the two regimes,

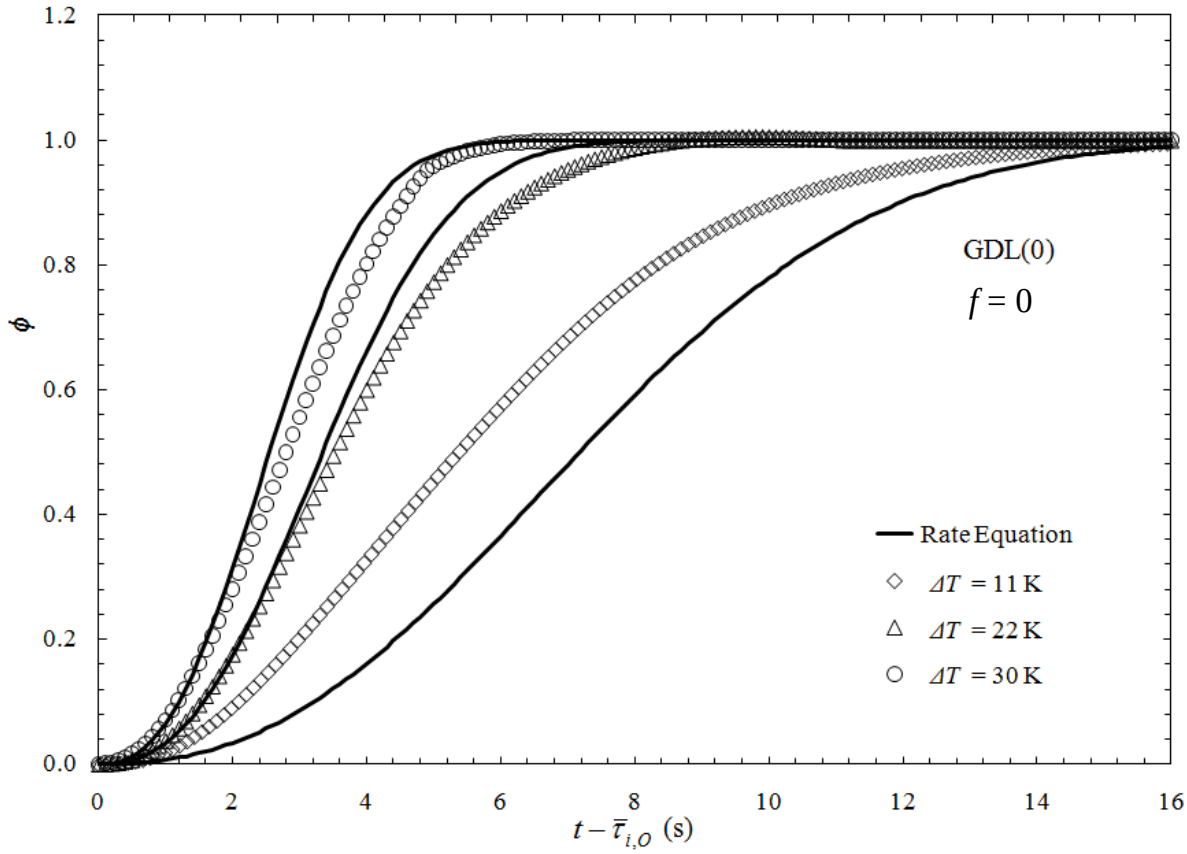

Figure 2.12. Isothermal freezing kinetics for the GDL(0) at three subcoolings. Solid lines represent theoretical predictions of ϕ using equation 2.10 and equation 2.12 for $k_O(T)$ with $\alpha_l = 1.4 \times 10^{-7}\,\mathrm{m^2/s}$, $\theta_o = 60°$, J_O from equation 2.17, η_o from equation 2.9, and $f = 0$.

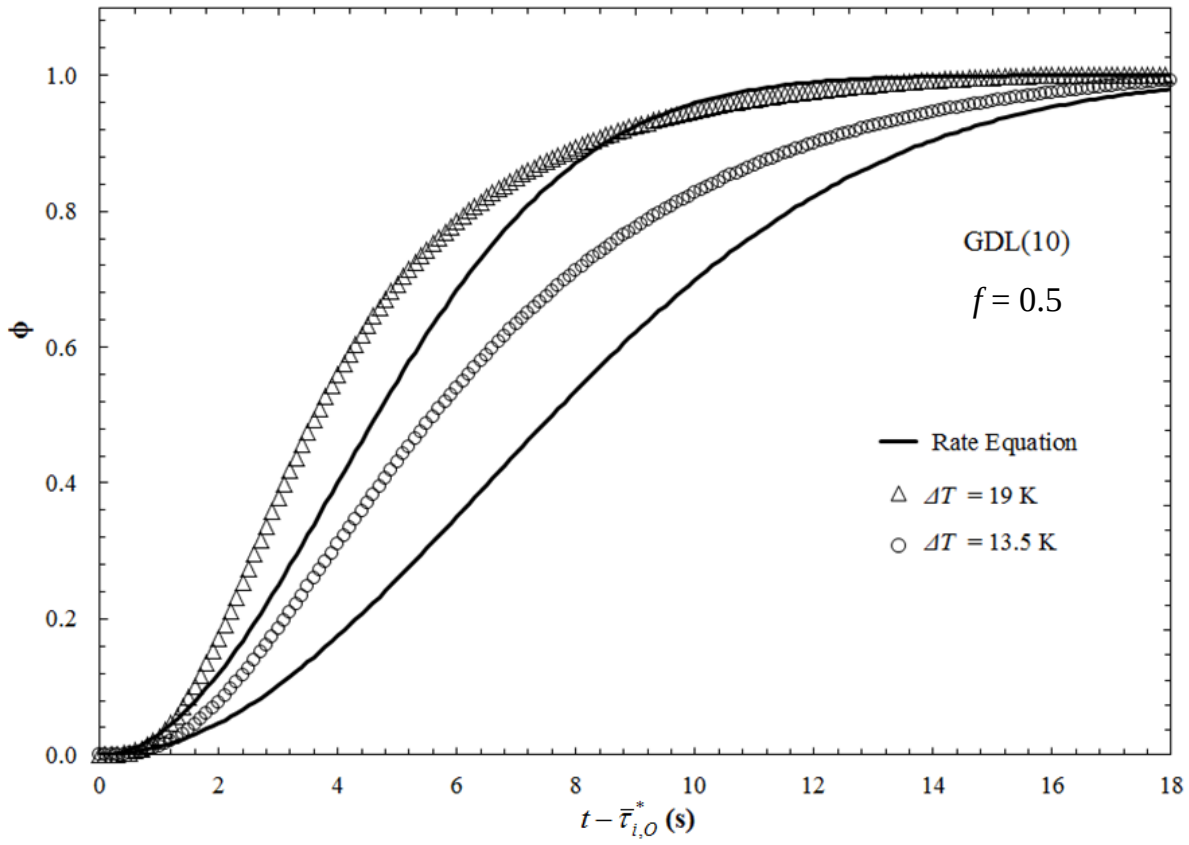

Figure 2.13. Isothermal freezing kinetics for the GDL(10) at two subcoolings. Solid lines represent theoretical predictions of ϕ using equation 2.10 and equation 2.12 for $k_O(T)$ with $\alpha_l = 1.4\times10^{-7}\,\mathrm{m^2/s}$, $\theta_o = 60°$, J_O from equation 2.17, and η_o from equation 2.9, and $f = 0.5$.

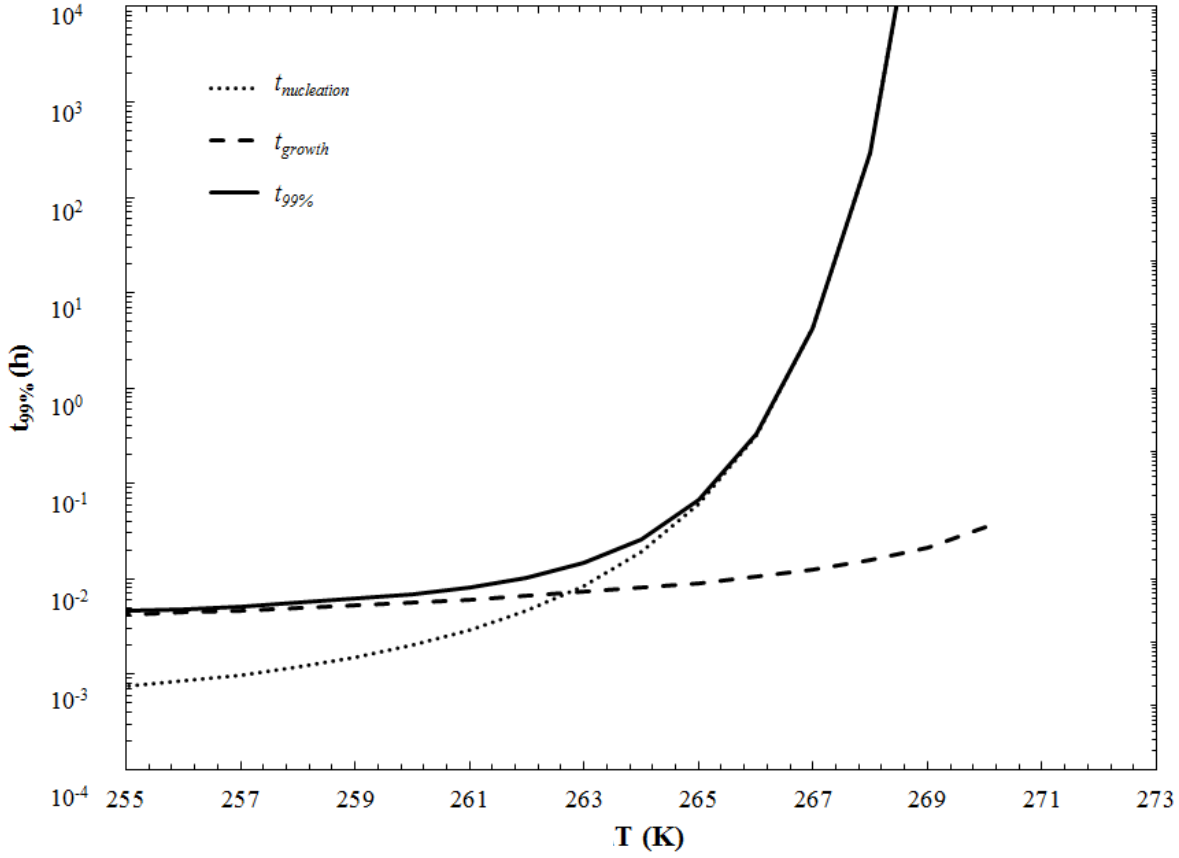

Figure 2.14. Time required for 99% crystallization as a function of temperature for the GDL(0). The dotted line estimates time required for the onset of crystallization, given by equation 2.20 with $f = 0$. The dashed line represents the time required (from the onset of crystallization) to form 99% of ice using equation 2.10 with $k_T(T) = 0$ and $k_o(T)$ given by equation 2.12. The solid line is the sum of the two dotted lines.

however, the entire range of J_O must be included. Nevertheless, because the system is nucleation limited at high temperatures, Figure 2.14 illustrates that $t_{99\%}$ is on the order of many hours. For example, at 267 K, $t_{99\%}$ is 4.2 hours. This demonstrates that the assumption of equilibrium-based freezing is not quantitative. As the nucleation rate increases, yielding smaller induction times, Figure 2.14 shows that for 243 K < T < 265 K, $t_{99\%}$ is on the order of a minute. Thus, the commonly-used assumption of equilibrium freezing is more reasonable when the temperature decreases and the system is limited by growth kinetics. Even for $T < 265\,\mathrm{K}$, however, the overall rate constant is far from infinite, suggesting the need to account for crystallization kinetics in understanding cold-start.

2.7. Conclusions

We determine pseudo-steady-state nucleation rates and crystallization rates as functions of subcooling in fuel-cell gas-diffusion layers (GDLs) using isothermal differential scanning calorimetry (DSC). Kinetic rates were measured by repeated induction times and heat-flow dynamics for two PTFE loadings (0 and 10 wt%) at temperatures between 240 and 273 K. Induction-time measurements demonstrate that nucleation is well-described by a Poisson distribution and that induction time decreases with increasing subcooling. Experimental nucleation rates and induction times follow classical nucleation theory. Both induction times and complete crystallization times increase with addition of PTFE to the GDL. Thus, both nucleation and crystal growth occur more slowly on hydrophobic fibers.

Assuming nucleation to a critical radius followed by heat-transfer-limited growth, a nonlinear ice-crystallization rate for GDLs was developed within the JMAK framework. The proposed rate equation is in good agreement with integrated DSC exotherms. Although model crystal growth rates apply specifically to small isolated crystals, the time for complete crystallization is accurately predicted in all cases. The temperature dependence of the crystallization rate is primarily a result of the nucleation rate, consistent with experimental results. As PTFE is impregnated in a GDL, both crystallization rate and induction times decrease because of a reduction in the available surface-area fraction of oxidized carbon. Although the predicted crystallization rate is accurate at subcoolings of 19, 22, and 30K, small deviations are observed at 11 and 13.5 K. These small deviations are thought to be a result of the heterogeneities of the materials and processing, coupled with the stochastic nature of crystallization.

2.8. List of Symbols

$\Delta\hat{H}_f$	heat of fusion per mass of solid (kJ/kg)
J	pseudo steady-state nucleation rate (nuclei/m^3/s)
k	overall rate constant (s$^{-2.5}$)
k_B	Boltzmann constant (J/molecule/K)
P	cumulative probability
S	liquid-water saturation
T	Temperature (K)

ΔT subcooling (K)

t time (s)

$\hat{v}$ specific volume (m^3/kg)

V volume (m^3)

$\dot{Q}$ heat-flow rate (mW)

Greek Letters

α thermal diffusivity (m^2/s)

γ surface tension (mN/m)

ε porosity

η_o thermal growth constant

θ contact angle

ρ mass density (kg/m^3)

τ induction time (s)

τ_g time for nuclei grow to an instrument detectable size (s)

ϕ volume fraction

Subscripts

o initial

l water

O oxidized carbon

s ice

T PTFE

dry dry gas-diffusion layer

2.9. Acknowledgements

This work was funded by the Assistant Secretary for Energy Efficiency and Renewable Energy, Office of Fuel Cell Technologies, of the U. S. Department of Energy under contract number DE-AC02-05CH11231. We thank the Los Alamos National Laboratory for providing the mercury-porosimetry-intrusion data and Haluna Gunterman for providing GDL SEM images.

2.10. References

[1] E. Cho, J.J. Jo, H.Y. Ha, S. Hong, K. Lee, T. Lim, I. Oh, Characteristics of the PEMFC repetitively brought to temperatures below 0 °C, J. Electrochem. Soc. 150 (2003) A1667-A1670.

[2] M. Oszcipok, D. Riemann, U. Kronenwett, M. Kreideweis, M. Zedda, Statistic analysis of operational influences on the cold start behavior of PEM fuel cells, J. Power Sources 145 (2005) 407-415.

[3] K. Tajiri, Y. Tabuchi, F. Kagami, S. Takahashi, K. Yoshizawa, C.Y. Wang, Effects of operating and design parameters on PEFC cold start, J. Power Sources 165 (2007) 279-286.

[4] S. Ge, C.Y. Wang, Cyclic voltammetry study of ice formation in the PEFC catalyst layer during cold start, J. Electrochem. Soc. 154 (2007) B1399-B1406.

[5] L. Mao, C.Y. Wang, Analysis of cold start in polymer electrolyte fuel cells, J. Electrochem. Soc. 154 (2007) B139-B146.

[6] Y. Hishinuma, T. Chikahisa, F. Kagami, T. Ogawa, The design and performance of a PEFC at a temperature below freezing, Japan Soc. Mech. Eng. Int. J. 47 (2004) 235-241.

[7] S. Ge, C.Y. Wang, Characteristics of subzero startup and water/ice formation on the catalyst layer in a polymer electrolyte fuel cell, Electrochim. Acta 52 (2007) 4825-4835.

[8] Y. Ishikawa, H. Hamada, M. Uehara, M. Shiozawa, Super-cooled water behavior inside polymer electrolyte fuel cell cross-section below freezing temperature, J. Power Sources 179 (2008) 547-552.

[9] L. Mao, C.Y. Wang, Y. Tabuchi, A multiphase model for cold start of polymer electrolyte fuel cells, J. Electrochem. Soc. 154 (2007) B341-B351.

[10] H. Meng, A PEM fuel cell model for cold-start simulations, J. Power Sources 178 (2008) 141-150.

[11] K. Jiao, X. Li, Three-dimensional multiphase modeling of cold start processes in polymer electrolyte membrane fuel cells, Electrochim. Acta 54 (2009) 6876-6891.

[12] R. Balliet, J. Newman, Cold start of a polymer-electrolyte fuel cell I. Development of a two-dimensional model, J. Electrochem. Soc. 158 (2011) B927-B938.

[13] L. Bronfenbrener, E. Korin, Kinetic model for crystallization in porous media, Int. J. Heat Mass Trans. 40 (1997) 1053-1059.

[14] L. Bronfenbrener, E. Korin, Experimental studies of water crystallization in porous media, Chem. Eng. Process. 41 (2002) 357-363.

[15] H. Zhang, J. Banfield, Kinetics of crystallization and crystal growth of nanocrystalline anatase in nanometer-sized amorphous titania, Chem. Mater. 14 (2002) 4145-4154.

[16] S.H. Kim, S.H. Ahn, T. Hirai, Crystallization kinetics and nucleation activity of silica nanoparticle-filled poly(ethylene 2,6-naphthalate), Polymer 44 (2003) 5625-5634.

[17] G.W. Scherer, Freezing gels, J. Non-Crystalline Solids 155 (1993) 1-25.

[18] T. Fen-Chong, A. Fabbri, C.R. Mecanique 333 (2005) 425-430.

[19] G. Luo, Y. Ji, C.Y. Wang, P.K. Sinha, Modeling liquid water transport in gas diffusion layers by topologically equivalent pore network, Electrochim. Acta 55 (2010) 5332-5341.

[20] J.T. Gostick, M.A. Ioannidis, M.W. Fowler, M.D. Pritzker, Wettability and capillary behavior of fibrous gas diffusion media for polymer electrolyte membrane fuel cells, J. Power Sources 194 (2009) 433-444.

[21] C. Lim, C.Y. Wang, Effects of hydrophobic polymer content in GDL on power performance of a PEM fuel cell, Electrochim. Acta 49 (2004) 4149-4156.

[22] E. Gmelin, St. M. Sarge, Calibration of differential scanning calorimeters, Pure App. Chem. 67(1995) 1789-1800.

[23] M. Avrami, Kinetics of phase change I general theory, J. Chem. Phys. 7 (1939) 1103-1112.

[24] M. Avrami, Kinetics of phase change II transformation-time relations for random distribution of nuclei, J. Chem. Phys. 8 (1940) 212-224.

[25] W.A. Johnson, R.F. Mehl, Reaction kinetics in processes of nucleation and growth, AIME Trans. 135 (1939) 416.

[26] A.N. Kolmogorov, Selected Works of A.N. Kolmogorov, vol. 1, Kluwer Academic Publishers, Dodrecht, 1985, pp. 530-560.

[27] A.F. Heneghan, P.W. Wilson, A.D. Haymet, Heterogeneous nucleation of supercooled water, and the effect of an added catalyst, PNAS 99 (2002) 9631-9634.

[28] S. Suzuki, A. Najajima, N. Yoshia, K. Okada et al., Freezing of water droplets on silicon surfaces coated with various silanes, Chem. Phys. Lett. 445 (2007) 37-41.

[29] D. Vollhardt, M. Ziller, U. Retter, Generalized nucleation-growth-collision theory for formation of lenticular centers from insoluble monolayers, Langmuir 9 (1993) 3208-3211.

[30] D.R. Uhlmann, B. Chalmers, The energetics of nucleation, Ind. Eng. Chem. 57 (1965) 19-31.

[31] D. Kashchiev, Nucleation: Basic Theory with Applications, 1st ed., Butterworth-Heinemann, Oxford, 2000, chapter 15.

[32] H.S. Carslaw, J.C. Jaeger, Conduction of Heat in Solids, 2nd ed., Oxford University Press, Oxford, 1959, chapter 11.

[33] L.I. Rubinstein, The Stefan Problem, AMS, Providence, Rhode Island, 1971, chapter 1.

[34] S. Jiang, J.H. Horst, Crystal nucleation rates from probability distributions of induction times, Crystal Growth Design 11 (2011) 256-261.

[35] D. Turnbull, J.C. Fisher, Rate of nucleation in condensed systems, J. Chem. Phys. 17 (1949) 71-73.

[36] D. Kashchiev, Induction time and metastability limit in new phase formation, J. Crystal Growth 110 (1991) 373-380.

[37] F. Feuillebois, A. Lasek, P. Creismeas, F. Pigeonneau, A. Szaniawski, Freezing of a subcooled liquid droplet, J. Colloid Interf. Sci. 169 (1995) 90-102.

[38] S.C. Hardy, A grain boundary groove measurement of the surface tension between ice and water, Philosophical Magazine 35 (1977) 471-484.

[39] P. Laval, A. Crombez, J.B. Salmon, Microfluidic droplet method for nucleation kinetics measurements, Langmuir 25 (2009) 1836-1841.

[40] B.K. Paul, M.S. Joshi, The effect of supersaturation on the induction period of potassium dihydrogen phosphate crystals grown from aqueous solution, J. Phys. D: Appl. Phys. 9 (1976) 1253-1256.

[41] J.M. Lachin, Introduction to sample size determination and power analysis for clinical trials, Controll. Clinical Trials 2 (1981) 93-113.

[42] L.M. Skinner, J.R. Sambles, The Kelvin equation - a review, J. Aerosol Sci. 3 (1972) 199-210.

Appendix 2A. Classical Nucleation Theory (CNT)

As illustrated in Figure 2.8a, ice crystallization in the gas-diffusion layer begins with nucleation, during which time critical nuclei form heterogeneously with an average nucleation rate, J (e.g., see equations 2.15 and 2.16). As stated previously, we adopt classical nucleation theory (CNT) to specify the dependence of J on ΔT. In this appendix, we review CNT thermodynamics. In Section 2A.1, we review the expression for the homogeneous Gibbs-free energy of critical-nucleus formation, ΔG^*. In Section 2A.2, we modify homogeneous nucleation theory to evaluate the heterogeneous critical Gibbs-free energy of nucleation on a flat substrate, ΔG^*_{het}. In both cases, the critical Gibbs-free energy of nucleus formation is used to calculate the average ice-nucleation rate, J, as described in Section 2.5.2 (e.g., see equations 2.15 and 2.16) [27,30,34-36,39,40].

Appendix 2A.1. Homogeneous Nucleation:

Figure 2A.1a illustrates a simple system to evaluate the homogeneous critical Gibbs-free energy of nucleation, ΔG^*, for a single component. Consider two configurations for nucleation of a solid sphere from its liquid. In state I, M molecules of liquid are placed in an inert chamber at a fixed temperature, T, and pressure, P. Similarly, in state II, $M-n$ molecules of liquid are maintained at T and P in an inert chamber, along with a solid sphere containing n molecules at T and pressure, P_S. The solid sphere and liquid in state II are not in equilibrium. We begin by writing the change in Helmholtz free energy between states I and II, ΔF. In state I, the Helmholtz free energy, F_I, is

$$F_I = M\mu_L(T,P) - PV_{L,I} \qquad \text{constant } T \qquad (2A.1)$$

whereas in state II, the Helmholtz free energy, F_{II}, is

$$F_{II} = [M-n]\mu_L(T,P) + n\mu_S(T,P_S) - P_S V_S - PV_{L,II} + \gamma_{SL}A\ , \quad \text{constant } T \qquad (2A.2)$$

where μ_i is chemical potential of phase i, V_i is volume of phase i, γ_{SL} is the solid/liquid interfacial energy, and A is interfacial surface area. Subscripts L, S, and L,I and L,II denote liquid, solid, and liquid in states I and II, respectively. Subtraction of equation 2A.1 from equation 2A.2 gives the change in Helmholtz free energy, ΔF

$$\Delta F \equiv F_{II} - F_I = -n\mu_L(T,P) + n\mu_S(T,P_S) + V_S[P-P_S] - P[V_{II}-V_I] + \gamma_{SL}A, \qquad (2A.3)$$

where $V_I = V_{L,I}$ and $V_{II} = V_{L,II} + V_S$. In this case, $V_{II} > V_I$ because the bulk density of the liquid is greater than that of the solid. For convenience, we add and subtract $n\mu_S(T,P)$ to the right side of equation 2A.3, or

$$\Delta F = -n\Delta\mu(T,P) + n[\mu_s(T,P_s) - \mu_s(T,P)] + V_s[P-P_s] - P\Delta V + \gamma_{sl}A, \qquad (2A.4)$$

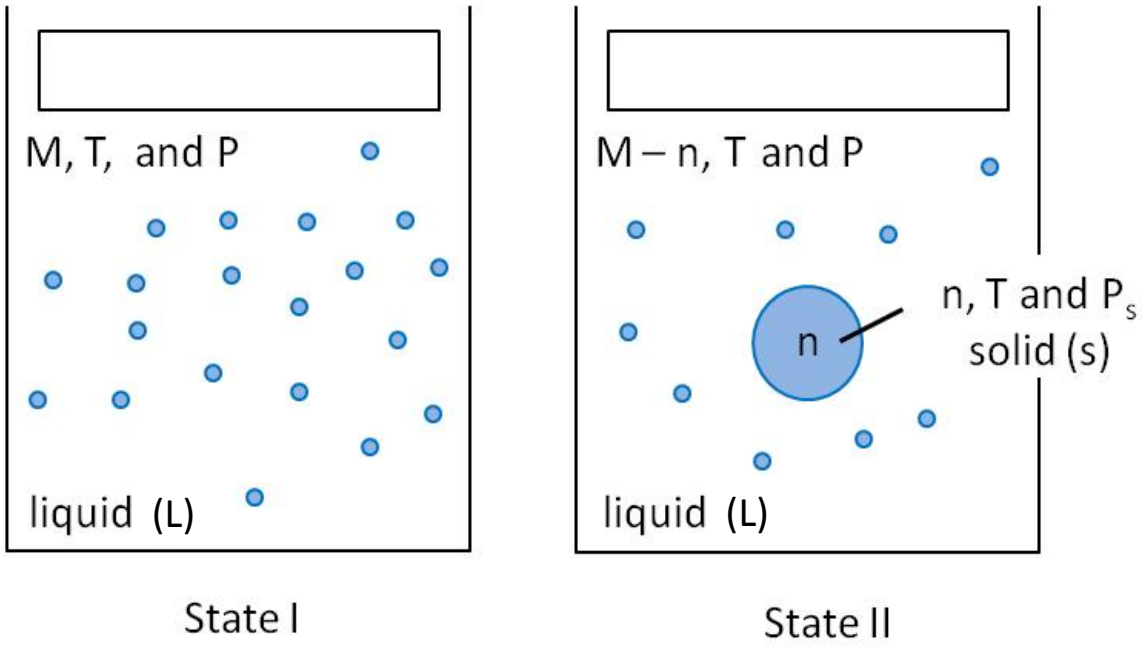

Figure 2A.1. Schematic of the thermodynamic system to calculate the homogeneous Gibbs-free energy of critical-nucleus formation, ΔG^*.

where $\Delta\mu(T,P) \equiv \mu_L(T,P) - \mu_S(T,P)$ is the supersaturation [27,30,34-36,39,40], as described in detail below. As written, $\Delta\mu(T,P)$ is a positive quantity. Upon invoking the Gibbs-Duhem equation for the solid phase (i.e., $\mu_S(T,P) - \mu_S(T,P_S) = \tilde{v}_S(P - P_S)$), equation 2A.4 simplifies to $\Delta F = -n\Delta\mu(T,P) - P\Delta V + \gamma_{SL}A$. Rewriting this expression in terms of the change in Gibbs free energy, $\Delta G = \Delta F + P\Delta V$, gives the oft-reported result that [27,30,34-36,39,40]

$$\Delta G = -n\Delta\mu(T,P) + \gamma_{SL}A. \tag{2A.5}$$

Since $\Delta\mu(T,P)$ is positive, supersaturation drives nucleation, whereas creation of new surface sets an energy barrier. Once formed, nuclei grow or decay depending on their size and the degree of supersaturation.

The solid sphere and bulk liquid in state II (Figure 2.8a) are not necessarily in phase equilibrium. Only nuclei of a critical size (i.e., critical nuclei) are in metastable equilibrium with the mother liquid. To evaluate the critical radius, r^*, and the subsequent critical Gibbs free energy of formation, ΔG^*, we maximize equation 2A.5 with respect to *r*. For a spherical nucleus, equation 2A.5 simplifies to $\Delta G = -4\pi\Delta\mu(T,P)r^3/3\hat{v}_S + 4\pi\gamma_{SL}r^2$, since $A = 4\pi r^2$ and $n = 4\pi r^3/3\hat{v}_S$. Thus, we find the classical result that

$$r^* = \frac{2\,\hat{v}_S\,\gamma_{SL}}{\Delta\mu(T,P)} \tag{2A.6}$$

and

$$\Delta G^* = -\frac{16\pi}{3}\left(\frac{\hat{v}_S\,\gamma_{SL}^{3/2}}{\Delta\mu(T,P)}\right)^2. \tag{2A.7}$$

As expected, r^* and ΔG^* in equations 2A.6 and 2A.7 decrease with increasing $\Delta\mu(T,P)$.

A cursory glance at equation 2A.6 reveals that r^* is nearly identical to the critical drop size given by the classic Kelvin equation [42]

$$r^* = \frac{2\gamma_{SL}\hat{v}_S\hat{v}_L}{\Delta\mu(\hat{v}_L - \hat{v}_S)}. \tag{2A.8}$$

In the Kelvin formalism, however, the supersaturation is defined as the difference in chemical potential of the solid with a curved and planar interface, or $\Delta\mu \equiv \mu_S(T,P_S) - \mu_S(T,P^{sat})$.We resolve this apparent inconsistency by again invoking Gibbs-Duhem in the liquid and solid phases. After simplification, we find: $(\hat{v}_L - \hat{v}_S)[\mu_S(T,P_S) - \mu_S(T,P^{sat})] = \hat{v}_L[\mu_L(T,P) - \mu_S(T,P)]$. Substituting this result into equation 2A.8 reveals that equation 2A.6 is akin to the classic Kelvin equation.

Appendix 2A.2. Heterogeneous Nucleation:

Most phase transitions occur heterogeneously due to particulate impurities and/or the presence of other surface sites [27,30,34-36,39,40]. It is, therefore, of interest to determine the heterogeneous critical Gibbs-free energy of nucleation on a flat solid substrate, ΔG^*_{het}. Consider

a solid spherical segment nucleating on a flat substrate (i.e., an oxidized-carbon fiber, denoted O) immersed in liquid, as illustrated in Figure 2.8. As before, the Helmholtz free energy of state I, F_I, is

$$F_I = M\mu_L(T,P) - PV_{L,I}\ , \qquad \text{constant } T \tag{2A.9}$$

whereas in state II, the Helmholtz free energy, F_{II}, is now

$$F_{II} = [M-n]\mu_L(T,P) + n\mu_S(T,P_S) - P_S V_S - PV_{L,II} + \gamma_{SL}A_{SL} + [\gamma_{SO} - \gamma_{SO}]A_{SO} \tag{2A.10}$$

at constant *T*, where the subscripts *SL*, *SO*, and *LO* denote solid nucleate/liquid, solid/oxidized-carbon substrate, and liquid/oxidized-carbon substrate, respectively. As discussed elsewhere [31]: $A_{LO} = \pi r^2 \sin^2\theta$, $A_{SL} = 2\pi r^2[1-\cos\theta]$, and $V_S = \pi r^3[\,2-3\cos\theta+\cos^3\theta\,]/3$. Further, $\gamma_{SL}\cos\theta = \gamma_{LO} - \gamma_{SO}$. Following the procedure outlined in Section 2A.1, after some algebra, the expressions for r^* and ΔG^*_{het} are

$$r^* = \frac{2\,\hat{v}_S\,\gamma_{SL}}{\Delta\mu(T,P)} \tag{2A.11}$$

and

$$\Delta G^*_{het} = -\frac{16\pi}{3}\left(\frac{\hat{v}_S\,\gamma_{SL}^{3/2}\,g(\theta)}{\Delta\mu(T,P)}\right)^2, \tag{2A.12}$$

where $g(\theta) = (2+\cos\theta)(1-\cos\theta)^2/4$, as discussed in Section 2.5.1 (e.g., see equation 2.5). Note that equation 2A.11 is identical to equation 2A.6 for homogeneous nucleation. Because heterogeneous nucleation generally takes place at lower supersaturations than that of homogeneous nucleation, the critical nucleus radius is, of course, different for the two cases. Equation 2A.12 reveals that $\Delta G^*_{het} = g(\theta)\Delta G^*$, reiterating that for $\theta > 0^\circ$, $\Delta G^*_{het} < \Delta G^*$ [31]. Finally, we note that equation 2A.12 is identical to that appearing in equations 2.15 and 2.16.

Chapter 3

Pseudo-Isothermal Ice-Crystallization Kinetics in the Gas-Diffusion Layer of a Fuel Cell from Differential Scanning Calorimetry

T.J. Dursch, M.A. Ciontea, G.J. Trigub, C.J. Radke, A.Z. Weber, Pseudo-isothermal ice-crystallization kinetics in the gas-diffusion layer of a fuel cell from differential scanning calorimetry, Int. J. Heat Mass Trans. 60 (*2013*) *450-458.*

3.1. Abstract

Non-isothermal ice-crystallization kinetics in the fibrous gas-diffusion layer (GDL) of a proton-exchange-membrane fuel cell is investigated using differential scanning calorimetry (DSC). Non-isothermal ice-crystallization rates and ice-crystallization temperatures are obtained from heat-flow measurements in a water-saturated commercial GDL at cooling rates of 2.5, 5, 10, and 25 K/min. Our previously developed isothermal ice-crystallization rate expression is extended to non-isothermal crystallization to predict ice-crystallization kinetics in a GDL at various cooling rates. Agreement between DSC experimental results and theory is good. Both show that as the cooling rate increases, ice-crystallization rates increase and crystallization temperatures decrease monotonically. Importantly, we find that the cooling rate during crystallization has a negligible effect on the crystallization rate when crystallization times are much faster than the time to decrease the sample temperature by the subcooling. Based on this finding, we propose a pseudo-isothermal method for obtaining non-isothermal crystallization kinetics using isothermal crystallization kinetics evaluated at the non-isothermal crystallization temperature.

3.2. Introduction

Proton-exchange-membrane fuel cells (PEMFCs) reduce oxygen to water in the cathode catalyst layer (cCL). Under subfreezing conditions, water solidifies and hinders access of oxygen to the catalytic sites in the cCL, severely inhibiting cell performance and potentially causing cell failure [1]. Recently, using isothermal differential scanning calorimetry (DSC), we show that the rate at which ice forms in the fibrous gas-diffusion layer (GDL) of a PEMFC depends strongly on temperature and medium wettability [2]. Therefore, detailed knowledge of ice-crystallization kinetics within PEMFC media is needed. To date, ice-crystallization kinetics in the GDL have been analyzed only under isothermal conditions. However, ice-formation kinetics must be considered under experimental settings similar to actual PEMFC operating conditions where ice invariably forms non-isothermally.

DSC is a conventional apparatus to obtain crystallization kinetics [2-7]. In DSC, the rate of a phase transition is determined by measuring heat released or absorbed by a sample over time. When crystallization experiments are performed isothermally, the resulting exotherms are directly integrated to provide crystallization rates [2-7]. For non-isothermal DSC, however, coupling of the crystallization rate with internal heat transfer makes interpretation difficult. As a result, several models have been presented to describe crystallization and heat transfer within a DSC under non-isothermal conditions [3, 8, 9]. In these treatments, non-isothermal DSC

exotherms are predicted from a semi-empirical kinetic expression in conjunction with an overall energy balance [3, 8, 9], despite the availability of crystallization kinetics via the Johnson-Mehl-Avrami-Kolmogorov (JMAK) formalism [10-13]. Available models highlight the effects of heat transfer on crystallization and show good agreement with experiment. In the analyses, however, an empirical crystallization rate constant with an Arrhenius-temperature dependence is employed, neglecting contributions from both nucleation and growth processes. Similar to JMAK theory, in polymer crystallization, the Hoffman-Lauritzen equation combines nucleation and growth to obtain an overall crystallization rate constant from non-isothermal DSC data [14-16]. This equation, unfortunately, is limited to polymer crystallization.

In this work, we extend previous isothermal ice-crystallization kinetics in the GDL of a PEMFC [2] based on JMAK theory to non-isothermal crystallization where the DSC furnace temperature decreases in time. Experimental non-isothermal ice-crystallization rates and ice-crystallization temperatures are obtained from DSC heat-flow measurements in a water-saturated Toray GDL at cooling rates of 2.5, 5, 10, and 25 K/min. Our previously developed isothermal ice-crystallization rate expression [2] is extended to non-isothermal crystallization, allowing prediction of DSC crystallization exotherms in GDLs at various cooling rates.

3.3. Materials and Methods

3.3.1. GDL Sample Preparation:

Water-wetting TGP-H-060 carbon-paper GDLs were provided by Toray (Toray Corp., Tokyo, Japan). Relevant material properties are listed in Table 3.1. GDL samples were bored into 3.75-mm diameter circles and saturated with Ultrapure Milli-Q® (Millipore, Billerica, MA) distilled/deionized water in a home-built vacuum chamber for 45 min at 4.7 kPa. Excess surface water was blotted with Fisherbrand® (Fisher Scientific, Pittsburg, PA) weighing paper. Water content was determined gravimetrically. Measured values were consistent with integrated peak areas generated from DSC. Water loss by evaporation during DSC was negligible. Additionally, capillary pressure-saturation measurements showed that water does not drain from the GDLs under atmospheric pressure [17].

Table 3.1. GDL Properties

GDL	Thickness (μm)	PTFE (wt %)	Porosity, ε	Water Saturation, S_w
Toray	190	0	[a]80.0 %	[b]84±3 %

[a] Mercury-intrusion-porosimetry data provided by Los Alamos National Laboratory.

[b] Calculated according to Lim and Wang [32]

3.3.2. Differential Scanning Calorimetry:

A PerkinElmer 6000 DSC (PerkinElmer Inc., Waltham, MA) with a liquid-nitrogen chiller detected the heat-flow rate from the sample over time. The DSC was calibrated against the known melting points of 99.999% indium (429.78 K) and zinc (692.68 K) (PerkinElmer Inc., Waltham, MA), as well as dodecane (263.55 K) (Sigma Chemical Co., St. Louis, MO) for lower

temperatures. Heat flow to the calorimeter was calibrated using the heat of fusion of indium (28.47 J/g) following Gmelin and Sarge [18]. Nitrogen at a flow rate of 20 mL/min served as the purge gas. Water-saturated GDL samples, weighing between 1 and 5 mg, were placed into 20-µL PerkinElmer hermetically-sealed aluminum pans.

Non-isothermal crystallization was carried out over the temperature range of 240 to 273 K. Water-saturated GDL samples were placed into the DSC at 300 K and cooled to 240 K at constant cooling rates of 2.5, 5, 10, and 25 K/min. A preliminary cooling and heating cycle at a rate of 10 K/min erased the thermal history of the sample, and was not included in the data analysis. Unless otherwise stated, reported results represent the average of two samples. In all experiments, the sample temperature and DSC heat-flow rate were recorded as functions of time and programmed temperature.

Figure 3.1 shows a typical crystallization exotherm of heat-flow rate (solid line), $\dot{Q}$, and sample temperature (dashed line), T_S, versus time for a water-saturated GDL. The sample was cooled at 5 K/min from 293 K to 240 K. Crystallization commenced at approximately 257.8 K (point A in Figure 3.1), defined as the crystallization temperature, T_C. Heat flow due to liberation of the enthalpy of crystallization from point A is evident until a maximum is observed at point B, after which crystallization slows significantly until complete freezing at point C. To obtain the gas-free volume fraction of ice within the GDL pores, ϕ, as a function of time, crystallization exotherms were integrated from point A to point C according to the expression

$$\phi = \frac{\int_0^t \dot{Q}(t)dt}{\int_0^\infty \dot{Q}(t)dt} \tag{3.1}$$

where $\dot{Q}(t)$ is the heat-flow rate (mW) from the DSC. Crystallization in Figure 3.1 is preceded by a non-isothermal induction time, τ_I, corresponding to the crystallization temperature, T_C. We define τ_I as the time elapsed between when the sample temperature reaches 273 K and the onset of crystallization, approximately 168 s (point A) in Figure 3.1.

For each exotherm, the initial mass of water present, $m_{w,o}$, is calculated by

$$m_{w,o} = -\frac{1}{\beta \Delta \hat{H}_f} \int_{T_F(\tau_I)}^{T_F(t_{99\%})} \dot{Q}_a\left(T_F(t)\right) dT_F \tag{3.2}$$

where $T_F(\tau_I)$ is the furnace temperature at the crystallization onset, $T_F(t_{99\%})$ is the furnace temperature at complete crystallization defined below, β is the cooling rate (K/min), $\Delta \hat{H}_f$ is the enthalpy of fusion (taken as positive), and $\dot{Q}_a$ is heat-flow rate adjusted by subtracting the baseline heat-flow rate, $\dot{Q}_B(t)$, or $\dot{Q}_a = \dot{Q} - \dot{Q}_B(t)$. Agreement is excellent between the water mass calculated from equation 3.2 and the gravimetric water content of the sample.

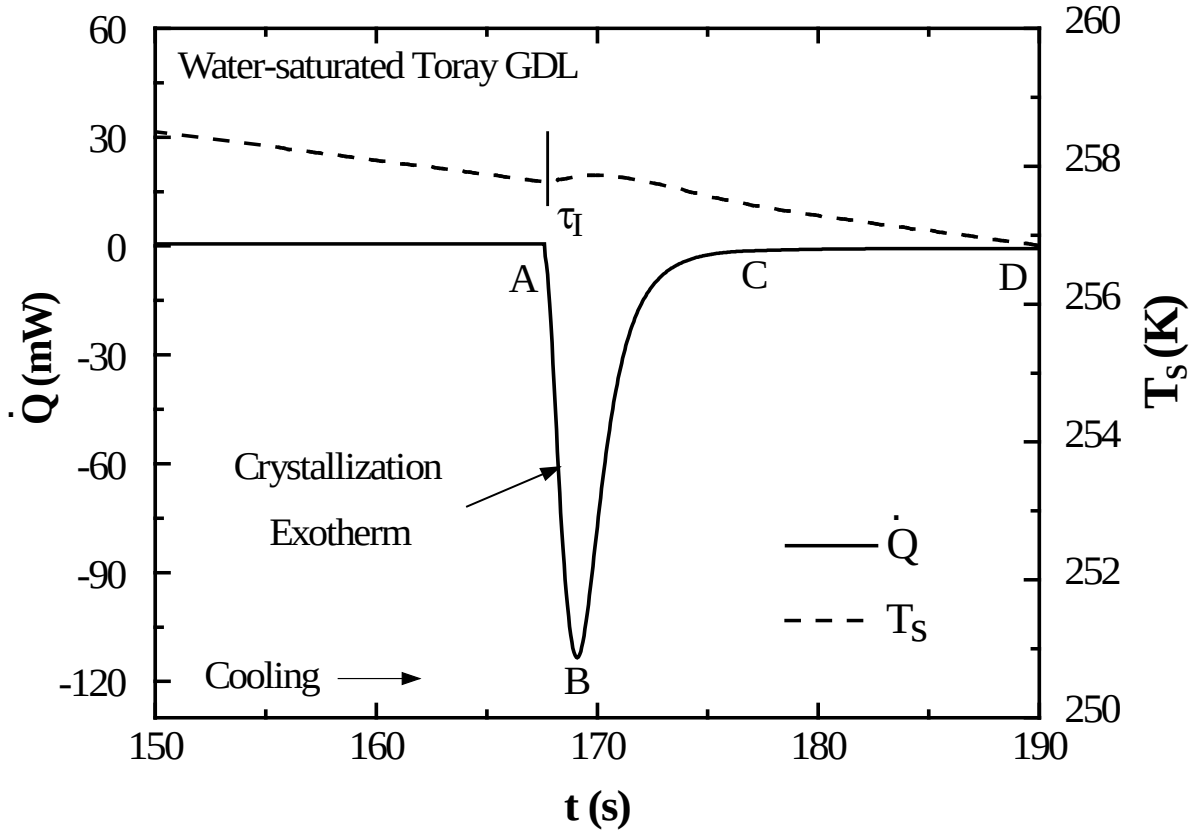

Figure 3.1. Typical non-isothermal DSC cooling exotherm of a water-saturated GDL, cooled at a rate of 5 K/min to 240 K. The solid line corresponds to heat-flow rate, whereas the dashed line represents the sample temperature. τ_I denotes the non-isothermal induction time, defined as the time from 273 K to point A. Points A-C label the onset, extremum, and completion of water freezing, respectively. Point D labels the final baseline heat-flow rate, $\dot{Q}_{Bf}$.

3.4. Experimental Results

Figure 3.2 shows measured ice-crystallization exotherms (filled symbols) of heat-flow rate versus furnace temperature, T_F, at cooling rates, β, of 2.5, 5, 10, and 25 K/min. Lines in Figure 3.2 correspond to theory discussed below. As β increases from 2.5 to 25 K/min, crystallization exotherms both broaden and reach greater peak heat-flow rates, consonant with identical water mass in each sample and equation 3.2. Concomitantly, the number-average crystallization temperature, $\overline{T}_C$, decreases from 264.2 to 259.2 K (not shown in Figure 3.2), and the final baseline heat-flow rate (taken as point D in Figure 3.1), $\dot{Q}_{Bf}$, increases from 0.33 to 3.2 mW (not seen on the scale of Figure 3.2). For ease of comparison, final baseline heat-flow rates are listed in Table 3.2. A similar dependence of final baseline heat-flow rate on β is reported elsewhere [19-21]. The observed trends are examined in greater detail below.

To quantify the effect of β on the non-isothermal crystallization temperature, T_C-measurements were performed for three separate Toray GDLs. Filled symbols in Figures 3.3 and 3.4 display number-average $\overline{\tau}_I$ and $\overline{T}_C$ values measured at cooling rates of $\beta = 2.5$, 5, 10, 25, and 50 K/min. Solid lines in Figures 3.3 and 3.4 correspond to theory as discussed below. As β increases, both $\overline{\tau}_I$ and $\overline{T}_C$ decrease monotonically. Higher cooling rates yield lower crystallization temperatures and smaller non-isothermal induction times. Similar monotonic dependences of $\overline{\tau}_I$ and $\overline{T}_C$ on β are reported for polymer crystallization [3, 4, 7, 22-24].

Error bars reported at 10 K/min in Figures 3.3 and 3.4 correspond to the observed range of 16 repeated T_C and τ_I measurements. The statistical nature of the induction process results in a Poisson distribution for single-τ_i measurements [2]. Since a single τ_i corresponds to a given crystallization temperature, T_C values are similarly Poisson distributed. Figure 3.5 displays 16 measured T_C values for a Toray GDL cooled at 10 K/min, where the dotted line indicates the number-average crystallization temperature, $\overline{T}_C$. Generally, T_C lies below the mean with intermittent excursions to high temperatures. Significantly, Figure 3.5 shows that T_C can vary by as much as 4 K at a cooling rate of 10 K/min. Unfortunately, the distribution of crystallization temperatures is often ignored [3, 4, 7, 14, 22, 25].

Table 3.2. Final Baseline DSC Heat-flow Rates, $\dot{Q}_{Bf}$

β (K/min)	$\dot{Q}_{Bf,\exp}$ (mW)	$\dot{Q}_{Bf,theory}$ (mW)
2.5	0.33	0.37
5	0.64	0.71
10	1.28	1.42
25	3.55	3.63

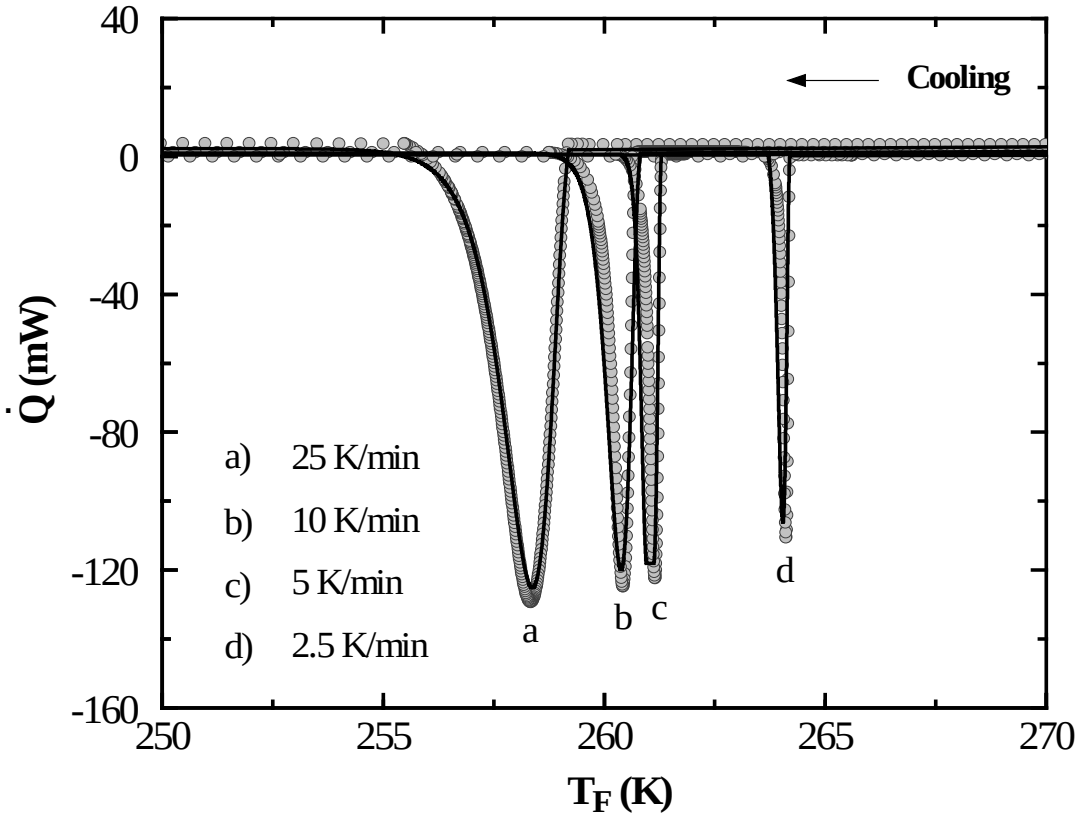

Figure 3.2. Measured and predicted non-isothermal DSC cooling exotherms as a function of furnace temperature, T_F, for a water-saturated Toray GDL at cooling rates of $\beta = 2.5$, 5, 10, and 25 K/min. Filled symbols are measured exotherms, whereas solid lines are predicted exotherms as described in Appendix 3B.

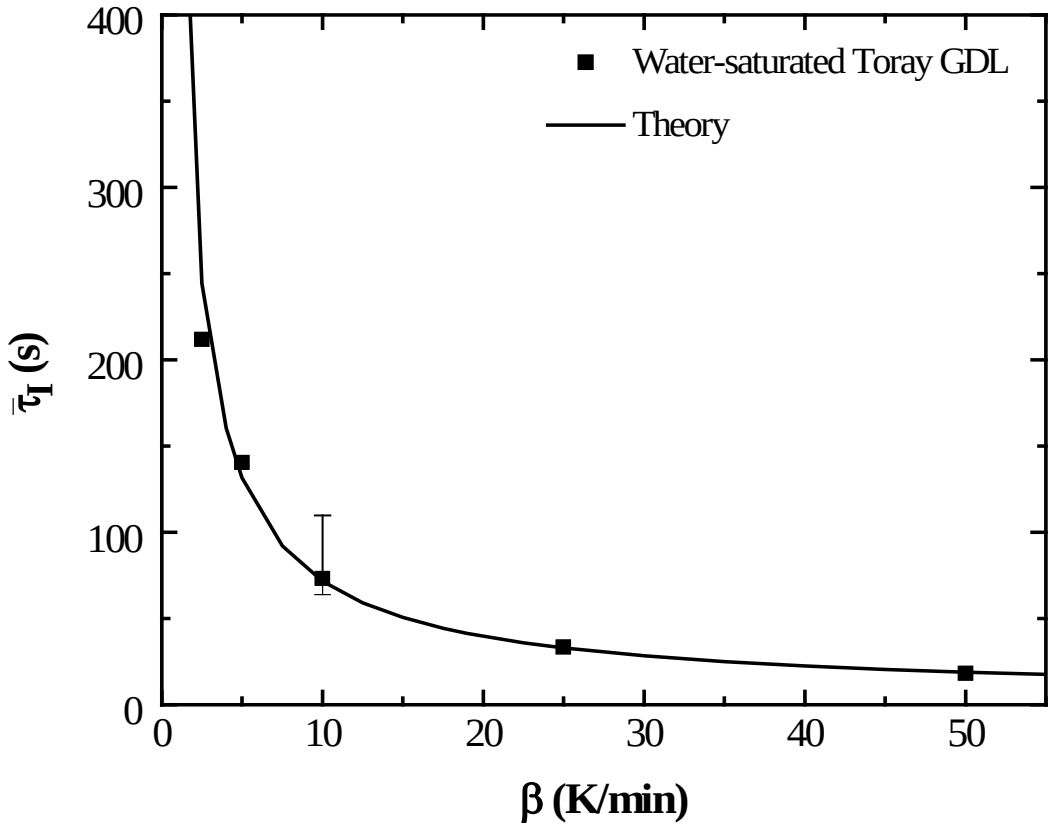

Figure 3.3. Average non-isothermal induction time, $\bar{\tau}_I$, as a function of cooling rate, β. Filled symbols are measured non-isothermal induction times averaged over three water-saturated Toray GDLs. The solid line is a prediction of $\bar{\tau}_I$ using equations 3.6, 3.16, and 3.17, with $A = 9.1\times10^{7}$ nuclei $m^{-3}\,s^{-1}$ and $B = 1.1\times10^{5}\ K^{3}$. The error bar indicates the range of observed induction times for 16 repeated τ_I-measurements on a single Toray GDL.

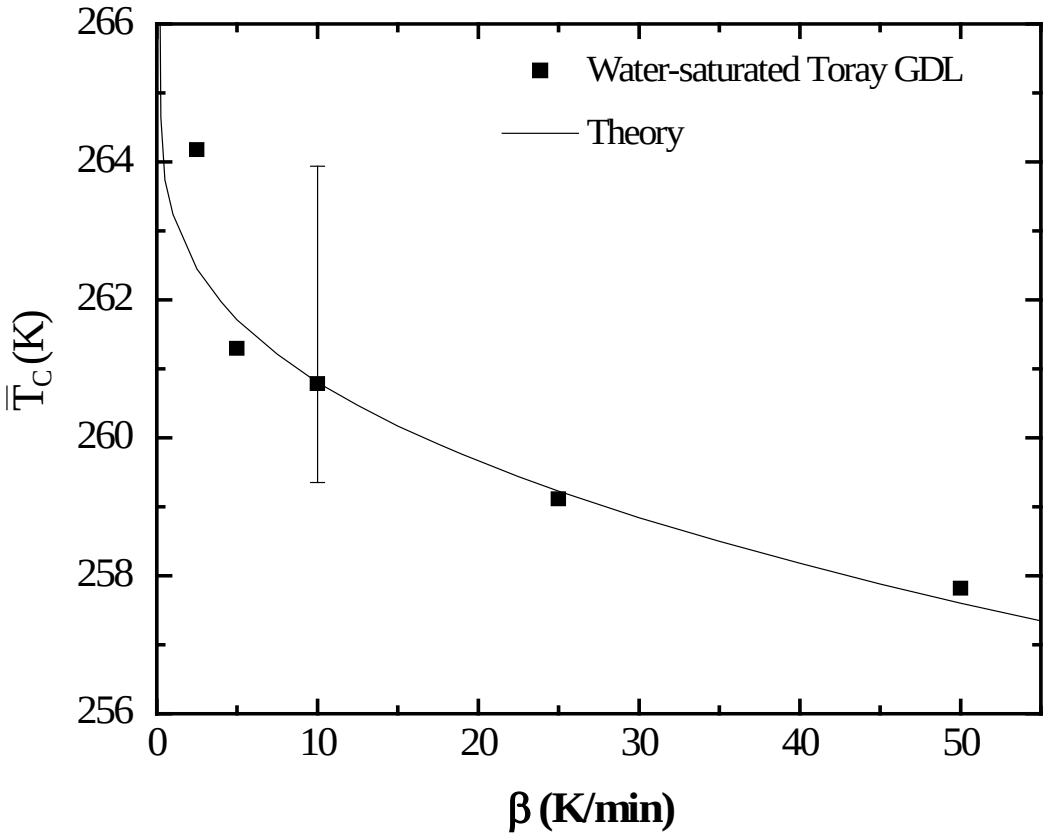

Figure 3.4. Average non-isothermal crystallization temperature, $\overline{T}_C$, as a function of cooling rate, β. Filled symbols are measured $\overline{T}_C$ values averaged over three water-saturated Toray GDLs. The solid line is a prediction of $\overline{T}_C$ using equation 3.6 with $\overline{\tau}_I$ from Figure 3.3, i.e., the sample temperature evaluated at the non-isothermal induction time, $\overline{\tau}_I$. The error bar indicates the range of observed crystallization temperatures for 16 repeated T_C-measurements on a single Toray GDL.

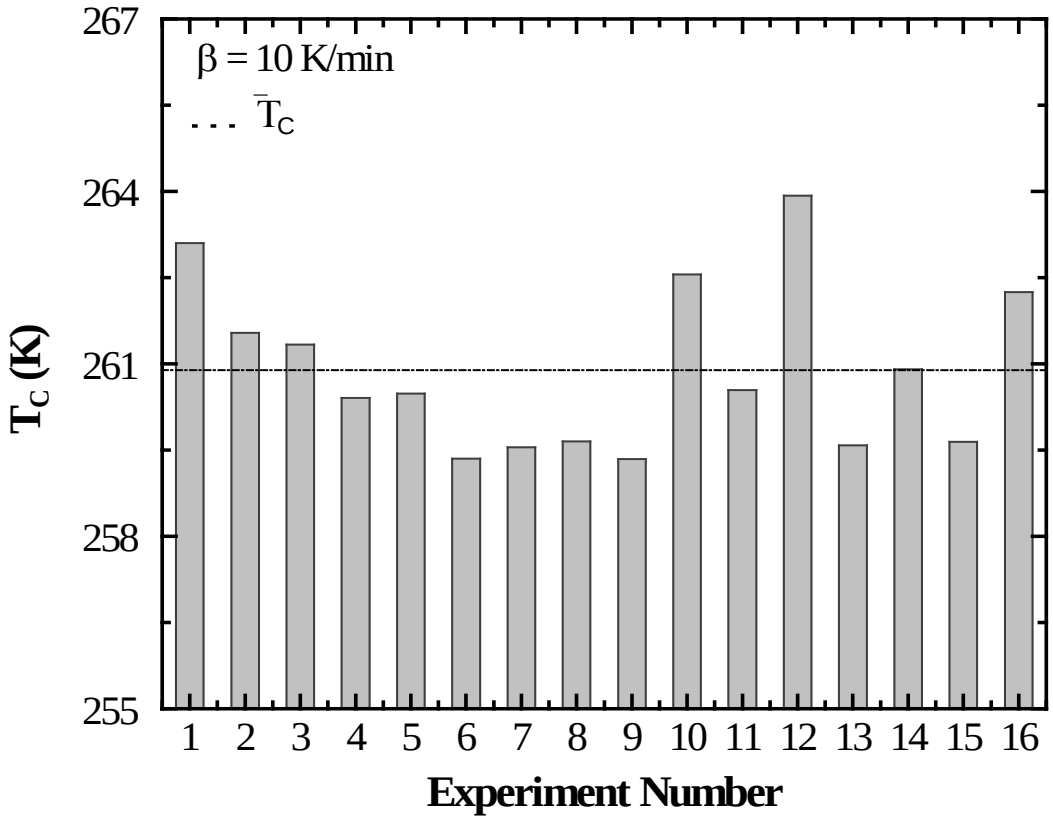

Figure 3.5. 16 crystallization-temperature measurements at a cooling rate of 10 K/min for a water-saturated Toray GDL. The horizontal dash-dotted line indicates the number-average crystallization temperature, $\bar{T}_C$.

Plotting $\dot{Q}$ versus T_F, although common [3, 4, 7, 14, 22], makes it difficult to compare complete crystallization times among exotherms. Since the furnace temperature depends directly on the cooling rate, a graph of $\dot{Q}$ versus T_F stretches the exotherm by the respective cooling rate. Consequently, complete crystallization times are best obtained by ascertaining the fractional crystallization, $\phi(t)$, from equation 3.1, as a function of time. Figure 3.6 shows $\phi(t)$ as filled symbols, obtained from the measured exotherms for cooling rates of 2.5, 5, 10, and 25 K/min, respectively. Solid, dashed, dash-dotted, and dotted lines are non-isothermal $\phi(t)$ predictions discussed below. At each cooling rate, τ_I was subtracted from the total time so that all curves are compared on a single time scale. Complete crystallization times are taken as the time required after the induction time to transform 99% of the initial water to ice. In Figure 3.6, measured complete crystallization times are 10.5, 7.8, 6.5, and 5.7 s for cooling rates of 2.5, 5, 10, and 25 K/min, respectively. Thus, as β increases, the time for complete crystallization decreases monotonically.

3.5. Non-isothermal DSC Theory

We desire quantitative prediction of DSC-measured non-isothermal ice-crystallization kinetics within a GDL. Sample temperature, T_S, and DSC heat-flow rate, $\dot{Q}$, are determined by solving overall energy balances, using a non-isothermal ice-crystallization rate expression based on the Johnson-Mehl-Avrami-Kolmogorov (JMAK) formalism [2].

Heat transfer within a DSC has been thoroughly investigated [8, 9, 14, 26]. Sample and reference pans in a DSC are placed onto separate highly-conductive aluminum platforms and encased in a furnace. Using a liquid-nitrogen chiller, the furnace temperature, T_F, is lowered at a programmed linear rate

$$T_F = T_{Fo} - \beta\, t \tag{3.3}$$

where T_{Fo} is the initial furnace temperature and β is the cooling rate (K/min). Instrument-reported heat-flow rate, $\dot{Q}$(mW), is given by the temperature difference between the sample and reference pans [26]

$$\dot{Q} = UA_p(T_S - T_R) \tag{3.4}$$

where U is the overall heat transfer coefficient, A_p is the pan area in contact with the DSC platform, T_S is the sample temperature, and T_R is the reference or empty-pan temperature.

Following Eder [4] and Wu et al. [8], energy balances describe the temperatures of the reference and sample pans, respectively

$$m_p \hat{C}_{p,p} \frac{dT_R}{dt} = UA_p(T_F - T_R), \tag{3.5}$$

$$(m_{cf}\hat{C}_{p,cf} + m_{w,o}\hat{C}_{p,w} + m_p\hat{C}_{p,p})\frac{dT_S}{dt} = UA_p(T_F - T_S) \qquad \text{for } t < \tau_I, \tag{3.6}$$

and

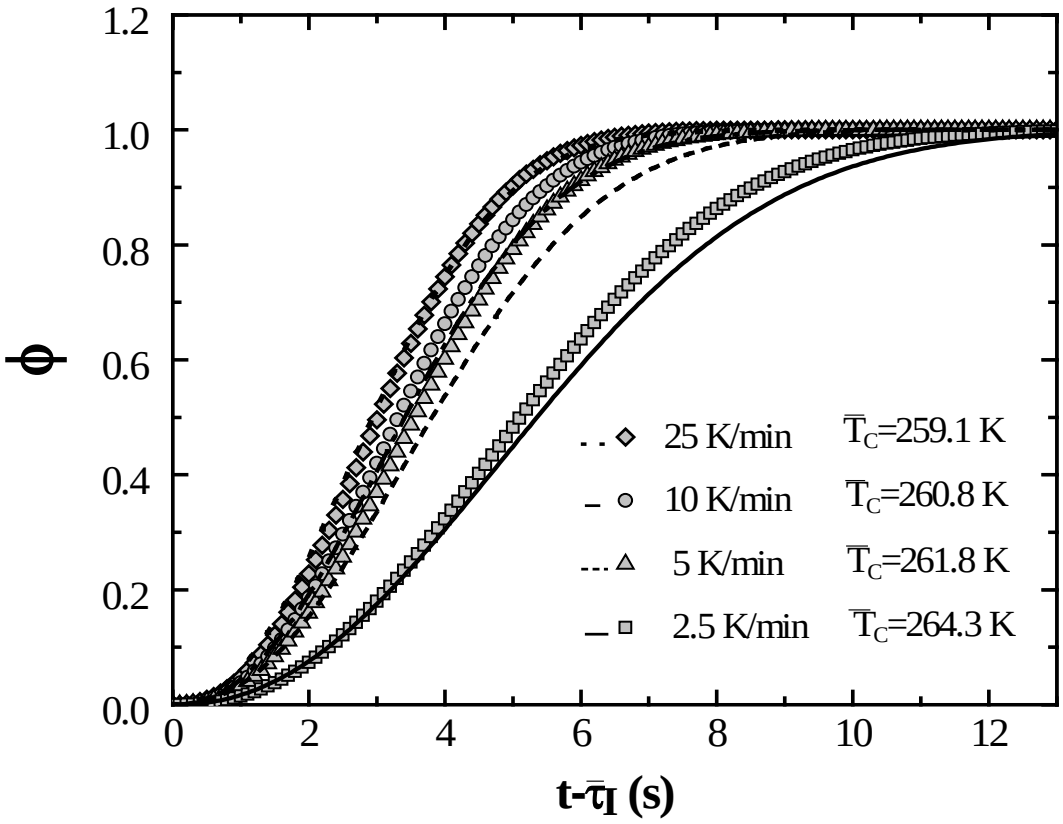

Figure 3.6. Average non-isothermal freezing kinetics for three water-saturated Toray GDLs at cooling rates of $\beta = 2.5$, 5, 10, and 25 K/min. The gas-free volume fraction of ice within the GDL pores, ϕ, is calculated using equation 3.1 for the exotherms in Figure 3.2. Dotted, dash-dotted, dashed, and solid lines are predicted using equation 3.15, as detailed in Appendix 3B. Measured $\bar{\tau}_I$ and $\overline{T_C}$ values are from Figures 3.3 and 3.4, respectively.

$$(m_{cf}\hat{C}_{p,cf} + m_p\hat{C}_{p,p} + m_{w,o}\hat{C}_{p,w}(1-\phi) + \frac{m_{w,o}\hat{C}_{p,i}\rho_i}{\rho_w}\phi)\frac{dT_S}{dt} = UA_p(T_F - T_S) + \frac{m_{w,o}\rho_i}{\rho_w}\Delta\hat{H}_f R_i \quad \text{for } t \geq \tau_I \qquad (3.7)$$

where m is mass, $m_{w,o}$ is initial water mass, $\hat{C}_p$ is heat capacity per unit mass, $\Delta\hat{H}_f$ is the latent heat of fusion per unit mass (taken as positive), τ_I is the non-isothermal induction time, and R_i is the rate of ice formation (generated ice volume/water plus ice volume per unit time). Subscripts *S*, *R*, *p*, *cf*, *w*, and *i* denote sample, reference, aluminum pan, carbon fibers, water, and ice, respectively. In equation 3.7, we assume that $\rho_w \sim \rho_i$ and $\hat{C}_{p,w} \sim \hat{C}_{p,i}$. Additionally, heat transfer to the purge gas is neglected [26]. The product UA_p is obtained by DSC calibration using indium, as described in Appendix 3A [3, 8].

The second term on the right in equation 3.7 reflects the ice-formation rate, R_i, which in the closed sample pan follows from

$$(1-S_g)R_i = \frac{d[(1-S_g)\phi]}{dt} \qquad (3.8)$$

where ϕ is the gas-free volume fraction of ice within the GDL pores, S_g is the gas saturation, and R_i has dimensions of ice volume/initial water volume/time. In a DSC experiment, S_g is constant, and equation 3.8 reduces to $R_i = d\phi/dt$. Using a heat-transfer-limited growth rate [2], $\phi(t)$ is well-described by JMAK theory and is determined by a convolution integral over nucleation and growth rates [2, 10-13]

$$\phi(t) = 0 \quad \text{for } t < \tau_I, \qquad (3.9)$$

and

$$\phi(t) = 1 - \exp\left(-\frac{4\pi}{3}g(\theta)\int_{\tau_I}^{t} J(t')\,r^3(t-t')dt'\right) \quad \text{for } t \geq \tau_I, \qquad (3.10)$$

where [2, 27]

$$g(\theta) = \frac{1}{4}(2+\cos\theta)(1-\cos\theta)^2, \qquad (3.11)$$

J is the pseudo-steady-state nucleation rate (nuclei m^{-3} s^{-1}), r is the growing nucleus radius as a function of time *t*. Equation 3.10 accounts not only for nucleation and growth, but also for impingement of the growing nuclei (i.e., size exclusion). In equation 3.10, nuclei are assumed to form at a time, *t'*, and grow as spherical caps from *t'* to *t*, with a contact angle, θ, defined through the ice phase.

J and r in equation 3.10 depend implicitly on time through the sample temperature, $T_S(t)$. Our previous isothermal DSC measurements (see Chapter 2) show that the temperature dependence of J, interpreted from classical nucleation theory, is [2]

$$J(T_S) = A\exp\left(\frac{-B}{T_S(T_o - T_S)^2}\right) \tag{3.12}$$

where $T_o = 273$ K, and A and B are constants discussed below. For heat-transfer-limited growth, $r(t)$ is described by the Stefan problem [2, 28, 29]

$$r(t) = 2\eta_o\sqrt{\alpha_w t} \tag{3.13}$$

where α_w is the liquid thermal diffusivity, and η_o is a dimensionless temperature-dependent growth parameter given by [2, 28, 29]

$$\eta_o^2 \exp\left(\eta_o^2\right)\left[\exp\left(-\eta_o^2\right) - \sqrt{\pi}\eta_o erf\left(\eta_o\right)\right] = \frac{Ste}{2} \tag{3.14}$$

where $Ste = \hat{C}_{p,w}\Delta T / \Delta\hat{H}_f$ is the Stefan number. Substitution of equation 3.13 into equation 3.10 gives an integral expression for the gas-free volume fraction of ice within the GDL pores

$$\phi(t) = 1 - \exp\left(-\frac{32\pi}{3}\alpha_w^{3/2} g(\theta) \int_{\bar{\tau}_I}^{t} J\left(T_S(t')\right)\, \eta_o^3\left(T_S(t-t')\right)\, \left(t-t'\right)^{3/2}\, dt'\right) \tag{3.15}$$

where the temperature dependencies of J and η_o are given by equations 3.12 and 3.14, respectively.

Equation 3.15 applies only after the number-average non-isothermal induction time, $\bar{\tau}_I$. To determine $\bar{\tau}_I$, the approach of Sifleet et al. [18] is adopted in which $\bar{\tau}_I$ is approximated by a series of infinitesimal isothermal time steps

$$\int_0^{\bar{\tau}_I} \frac{dt}{\bar{\tau}_i(T_S(t))} = 1 \tag{3.16}$$

where $\bar{\tau}_i(T_S(t))$ is the isothermal induction time as a function of the sample temperature. In equation 3.16, dt is the time interval of a single isothermal increment corresponding to an average isothermal induction time, $\bar{\tau}_i(T_S(t))$. Division of dt by $\bar{\tau}_i(T_S(t))$ provides the fractional contribution to $\bar{\tau}_I$ of each time increment. The non-isothermal induction time is reached when the fractional contributions integrate to unity.

For three-dimensional, heat-transfer-limited growth, the temperature dependence of $\bar{\tau}_i$ in equation 3.16 is specified by

$$\bar{\tau}_i = \frac{\rho_w}{J(T_S)m_{w,o}} + \left(\frac{15\omega}{64\pi g(\theta) J(T_S)\eta_0^3(T_S)\alpha_w^{3/2}}\right)^{2/5} \tag{3.17}$$

where ω is an instrument-specific constant representing the first measurable heat released from a frozen volume fraction of initial liquid [28]. Equation 3.17 from Kashchiev [30] is a more global form of our previous approach [2] (i.e., see equation 2.18), where the first term in equation 3.17 is the expectation time for the appearance of a critical nucleus and the second term

is the time required for critical nuclei to form and grow to a size detectable by the DSC ($\bar{\tau}_g$ in equation 2.18). From previously measured $\bar{\tau}_g(T)$ values [2], the second term in equation 3.17 establishes $\omega = 0.0173$ for our instrument. The second term in equation 3.17 then accounts for approximately 10 to 25 % of $\bar{\tau}_i$.

3.5.1. Numerical Solution:

The coupled integro-differential equations 3.5-3.8, 3.10, 3.12, and 3.14-3.17 are solved numerically using a forward Euler marching scheme in Matlab R2010a (The Math Works Inc., Natick, MA) using a time step of 10^{-4} s, as described in Appendix 3B. Equations are solved in two time regimes. First, prior to crystallization, the energy balances, equations 3.5 and 3.6, and the induction-time relations, equations 3.16 and 3.17, are solved to provide the average non-isothermal induction time, $\bar{\tau}_I$, and the corresponding average crystallization temperature, $\overline{T_C}$, at a given cooling rate. Second, during crystallization, the energy balances in equations 3.5 and 3.7 are solved in conjunction with the non-isothermal ice-crystallization rate, equation 3.15 substituted into equation 3.8. During each time period, sample temperature and DSC heat-flow rate are calculated as functions of time.

3.6. Discussion

3.61. Model Comparison to Experiment:

Lines in Figure 3.2 show predicted ice-crystallization exotherms of heat-flow rate versus furnace temperature at cooling rates of $\beta = 2.5$, 5, 10, and 25 K/min. All model parameters were independently evaluated from experimental data and are listed in Table 3.3. Overall, theory and

Table 3.3. Model Parameters

	Aluminum Pan	**Water**	**Carbon Fibers**	**Saturated GDL**
m (mg)	24.5	1.3	1.1	27.1
$\hat{C}_p$ (J kg^{-1} K^{-1})	910	4210	710	_
$\Delta\hat{H}_f$ (kJ kg^{-1})	_	335.6	_	_
k_{th} (W m^{-1} K^{-1})	250	0.9	1.7	_
UA_p (W K^{-1})	–	–	–	0.035
A_p (mm^2)	9.6	9.6	9.6	9.6
A (nuclei m^{-3} s^{-1})	_	9.1×10^{7}	_	_
B (K^3)	_	1.1×10^{5}	_	_

experiment are in excellent agreement. With no adjustable parameters, all observed trends are quantitatively explained below using the proposed crystallization/heat transfer model.

In Figure 3.2, the final base-line heat-flow rate, $\dot{Q}_{Bf}$, increases from 0.33 to 3.35 mW as β increases from 2.5 to 25 K/min. Similarly, predicted values, using equation 3.4 and listed as $\dot{Q}_{Bf,theory}$ in Table 3.2, increase from 0.37 to 3.63 mW, in quantitative agreement with measured values. A simple analytical expression for $\dot{Q}_B(t)$ (valid between points C and D in Figure 3.1) is available in equation 3C.1 of Appendix 3C. As t approaches infinity after complete crystallization (point D in Figure 3.1), equation 3C.1 reduces to

$$\dot{Q}_{Bf} = \beta\left(m_{cf}\hat{C}_{p,cf} + m_i\hat{C}_{p,i}\rho_i/\rho_w\right). \tag{3.18}$$

Equation 3.18 reveals that the baseline heat-flow rate increases linearly as β increases. Thus, for constant thermal mass, the ratio of final baseline heat-flow rates is simply equal to the ratio of the cooling rates. From Table 3.2, the measured baseline heat-flow rate ratios are 1.94 (from 2.5 to 5 K/min), 2.01 (from 5 to 10 K/min), and 2.61 (10 to 25 K/min), in good agreement with equation 3.18. Additionally, the predicted dependence of $\dot{Q}_{Bf}$ on both thermal mass and cooling rate in equation 3.18 was confirmed using empty aluminum DSC pans. A similar expression for $\dot{Q}_B(t)$ exists prior to ice crystallization. In this case, however, the unknown heat capacity for subcooled water makes equation 3.18 difficult to validate quantitatively.

Our proposed non-isothermal kinetic theory also predicts $\bar{\tau}_I$ and $\overline{T}_C$ as functions of cooling rate, β. Solid lines in Figures 3.3 and 3.4 correspond to predictions of $\bar{\tau}_I$ and $\overline{T}_C$ using equations 3.6, 3.16, and 3.17 with $A = 9.1\times10^7$ nuclei m^{-3} s^{-1} and $B = 1.1\times10^5$ K^3. As illustrated in Figure 3.5, nucleation is a random statistical process, so that isothermal induction times follow a Poisson distribution at a given subcooling [2]. Accordingly, A and B were chosen in equation 3.17 from a range of measured isothermal induction times [2] (see Chapter 2) to best-fit the data shown in Figure 3.3, and are listed in Table 3.3. Good quantitative agreement is seen between theory and experiment in both Figures 3.3 and 3.4. Significantly, these results illustrate that measured isothermal induction times in equation 3.17 can be used to predict reliable non-isothermal crystallization temperatures.

Lines in Figure 3.6 show predicted transient gas-free volume fractions of ice within the GDL pores, $\phi(t)$, for cooling rates of 2.5, 5, 10, and 25 K/min. Lines are calculated from equation 3.15 using $\bar{\tau}_I$, $\overline{T}_C$, A, and B values from the individual experiments in Figures 3.3 and 3.4. For all cooling rates, predicted complete-crystallization times are in good agreement with measured values. Measured and predicted complete-crystallization times are: 13.3, 9.2, 8.2, and 7.0 s; 11.5, 7.9, 7.4, and 6.7 s for cooling rates of 2.5, 5, 10, and 25 K/min, respectively.

Due to the statistical nature of nucleation (see Figure 3.5), values of A and B vary significantly among repeated crystallization exotherms [2]. To examine the sensitivity of $\phi(t)$ to A and B, $\phi(t)$ was predicted for the range of A and B values previously determined [2]. The solid line in Figure 3.7 is a prediction of $\phi(t)$ and $\bar{\tau}_I$ at a cooling rate of 10 K/min using average

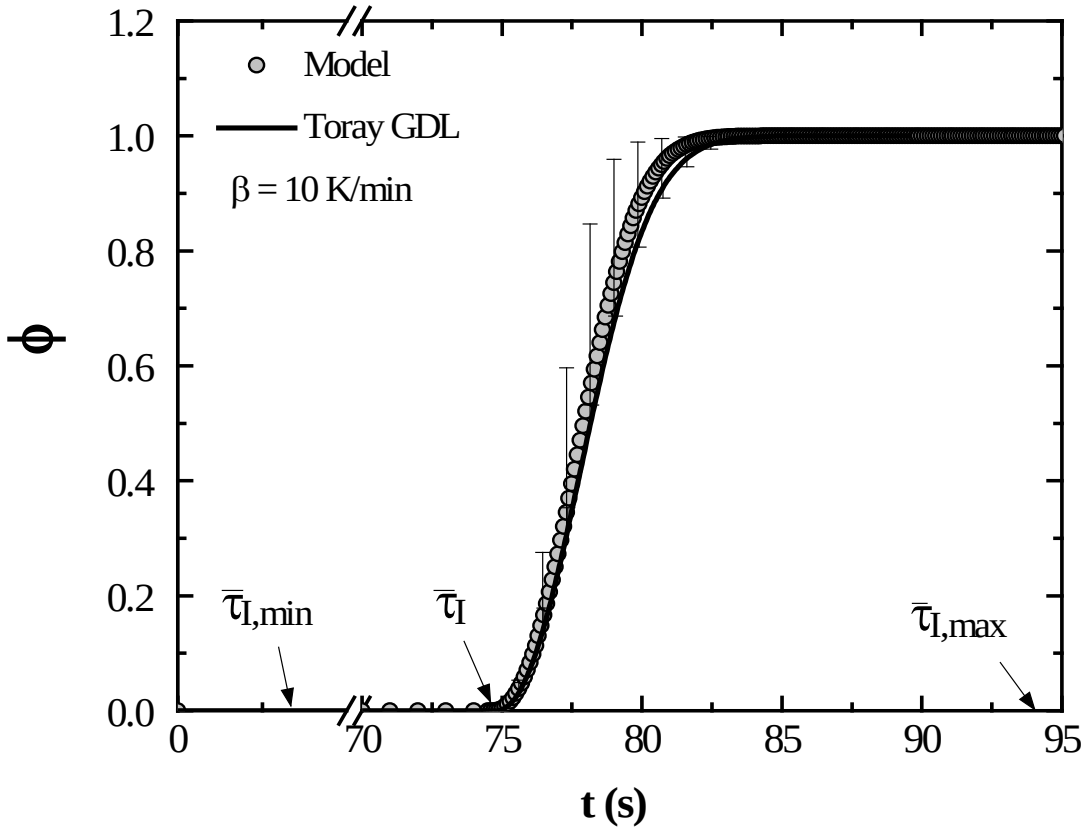

Figure 3.7. Predicted non-isothermal freezing kinetics for a water-saturated Toray GDL at cooling rate of 10 K/min. The open symbols denote measured $\phi(t)$ from Figure 3.6. The solid line represents predictions of $\phi(t)$ and $\bar{\tau}_I$ as described in Appendix 3B. Error bars denote minimum and maximum $\phi(t)$ predictions using a range previously reported of A and B values [2]. $\bar{\tau}_{I,\min}$, $\bar{\tau}_I$, and $\bar{\tau}_{I,\max}$ label predictions for the minimum, average, and maximum non-isothermal induction time, respectively.

A and B values, while open symbols represent a single measurement of $\phi(t)$ and $\bar{\tau}_I$. Error bars denote minimum and maximum $\phi(t)$ predictions using the range of previously reported A and B values (see Chapter 2) [2]. $\bar{\tau}_{I,\min}$, $\bar{\tau}_I$, and $\bar{\tau}_{I,\max}$ label, respectively, predictions for the minimum, average, and maximum non-isothermal induction times. In Figure 3.7, measured values lie within the range of theoretical predictions indicating excellent agreement. The statistical range of A and B decreases as ΔT increases, so that model predictions are more precise for larger β.

3.6.2. Pseudo-Isothermal Ice Crystallization:

The direct effect of cooling rate on freezing kinetics can be neglected when the time for crystallization is much shorter than the time required to decrease the sample temperature by subcooling, $\Delta\overline{T}_C = T_o - \overline{T}_C$. From non-dimensionalization of equation 3.7, the effect of β on $\phi(t)$ is insignificant when

$$\Omega = \left[\frac{\beta\, t_f}{\Delta\overline{T}_C}\right]\left[\frac{m_{eff,S}\hat{C}_{p,eff,S}}{m_{w,o}\hat{C}_{p,w}}\right] Ste << 1 \tag{3.19}$$

where t_f is the characteristic time for crystallization and $Ste = \hat{C}_{p,w}\,\Delta\overline{T}_C / \Delta\hat{H}_f$ is the Stefan number at the crystallization temperature. When applicable, this approximation greatly simplifies the kinetic expression, since the convolution integral in equation 3.15 solves explicitly.

For non-isothermal ice crystallization under heat-transfer-limited volume growth, t_f may be established as $L^2\eta_o^2(Ste)/[\alpha_w Ste]$, where L is the sample thickness and $\eta_o^2(Ste)$ is given by equation 3.14. This definition of t_f is conservative since the sample thickness is adopted as the characteristic length, L. Substitution of t_f into equation 3.19 gives the criterion for pseudo-isothermal ice crystallization

$$\Omega = \frac{\beta L^2}{\alpha_w \Delta\overline{T}_C}\frac{\eta_o^2(Ste)\, m_{eff,S}\hat{C}_{p,eff,S}}{m_{w,o}\hat{C}_{p,w}} << 1. \tag{3.20}$$

During pseudo-isothermal ice crystallization, equations 3.8 and 3.15 simplify considerably

$$R_i(\overline{T}_C,\phi) = k(\overline{T}_C)^{2/5}[1-\phi][-\ln(1-\phi)]^{3/5} \qquad \text{for} \quad t \geq \bar{\tau}_I, \tag{3.21}$$

where

$$k(\overline{T}_C) = \frac{64\pi}{15}\alpha_w^{3/2} g(\theta) J\left(\overline{T}_C\right)\eta_o^3\left(\overline{T}_C\right). \tag{3.22}$$

Equations 3.21 and 3.22 are readily solved to determine $\phi(t)$ for varying $\bar{\tau}_I$ and $\overline{T}_C$. Thus, for pseudo-isothermal crystallization kinetics, the effect of cooling rate appears only in the dependences of $\bar{\tau}_I$ and $\overline{T}_C$ on β (see Figures 3.3 and 3.4).

Figure 3.8 compares non-isothermal (solid lines) and pseudo-isothermal (dashed lines) model-predicted $\phi(t)$ for cooling rates of $\beta = 2.5$, 10, and 25 K/min, corresponding to $\Omega = 0.008$, 0.032, and 0.102, respectively. As Ω decreases, the pseudo-isothermal

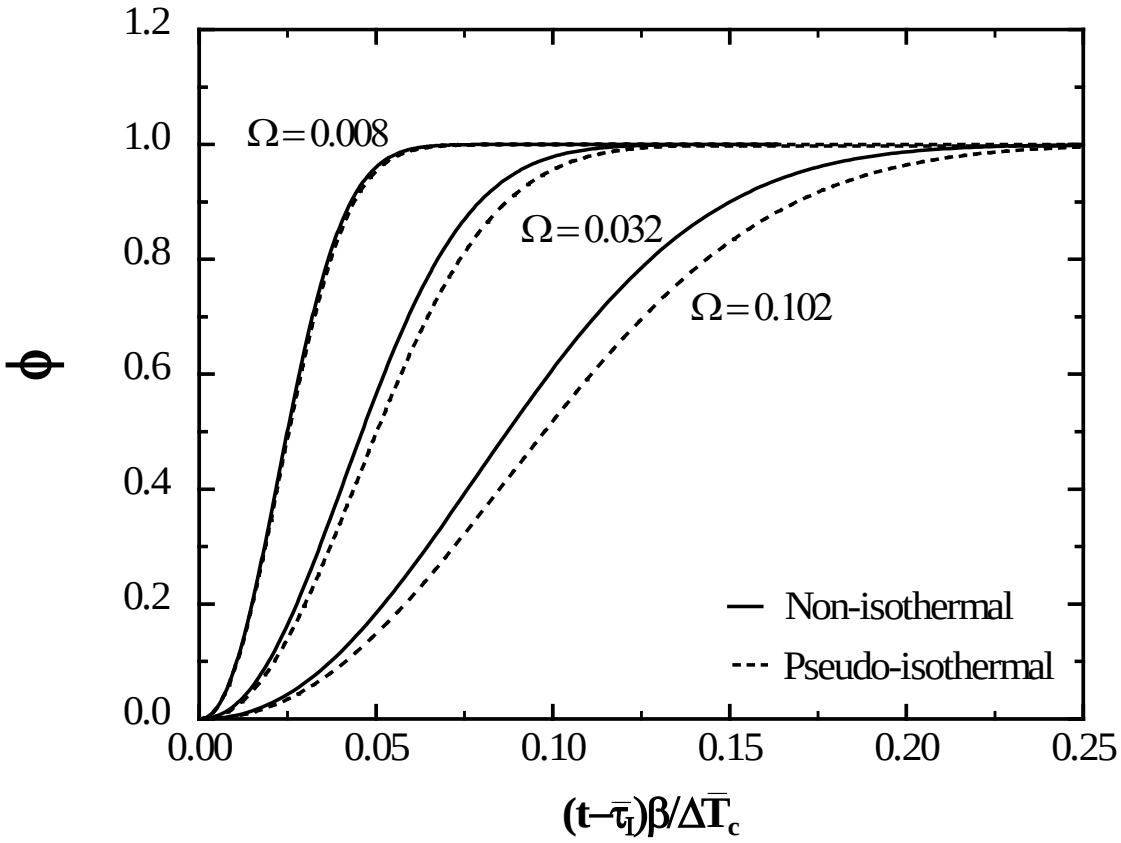

Figure 3.8. Predicted freezing kinetics for a water-saturated GDL at cooling rates of 2.5, 10, and 25 K/min, corresponding to $\Omega = 0.008$, 0.032, and 0.102 in equation 3.20, respectively. Solid lines are non-isothermal $\phi(t)$ predictions (described in Appendix 3B), whereas dashed lines are pseudo-isothermal predictions from equations 3.20 and 3.21.

approximation becomes increasingly accurate. This observation confirms that the pseudo-isothermal approximation is valid whenever $\Omega << 1$. Since equation 3.15 directly integrates, adoption of the pseudo-isothermal approximation provides a greatly simplified methodology to estimate heterogeneous crystallization kinetics. Additionally, this approximation agrees well with previous work in polymer crystallization, where non-isothermal effects are unimportant for low cooling rates [33, 34].

With the model parameters in Table 3.3, $\Omega = 0.008$, 0.011, 0.032, and 0.102 for $\beta = 2.5$, 5, 10, and 25 K/min, respectively. Accordingly, the direct effect of cooling rate on $\phi(t)$ is negligible in our DSC experiments. Thus, $\phi(t)$ is well-predicted assuming isothermal crystallization, but only when nucleation and growth rates are evaluated at the non-isothermal crystallization temperature, $\overline{T_C}$, which in turn depends on β (see Figure 3.3).

3.7. Conclusions

We determine non-isothermal ice-crystallization rates and non-isothermal induction times as a function of cooling rate in fuel-cell gas-diffusion layers (GDLs) using differential scanning calorimetry (DSC). Kinetic rates were measured by DSC heat-flow dynamics for a commercial Toray GDL at cooling rates of 2.5, 5, 10, and 25 K/min. Induction-time measurements reveal that non-isothermal induction times decrease monotonically with increasing cooling rate. Similarly, heat-flow measurements reveal that complete-crystallization times decrease with increasing cooling rate. Importantly, we find that the decrease in complete-crystallization time is primarily a result of the decrease in crystallization temperature.

Our previously developed isothermal ice-crystallization rate expression is extended to non-isothermal crystallization to predict DSC ice-freezing kinetics in a GDL as a function of cooling rate. Agreement between experiment and theory is good. Most importantly, our calculations show that during solidification, cooling rate has a negligible effect on the crystallization rate since ice-crystallization times are much faster than the time to decrease the sample temperature by the subcooling. Therefore, we find that non-isothermal ice-crystallization kinetics in the GDL are well approximated using pseudo-isothermal ice-crystallization kinetics but evaluated at the determined non-isothermal crystallization temperature.

3.8. List of Symbols

a $0.056\ K^{-1}$ in equation 3B.8

A nucleation constant (nuclei/m^3/s)

A_p pan area containing DSC platform

B induction-time constant (K^3)

J pseudo steady-state nucleation rate (nuclei/m^3/s)

k overall kinetic rate constant ($s^{-2.5}$)

k_{th} thermal conductivity (W/m/K)

L sample thickness (μm)

m mass (kg)

$\dot{Q}$ heat-flow rate (mW)

R_i ice-formation rate (ice volume/water plus ice volume/s)

Ste Stefan number

T Temperature (K)

T_o 273 K

ΔT subcooling, $T_o - T$ (K)

t time (s)

$t_{99\%}$ complete-crystallization time (s)

S saturation

U overall heat transfer coefficient

Greek Letters

α thermal diffusivity (m^2/s)

β cooling rate (K/min)

ε porosity of GDL

κ instrument-detectable volume fraction of the initial liquid

η_o thermal-growth constant

θ contact angle

ξ defined in equation 3B.1

ρ mass density (kg/m^3)

τ induction time (s)

ϕ volume fraction

ω instrument constant in equation 3.17

Ω dimensionless time in equations 3.19 and 3.20

Subscripts

B baseline

C crystallization

cf carbon fibers

eff effective

f final

F furnace

g gas

i ice

I indium

o initial

p pan

R reference

S sample

w water

3.9. Acknowledgements

This work was funded by the Assistant Secretary for Energy Efficiency and Renewable Energy, Office of Fuel Cell Technologies, of the U. S. Department of Energy under contract number DE-AC02-05CH11231. We thank Los Alamos National Laboratory for providing mercury-porosimetry-intrusion data.

3.10. References

[1] E. Cho, J.J. Jo, H.Y. Ha, S. Hong, K. Lee, T. Lim, I. Oh, Characteristics of the PEMFC repetitively brought to temperatures below 0 °C, J. Electrochem. Soc. 150 (2003) A1667-A1670.

[2] T.J. Dursch, M.A. Ciontea, C.J. Radke, A.Z. Weber, Isothermal ice-crystallization kinetics in the gas-diffusion layer of a proton-exchange-membrane fuel cell, Langmuir 28 (2012) 1222-1234.

[3] T.W. Chan, A.I. Isayev, Quiescent polymer crystallization: modeling and measurements, Polym. Eng. Sci. 34 (1994) 461-471.

[4] M. Eder, A. Wlochowicz, Kinetics of non-isothermal crystallization of polyethylene and polypropylene, Polymer 24 (1983) 1593-1595.

[5] T. Liu, Z. Mo, S. Wang, H. Zhang, Non-isothermal melt and cold crystallization kinetics of poly (aryl ether ether ketone ketone), Polym. Eng. Sci. 37 (1997) 568-575.

[6] T. Ozawa, Kinetics of non-isothermal crystallization, Polymer 12 (1970) 150-158.

[7] T.V. Chan, G.D. Shyu, A.I. Isayev, Master curve approach to polymer crystallization kinetics, Polym. Eng. Sci. 35 (1995) 733-740.

[8] C.H. Wu, G. Eder, H. Janeschitz-Kriegl, Polymer crystallization dynamics, as reflected by differential scanning calorimetry. Part 2: Numerical simulations, Coll. Polym. Sci. 271 (1993) 1116-1128.

[9] G. Lamberti, Importance of heat transfer phenomena during DSC polymer solidification, Int. J. Heat Mass Trans. 41 (2004) 23-31.

[10] M. Avrami, Kinetics of phase change I general theory, J. Chem. Phys. 7 (1939) 1103-1112.

[11] M. Avrami, Kinetics of phase change II transformation-time relations for random distribution of nuclei, J. Chem. Phys. 8 (1940) 212-224.

[12] W.A. Johnson, R.F. Mehl, Reaction kinetics in processes of nucleation and growth, AIME Trans.135 (1939) 416.

[13] A.N. Kolmogorov, Selected Works of A.N. Kolmogorv, vol. 1, Kluwer Academic Publishers, Dodrecht, 1985, pp. 530-560.

[14] C.J.G. Plummer, H.-H. Kaush, DSC non-isothermal crystallization curves in polyoxymethylene, Coll. Polym. Sci. 273 (1995) 227-232.

[15] A. Hammami, J.E. Spruiell, Quiescent non-isothermal crystallization kinetics of isotactic polypropylenes, Polym. Eng. Sci. 35 (2004) 797-804.

[16] S. Vyazovkin, J. Stone, N. Sbirrazzuoli, Hoffman-Lauritzen parameters for non-isothermal crystallization of poly(ethylene terephthlate) and poly(ethylene oxide) melts, J. Thermal Analysis Calorimetry 80 (2005) 177-180.

[17] J.T. Gostick, M.W. Fowler, M.A. Ioannidis, M.D. Pritzker, Y.M. Volfkovich, A. Sakars, Capillary pressure and hydrophilic porosity in gas diffusion layers for polymer electrolyte fuel cells, J. Power Sources 156 (2006) 375-387.

[18] E. Gmelin, St. M. Sarge, Calibration of differential scanning calorimeters, Pure Appl. Chem. 67(1995) 1789-1800.

[19] K.H. Kim, A. I. Isayev, K. Kwon, Crystallization kinetics for simulation of processing of various polyesters, J. Appl. Polym. Sci. 102 (2006) 2847-2855.

[20] W. Xu, M. Ge, P. He, Nonisothermal crystallization kinetics of polyoxymethylene/ montmorillonite nanocomposite, Journal of Applied Polymer Science 82 (2001) 2281-2289.

[21] P. Supaphol, N. Dangseeyun, P. Srimoaon, M. Nithitanakul, Nonisothermal melt-crystallization kinetics for three linear aromatic polyesters, Thermochim. Acta 406 (2003) 207-220.

[22] W.L. Sifleet, N. Dinos, J.R. Collier, Unsteady-state heat transfer in a crystallizing polymer, Polym. Eng. Sci.13 (2004) 10-16.

[23] G. Lamberti, Some issues on polymer crystallization kinetics studied by DSC non isothermal tests, Polym. Bulletin 56 (2006) 591-598.

[24] G. Lamberti, Isotactic polypropylene crystallization: analysis and modeling, Euro. Polym. J. 47 (2011) 1097-1112.

[25] Z. Ding, J.E. Spruiell, An experimental method for studying nonisothermal crystallization of polymers at very high cooling rates, J. Polym. Sci. B: Polym. Phys. 34 (1998) 2783-2804.

[26] G.W.H. Hohne, W.F. Hemminger, H.J. Flammersheim, Differential Scanning Calorimetry, second ed., Springer, Heidelberg, 2003, pp. 31-63.

[27] D.R. Uhlmann, B. Chalmers, The energetics of nucleation, Ind. Eng. Chem. 57 (1965) 19-31.

[28] H.S. Carslaw, J.C. Jaeger, Conduction of Heat in Solids, second edition, Oxford University Press, Oxford, 1959, chapter 11.

[29] L. I. Rubinstein, The Stefan Problem, American Mathematical Society, Rhode Island, 1971, chapter 1.

[30] D. Kashchiev, D. Verdoes, G.M. van Rosmalen, Induction time and metastability limit in new phase formation, J. Crystal Growth 110 (1991) 373-380.

[31] A.V. Bitsadze, Integral Equations of First Kind, Volume 7, World Scientific Publishing, New Jersey, 1995, chapter 7.

[32] C. Lim, C.Y. Wang, Effects of hydrophobic polymer content in GDL on power performance of a PEM fuel cell, Electrochim. Acta 49 (2004) 4149-4156.

[33] N. Nakamura, T. Watanabe, K. Katayama, T. Amano, Some aspects of nonisothermal crystallization of polymers. I. Relationship between crystallization temperature, crystallinity, and cooling conditions, J. Appl. Polym. Sci. 16 (1972) 1077-1091.

[34] A. Ziabicki, Kinetics of polymer crystallization and molecular orientation in the course of fiber spinning, Appl. Polym. Sym. 6 (1967) 1-18.

Appendix 3A. Overall Heat Transfer Coefficient

Following Wu et al. [8], the overall heat transfer coefficient, *U*, is obtained from sample temperature versus time in a heating cycle of an indium sample. When sample spatial temperature gradients are negligible, an overall energy balance applies for estimating the indium sample temperature, T_I, as a function of time [8]

$$\left(m_I \hat{C}_{p,I} + m_p \hat{C}_{p,p}\right)\frac{dT_I}{dt} = UA_p\left(T_F - T_I\right) \tag{3A.1}$$

with the initial condition $T_I(0) = T_{Io}$, and where A_p is area underneath the pan, *m* is mass, $\hat{C}_p$ is the specific heat capacity, and the subscripts *I* and *p* denote indium and the aluminum pan, respectively. The integrated form of equation 3A.1 for $T_I(t)$ is fit to the measured transient indium temperature from the heating cycle to provide the product UA_p.

Figure 3A.1 shows a plot of indium sample temperature versus time for a heating rate of 20 K/min. Masses of indium and the aluminum pan are 5.6 and 27.6 mg, respectively. Solid lines correspond to $T_I(t)$ from equation 3A.1 at three values of UA_p, with $\hat{C}_{p,I} = 233$ J kg^{-1} K^{-1} and $\hat{C}_{p,p} = 710$ J kg^{-1} K^{-1}. The best-fit value of UA_p is 0.035 W/K, which corresponds closely to the previously reported values of 0.032 W/K [10], 0.016 W/K [8], and 0.0041 W/K [3].

Appendix 3B. Numerical Solution

Solution to the transient model for the DSC described in Section 3.4 consists of two steps: calculation of the average non-isothermal induction time, $\bar{\tau}_I$, followed by solving the non-isothermal ice-crystallization rate equation along with the overall energy balances. Each step is amplified below.

3B.1. Non-isothermal Induction Time, $t < \bar{\tau}_I$:

We define a new dimensionless variable ξ as

$$\xi = \int_0^t \frac{d\eta}{\bar{\tau}_i(T_S(\eta))} \tag{3B.1}$$

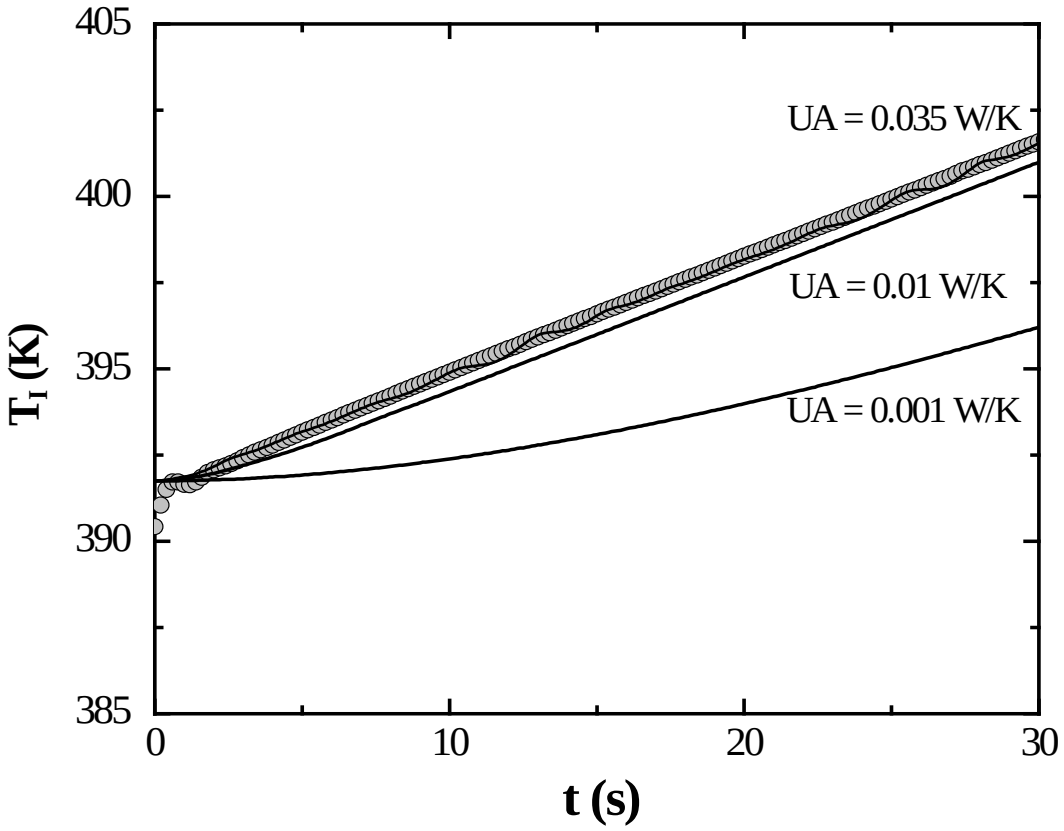

Figure 3A.1. Indium sample temperature versus time at a cooling rate of 20 K/min (open symbols). Solid lines correspond to $T_I(t)$ calculated from equation 3A.1 at three values of UA_p.

where following equation 3.16, $\xi = 1$ when $t = \bar{\tau}_I$. Equation 3B.1 expressed in differential form gives

$$\frac{d\xi}{dt} = \frac{1}{\bar{\tau}_i\left(T_S(t)\right)} \tag{3B.2}$$

with $\xi(0) = 0$. Equations 3B.2 and 3.17 provide an initial-value ordinary differential equation for ξ that is solved along with equation 3.6 to establish the number-average non-isothermal induction time, $\bar{\tau}_I$. Once $\bar{\tau}_I$ is established, equations 3.4 through 3.6 are solved for $0 \le t < \bar{\tau}_I$ to determine T_S and $\dot{Q}$ as a function of time for various cooling rates, subject to the initial conditions $T_R(0) = T_{Ro}$ and $T_S(0) = T_{So}$.

3B.2. Non-isothermal Ice-crystallization Rate, $t \ge \bar{\tau}_I$:

At $t = \bar{\tau}_I$, crystallization begins. Therefore, for $t \ge \bar{\tau}_I$ the sample energy balance in equation 3.7 includes the enthalpic source term and the crystallization rate from equation 3.8

$$m_{eff}\hat{C}_{p,eff}\frac{dT_S}{dt} = UA\left(T_F - T_S\right) + \frac{m_{w,o}\rho_i}{\rho_w}\Delta\hat{H}_f\frac{d\phi}{dt}, \tag{3B.3}$$

where

$$\phi(t) = 1 - \exp\left(-\frac{32\pi}{3}\alpha_w^{3/2}g(\theta)\int_{\tau_I}^{t} J\left(T_S(t')\right)\eta_o^3\left(T_S(t-t')\right)(t-t')^{3/2}\,dt'\right), \tag{3B.4}$$

and

$$m_{eff}\hat{C}_{p,eff} = m_{cf}\hat{C}_{p,cf} + m_{w,o}\hat{C}_{p,w} + m_p\hat{C}_{p,p}. \tag{3B.5}$$

Initial conditions are

$$T_S(\tau_I) = \overline{T_C} \text{ and } \phi(\bar{\tau}_I) = 0. \tag{3B.6}$$

To evaluate $T_S(t)$ in equation 3B.3, the Volterra integral of the first-kind [31] appearing in equation 3B.4 is approximated using the trapezoidal rule. For all $t \ge \tau_I$, the integral results in the following recurrence relation

$$\int_{\tau_I}^{t} J\left(T_S(t')\right)\eta_o^3\left(T_S(t-t')\right)(t-t')^{3/2}\,dt' = \frac{1}{2}J\left(T_s(\tau_I)\right)\eta_o^3\left(T_S(\Delta t)\right)\Delta t^{3/2} + \sum_{j=\tau_I}^{k-1} J\left(T_S(j\Delta t)\right)\eta_o^3\left(T_S\left[\left((k-j)\Delta t\right)\right]\right)\left[(k-j)\Delta t\right]^{3/2}, \tag{3B.7}$$

where the first term on the right represents $k = 1$ and the second term is applies for $k > 1$ to the total number of time steps.

Equations 3.12 and 3.14 specify J and η_o as functions of T_S, respectively. To minimize computation time, we replace the implicit equation for η_o in equation 3.14 by the following simplified expression

$$\eta_o(\Delta T) = \frac{a\Delta T}{1 + a\Delta T} \tag{3B.8}$$

where $a = 0.056\,\mathrm{K}^{-1}$. To obtain the constant a, equation 3B.8 was best fit to η_o versus $\Delta T = T_o - T_S$. Substitution of equations 3B.7 and 3B.8 into equation 3B.4 provides an expression for ϕ_k that contains only the one unknown dependent variable, $T_S(k\Delta t)$. To solve for $T_S(k\Delta t)$, equation 3B.3 is discretized to give

$$m_{eff}\hat{C}_{p,eff}\left[\frac{T_{S,k} - T_{S,k-1}}{\Delta t}\right] = UA\left(T_{F,k-1} - T_{S,k-1}\right) + \frac{m_{w,o}\rho_i}{\rho_w}\Delta\hat{H}_f\left[\frac{\phi_k - \phi_{k-1}}{\Delta t}\right] \tag{3B.9}$$

where $T_{S,k} = T_S(k\Delta t)$ and $T_{S,k-1} = T_S\left((k-1)\Delta t\right)$. Substitution of the expressions for ϕ_k and ϕ_{k-1} into equation 3B.9 results in an implicit equation for $T_{S,k}$, that is solved using the Regula-Falsi root-seeking algorithm (fzero in Matlab R2010a).

Appendix 3C. Baseline Heat-Flow Rate, $\dot{Q}_B(t)$

A simple analytical expression for $\dot{Q}_B(t)$ (valid between points C and D in Figure 3.1) is found by solving equations 3.3, 3.5, and 3.6, followed by substitution into equation 3.4

$$\begin{aligned}\dot{Q}_B(t) = &\left[UA_p\left(T_S(t_{99\%}) - T_F(t_{99\%})\right) - \beta\left(m_{eff,S}\hat{C}_{p,eff,S}\right)\right]\exp\left(-\frac{UA_p}{m_{eff,S}\hat{C}_{p,eff,S}}t\right) - \\ &\left[UA_p\left(T_R(t_{99\%}) - T_F(t_{99\%})\right) - \beta\left(m_p\hat{C}_{p,p}\right)\right]\exp\left(-\frac{UA_p}{m_p\hat{C}_{p,p}}t\right) + \beta\left(m_{eff,S}\hat{C}_{p,eff,S} - m_p\hat{C}_{p,p}\right)\end{aligned} \tag{3C.1}$$

with initial conditions $T_S(0) = T_S(t_{99\%})$ and $T_R(0) = T_R(t_{99\%})$, and where

$$m_{eff,s}\hat{C}_{p,eff,s} = m_{cf}\hat{C}_{p,cf} + m_p\hat{C}_{p,p} + m_{w,o}\hat{C}_{p,i}\rho_i/\rho_w. \tag{3C.2}$$

Chapter 4

Ice-Crystallization Kinetics in the Catalyst Layer of a Proton-Exchange-Membrane Fuel Cell

T.J. Dursch, G.J. Trigub, R. Lujan, J.F. Liu, R. Mukundan, C.J. Radke, A.Z. Weber, Ice-crystallization kinetics in the catalyst layer of a proton-exchange-membrane fuel cell, J. Electrochem. Soc. 161 (*2014*) *F199-F207.*

4.1. Abstract

Nucleation and growth of ice in the catalyst layer of a proton-exchange-membrane fuel cell (PEMFC) are investigated using isothermal differential scanning calorimetry and isothermal galvanostatic cold-starts. Isothermal ice-crystallization rates and ice-nucleation rates are obtained from heat-flow and induction-time measurements at temperatures between 240 and 273 K for four commercial carbon-support materials with various ionomer fractions and platinum loadings. Measured induction times follow expected trends from classical nucleation theory and reveal that the carbon-support material and ionomer fraction strongly impact the onset of ice crystallization. Conversely, dispersed platinum particles play little role in ice crystallization. Following our previous approach, a nonlinear ice-crystallization rate expression is obtained from Johnson-Mehl-Avrami-Kolmogorov (JMAK) theory. A validated rate expression is now available for predicting ice crystallization within water-saturated catalyst layers.

Using a simplified PEMFC isothermal cold-start continuum model, we compare cell-failure time predicted using the newly obtained rate expression to that predicted using a traditional thermodynamic-based approach. From this comparison, we identify conditions under which including ice-crystallization kinetics is critical and elucidate the impact of freezing kinetics on low-temperature PEMFC operation. The numerical model illustrates that cell-failure time increases with increasing temperature due to a longer required time for ice nucleation. Hence, ice-crystallization kinetics is critical when induction times are long (i.e., in the “nucleation-limited" regime for $T > 263$ K). Cell-failure times predicted using ice-freezing kinetics are in good agreement with the isothermal cold-starts, which also exhibit long and distributed cell-failure times for $T > 263$ K. These findings demonstrate a significant departure from cell-failure times predicted using the thermodynamic-based approach.

4.2. Introduction

Proton-exchange-membrane fuel cells (PEMFCs) show promise in automotive applications because of their high efficiency, high power density, and potentially low emissions. To be successful in automotive applications, PEMFCs must permit rapid startup with minimal energy from sub-freezing temperatures, known as cold-start. In a PEMFC, reduction of oxygen to water occurs in the cathode catalyst layer (cCL). Under subfreezing conditions, water solidifies and hinders access of gaseous oxygen to the catalytic sites in the cCL, severely inhibiting cell performance and potentially causing cell failure [1-3]. Elucidation of the mechanisms and kinetics of ice formation within the cCL is, therefore, critical to successful cell startup and high performance at low temperatures.

Because of degradation and cell failure under subfreezing conditions, much attention has been given to understanding cold-start fundamentals. To date, experiments predominately focus on characterizing overall low-temperature cell performance [1-7]. In recent years, however, *in-situ* visualization and detection of ice formation within PEMFC porous media has progressed [7-14]. Visualization methods include neutron radiography [8,9], environmental scanning electron microscopy [10], visible imaging[11-13], and latent-heat detection with infrared thermography [11,12]. In all cases, generation of by-product water was observed in the subcooled state, particularly between –2 and –20 °C. Although the generated liquid water did not freeze instantaneously, crystallization kinetics and its dependence on subcooling were not investigated [7-13].

Several PEMFC numerical cold-start models have also been recently developed [14-19]. Currently, however, no models include ice-crystallization kinetics, and consequently, do not account for subcooled liquid [14-19]. Commonly, models assume that product water vapor instantaneously solidifies when the vapor partial pressure exceeds the saturation value [14-16]. As a result, they do not account for liquid water within the PEMFC. More recently, Jiao et al. [17] and Balliet et al. [18,19] extended cold-start models to include vapor, liquid, and solid phases of water within the PEMFC. The freezing point of ice within the GDL, cCL, and PEM is based on a characteristic pore size using the Gibbs-Thomson equation. Furthermore, the ice-formation rate, R_I, is assumed linear with liquid-water saturation [18]

$$R_I \approx k_f S_L \tag{4.1}$$

where k_f is the freezing rate constant (e.g., see equation 14 in Balliet et al. [18]). Although the models include liquid water [17-19], they currently invoke thermodynamic-based freezing and circumvent ice-crystallization kinetics.

In this work, we measure isothermal ice-crystallization kinetics within PEMFC catalyst layers. Experimental ice-nucleation rates and ice-crystallization kinetics are obtained as functions of subcooling from isothermal differential-scanning-calorimetry (DSC) heat-flow measurements in water-saturated cCLs. Following our previous approach [20,21], we determine a rate expression for ice crystallization within cCLs. To validate ice-crystallization kinetics within PEMFCs, we further measure and predict cell-failure time during isothermal galvanostatic cold-start. Using a simplified PEMFC isothermal cold-start continuum model, we compare cell-failure time predicted using the newly obtained rate expression to that predicted using a traditional thermodynamic-based approach (i.e., equation 4.1). From this comparison, we identify conditions under which including ice-crystallization kinetics is critical and elucidate the impact of freezing kinetics on low-temperature PEMFC operation.

4.3. Materials and Methods

4.3.1. Catalyst Preparation:

Catalyst inks were prepared following Huang et al. [22] Inks were made by mixing 20-wt % Pt on Vulcan XC72 carbon black (Pt/C) (Sigma Aldrich, St. Louis, MO, Cat. No.: 738549-1G) with a 5-wt % Nafion solution (Sigma Aldrich, Cat. No.: 70160-25ML) in a 5:2 mass ratio (carbon:Nafion). After stirring for 15 min, 1-M tetrabutylammonium hydroxide (TBAOH) (Sigma Aldrich, Cat. No.: 86854-100ML) and glycerol (Sigma Aldrich, Cat. No.: G5516-100ML) were added in a mass ratio of 1:20:20 (glycerol:TBAOH:Nafion). The resulting solution

was stirred overnight. Following the same procedure, catalyst inks were prepared for three other carbon supports (containing no Pt): Black Pearls BP120, BP460, and BP800 (Cabot Corporation, Boston, MA). Additionally, catalyst inks were made for Vulcan XC72 without Pt and with varying carbon:Nafion mass ratios (5:1, 5:4, and 5:8) for BP800 and Vulcan XC72. Unless otherwise stated, the carbon:Nafion mass ratio is 5:2.

In all cases, catalyst inks (approximately 6 μL) were pipetted directly into 20-μL aluminum DSC pans (PerkinElmer Inc., Waltham, MA) and dried at 298 K under vacuum (4.7 kPa) to avoid cracking caused by rapid solvent evaporation. Dried samples were then saturated with Ultrapure Milli-Q (Millipore, Billerica, MA) distilled/deionized water in a home-built vacuum chamber for 1 h at 4.7 kPa. Following evacuation, excess surface water was removed by lightly blotting with Fisherbrand weighing paper (Fisher Scientific, Pittsburgh, PA). Water content was determined gravimetrically; measured values were consistent with integrated peak areas generated from DSC. Water loss by evaporation during DSC experiments was negligible. All catalyst water saturations are calculated from measured water contents to be between 78 and 94%, corresponding to typical porosities of 0.5 and 0.6, respectively [5,18,19,23].

4.3.2. Differential Scanning Calorimetry:

A PerkinElmer 6000 DSC (PerkinElmer Inc., Waltham, MA) with a liquid-nitrogen chiller measured heat-flow rate from the sample over time. The DSC was calibrated as described previously [20]. Nitrogen served as the purge gas at a flow rate of 20 mL/min. Isothermal crystallization was carried out from 240 to 273 K. Water-saturated catalyst samples were placed into the DSC at 300 K and cooled to the desired temperature at 105 K/min. A rapid cooling rate was chosen to reach the isothermal freezing temperature well before the onset of crystallization. Samples were then held at the subcooled temperature until crystallization was complete. Experiments were performed at various subcoolings, $\Delta T = T_o - T$, defined as the magnitude of the difference in the temperature of freezing and 273 K.

4.3.3. Isothermal Cold-Start:

Membrane electrode assemblies (MEAs) were provided by Ion Power (Ion Power, Inc., New Castle, DE). MEAs consisted of a Dupont™ Nafion® XL membrane, a TEC10EA40E cathode, and a TEC10V20E anode with 0.15 and 0.07 mg/cm^2 Pt loading, respectively. Ion Power purchased the cathode and anode catalysts from Tanaka Kikinzoku Kogyo K.K. (Tanaka Kikinzoku Kogyo K.K., Tokyo, Japan) and mixed them with a Nafion® solution to form an ink that was then painted on a web prior to transfer to the membrane. MEAs were assembled in single 50-cm^2 quad-serpentine fuel-cell hardware with cooling loops machined into both end plates. Cells were tested on a Fuel Cell Technologies testing stand (Fuel Cell Technologies, Inc., Albuquerque, NM) and cooled using a Neslab ULT-80 bath circulator.

Prior to each isothermal cold-start experiment, cells were conditioned at a current density of 1000 mA/cm^2 at 353 K and 100 % relative humidity. Following conditioning, cathode and anode flow channels were purged with 1000 mL/min of nitrogen gas for 30 seconds to prevent water from forming ice and clogging the flow fields. Cells were then cooled down to the desired isothermal freezing temperature and equilibrated at that temperature for 30 min. Isothermal cold-start experiments were carried out with 500 sccm of dry hydrogen and air. Following an initial current ramp of 0.4 mA/cm^2-s, current of 20 mA/cm^2 was applied until the cell voltage decayed to 0 mV. The cells were then heated to 353 K for characterization and cycling was repeated.

4.4. Experimental Results

4.4.1. Ice-Crystallization Kinetics:

Figure 4.1 shows a typical exotherm of heat flow and sample temperature versus time for a water-saturated Vulcan XC72 catalyst. The sample was cooled at 105 K/min to 257 K (i.e., $\Delta T = 16$ K), where isothermal crystallization commenced (point A in Figure 4.1). Heat flow due to liberation of the enthalpy of crystallization from point A is evident until a minimum is observed at point B, after which crystallization slows significantly until complete crystallization at point C. To obtain the gas-free ice volume fraction within the catalyst pores as a function of time, $\phi(t)$, crystallization exotherms were integrated from point A to point C, according to [20,21]

$$\phi(t) = \frac{\int_0^t \dot{Q}(t)\,dt}{\int_0^\infty \dot{Q}(t)\,dt} \tag{4.2}$$

where $\dot{Q}(t)$ is heat-flow rate from the DSC. Crystallization is preceded by an induction time, τ_i, defined as the time elapsed between the sample temperature becoming isothermal and the onset of the crystallization peak (point A), about 225 s in Figure 4.1.

Figure 4.2 displays number-average induction time, $\bar{\tau}_i$, as a function of subcooling, ΔT, for five water-saturated catalysts: 20 wt % Pt on Vulcan XC72 (triangles), Vulcan XC72 without Pt (squares), BP120 (inverted triangles), BP460 (diamonds), and BP800 (circles). Symbols denote average-τ_i measurements for a minimum of 25 experiments. Typical error bars for BP120 are discussed below. Solid lines are drawn according to classical nucleation theory (CNT), as discussed later. Several features are salient. In all cases, $\bar{\tau}_i$ decreases with increasing ΔT, as expected [20,21,24]. $\bar{\tau}_i$ measurements for Vulcan XC72 are similar to those for BP120 and BP460/800, but are shifted to larger ΔT by about 3 and 8 K, compared to those for BP120 and BP460/800, respectively. This result indicates that the specific carbon-support material impacts the onset of ice crystallization. Similar $\bar{\tau}_i$ measurements for Vulcan XC72 with and without added platinum (compare triangles and squares) at nearly all ΔT reveals that dispersed platinum particles, with diameters ranging from 3-5 nm [10], play little role in ice crystallization at typical loadings.

Example error bars in Figure 4.2 indicate the maximum range of observed τ_i. For all catalysts, τ_i was measured repeatedly to investigate the statistical nature of ice crystallization and to obtain pseudo-steady-state ice-nucleation rates, as discussed below. Representative results for BP120 are shown in Figure 4.3. Figure 4.3 displays 25 induction times measured at subcoolings of (a) 14.75 K and (b) 20 K for BP120, where the horizontal dashed line indicates the number-average induction time, $\bar{\tau}_i$. For both subcoolings, ΔT, τ_i generally lies below the mean with intermittent excursions to long times. Increased subcoolings result in narrower τ_i-distributions. Due to the stochastic nature of ice nucleation (see Chapter 2), τ_i measurements follow a Poisson distribution, as discussed elsewhere [20,21,24].

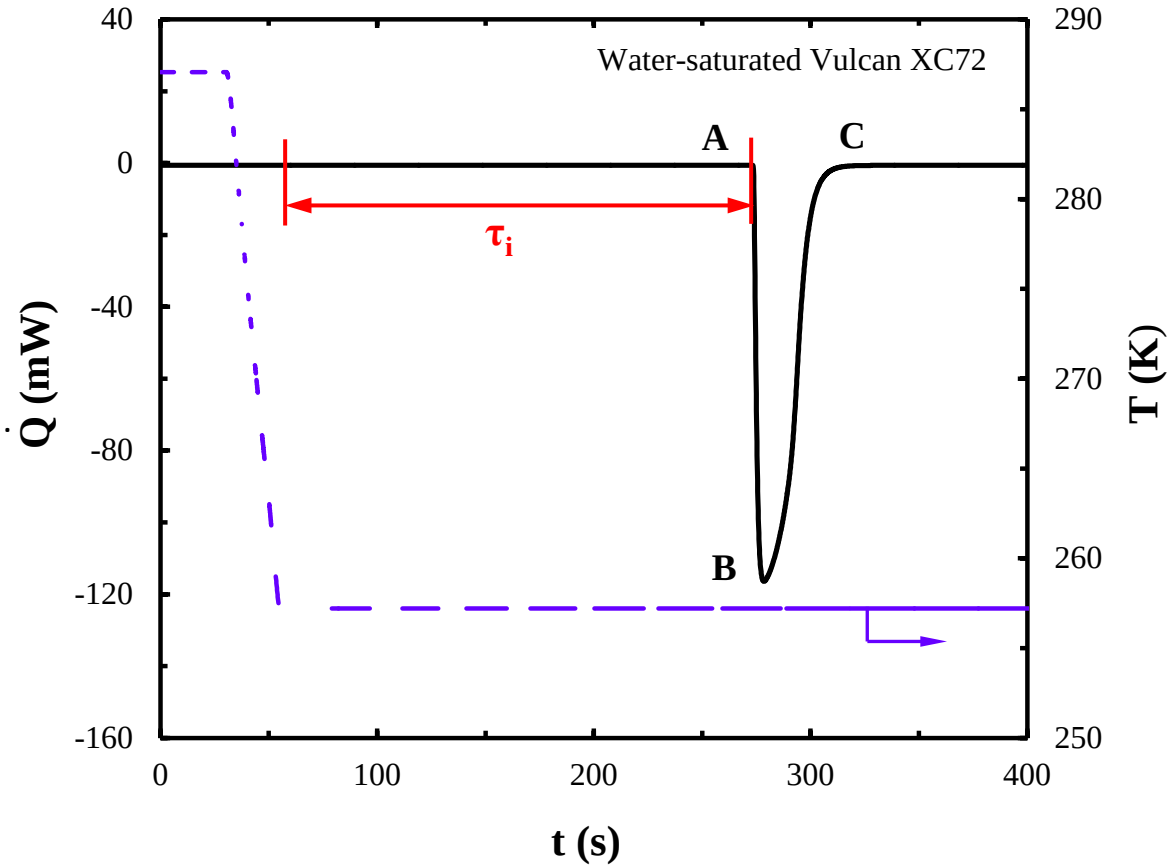

Figure 4.1. Typical isothermal DSC cooling exotherm of a water-saturated Vulcan XC72 catalyst at 257 K. The dashed line corresponds to the sample temperature, T, whereas the solid line represents heat-flow rate, $\dot{Q}$. The symbol τ_i labels the induction time. A─C label the onset, extremum, and completion of water freezing, respectively.

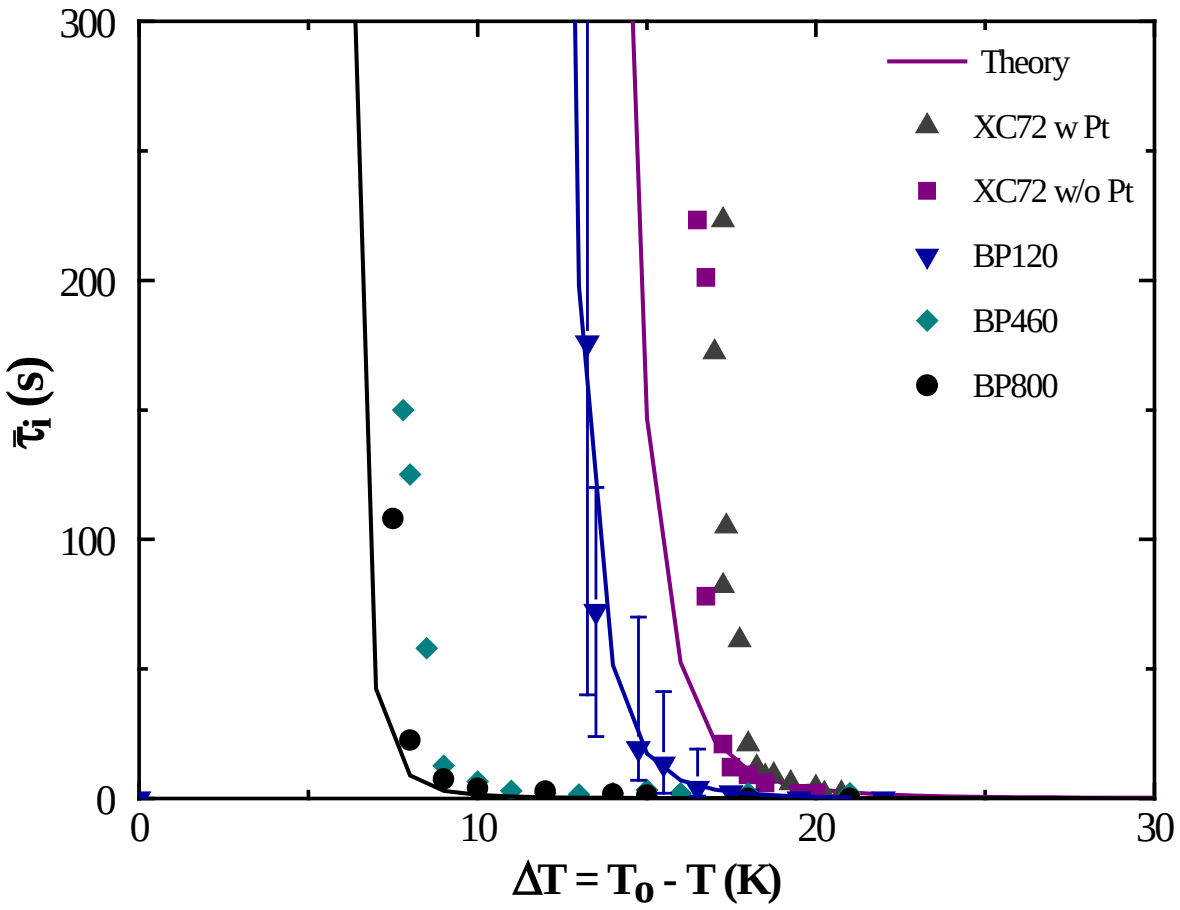

Figure 4.2. Isothermal number-average induction time, $\bar{\tau}_i$, as a function of subcooling, ΔT, for five PEMFC catalysts. Symbols correspond to 20 wt % Pt on Vulcan XC72 (triangles), Vulcan XC72 without Pt (squares), BP120 (inverted triangles), BP460 (diamonds), and BP800 (circles). Example error bars indicate the maximum range of observed τ_i. Solid lines are predictions of $\tau_i(\Delta T)$ from classical nucleation theory using equations 4.5 and 4.6.

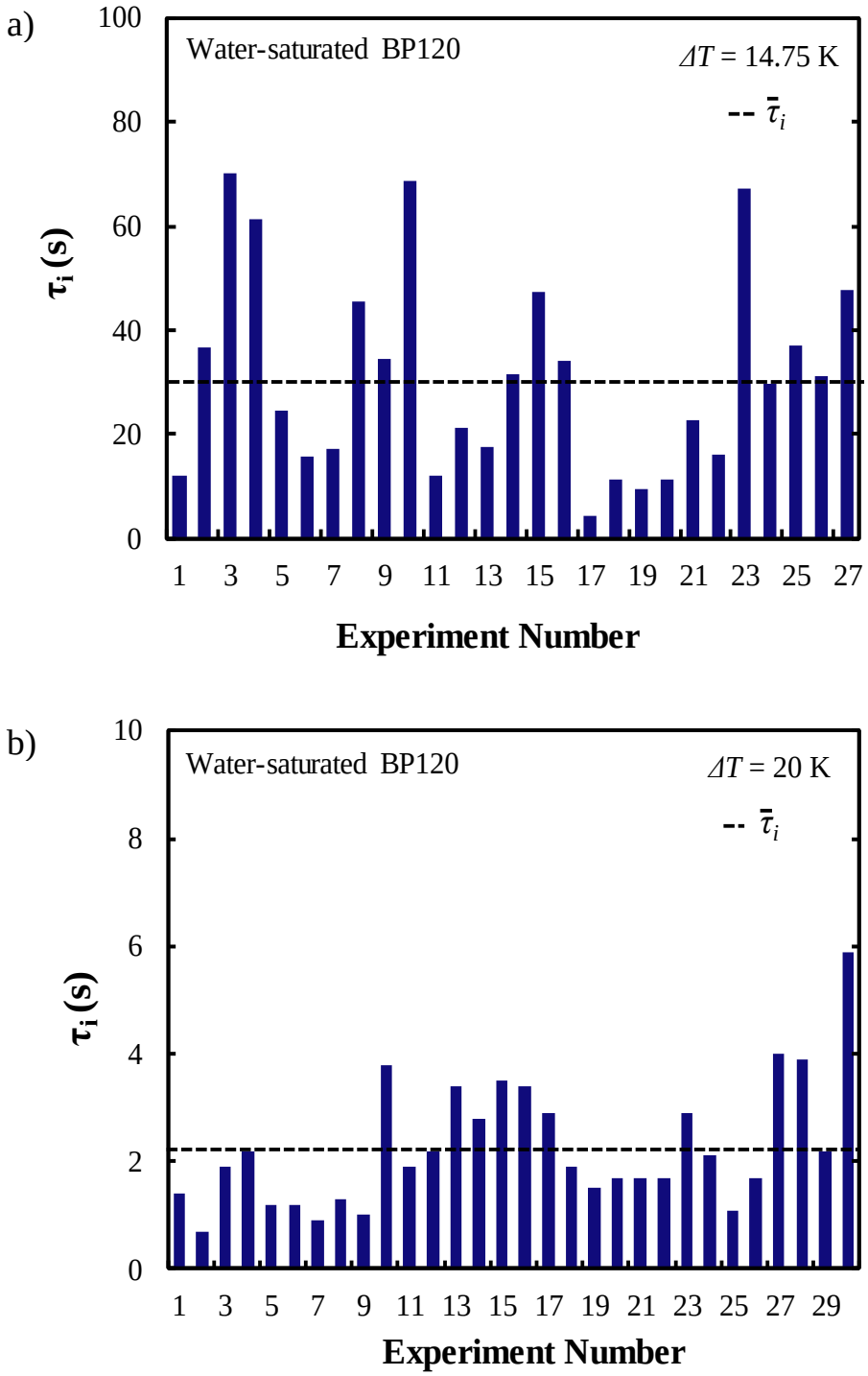

Figure 4.3. 25 induction-time measurements at a subcooling of (a) 14.75 K and (b) 20 K for BP120. Horizontal dashed lines indicate the number-average induction time, $\bar{\tau}_i$.

Figure 4.4 shows ice-crystallization kinetics, $\phi(t)$ versus t, calculated from equation 4.2 for the five water-saturated catalysts in Figure 4.2 (for specific samples with $\tau_i \approx \bar{\tau}_i$). Symbols denote 20-wt % Pt on Vulcan XC72 (triangles), Vulcan XC72 without Pt (squares), BP120 (inverted triangles), BP460 (diamonds), and BP800 (circles). Filled symbols correspond to a subcooling of 17.5 K, whereas open symbols (circles) correspond to a subcooling of 11 K. Solid and dashed lines are predictions of $\phi(t)$ from Johnson-Mehl-Avrami-Kolmogorov (JMAK) theory at $\Delta T = 17.5$ K and 11 K, respectively, as discussed below. At each subcooling, τ_i was subtracted from the total time so that all curves are compared on a single time scale. Complete ice-crystallization times (taken when $\phi(t) = 0.99$) are 13.3, 13.7, 22.0, and 24.1 s for BP460, BP800, BP120, and Vulcan XC72 at 17.5 K, respectively. Similar to Figure 4.2, Figure 4.4 illustrates that the carbon-support material appreciably impacts ice-freezing kinetics. Likewise, nearly identical $\phi(t)$ for Vulcan XC72 with and without platinum demonstrates that dispersed platinum does not significantly affect the kinetics of ice-crystallization. As ΔT decreases from 17.5 to 11 K for BP800, complete-ice-crystallization times increase from 13.3 to 27.7 s. This result reiterates that subcooling, ΔT, is the driving force for ice crystallization [20].

4.4.2. Isothermal Cold-Start:

Figure 4.5 shows a typical evolution of MEA cell voltage (squares) during isothermal cold-start from a subcooling of 6 K at a current density (circles) of 20 mA/cm^2. Initially, cell voltage decreases from 1.0 to 0.8 V during the current ramp of 0.4 mA/cm^2-s. Following a constant current density of 20 mA/cm^2, cell voltage remains constant until failure (i.e., when cell voltage rapidly decreases to 0 mV) as a result of ice formation within the cathode [1-19,35]. We define the cell-failure time, t_{fail}, as the time elapsed between the onset of constant cell voltage and 0 mV. We do not include the 30-min stabilization period when determining measured t_{fail}. To demonstrate applicability of ice-freezing kinetics to PEMFC cold-start, isothermal t_{fail} was measured as a function of ΔT.

Figure 4.6 plots isothermal t_{fail} versus ΔT at a current density of 20 mA/cm^2. Solid and dashed lines are discussed below in Section 4.6 and Appendix 4A. As ΔT increases, t_{fail} decreases substantially due to a shorter time required for ice nucleation (i.e., decreased $\bar{\tau}_i(\Delta T)$ in Figure 4.2). For example, t_{fail} decreases from 15.5 and 33 h to 0.19 and 0.2 h for an increase in ΔT from 5 to 10 K, respectively. The variance (not shown) between repeated t_{fail} measurements also decreases significantly with increasing ΔT, suggesting that stochastic nucleation events are critical at low subcoolings. This finding is consistent with narrowing τ_i-distributions for increased ΔT (compare Figure 4.2a and Figure 4.2b). Since a single induction time corresponds to a given cell-failure time, t_{fail} values are similarly distributed. Our measured isothermal cell-failure times are similar to those obtained by Oberholzer et al. [8], who observed a Poisson distribution of MEA-cell-failure times during isothermal galvanostatic cold-start from 258 to 268 K using neutron imaging.

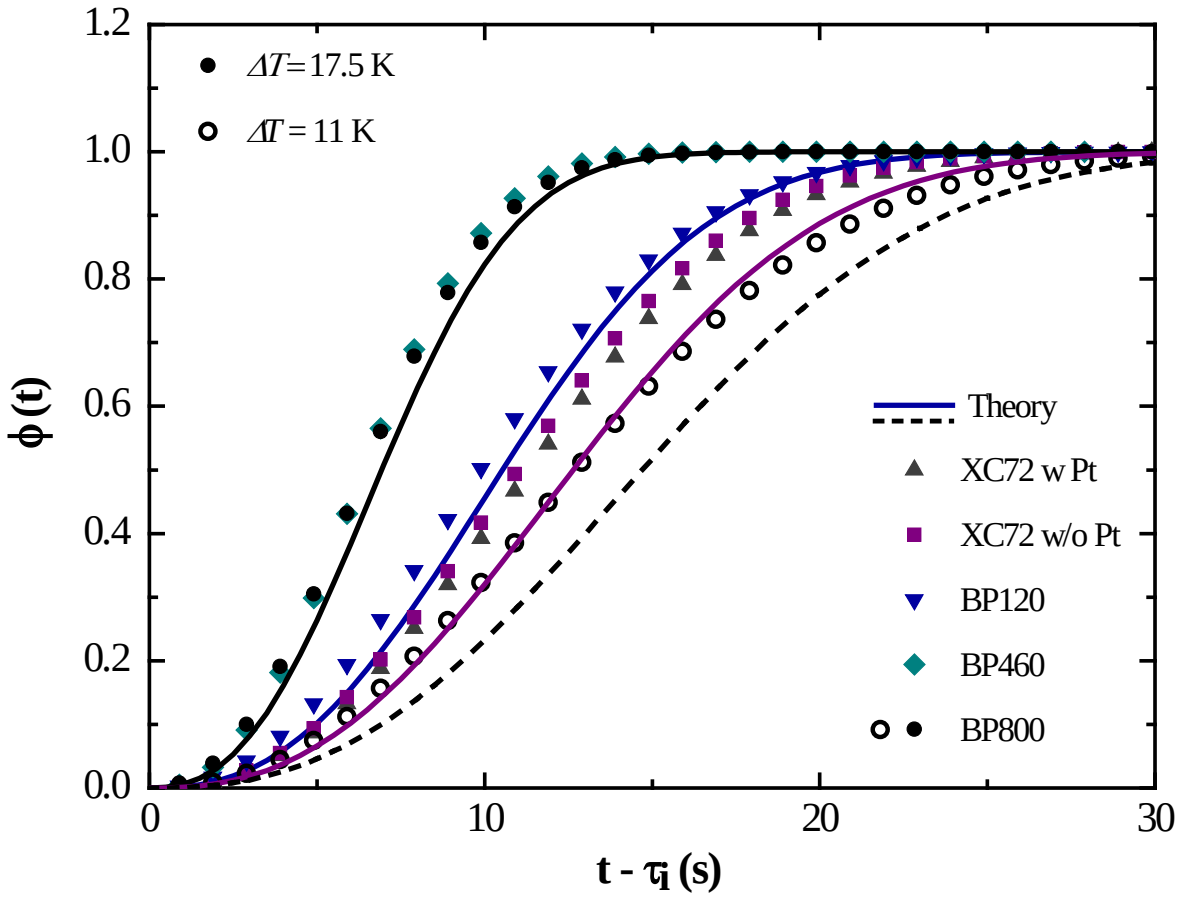

Figure 4.4. Isothermal freezing kinetics for five PEMFC catalysts. Symbols denote 20 wt % Pt on Vulcan XC72 (triangles), Vulcan XC72 without Pt (squares), BP120 (inverted triangles), BP460 (diamonds), and BP800 (circles). Filled symbols correspond to a subcooling of 17.5 K, whereas open symbols (circles) correspond to a subcooling of 11 K. Solid and dashed lines are predictions of $\phi(t)$ using equations 4.3 and 4.4, at subcoolings of 17.5 and 11 K, respectively.

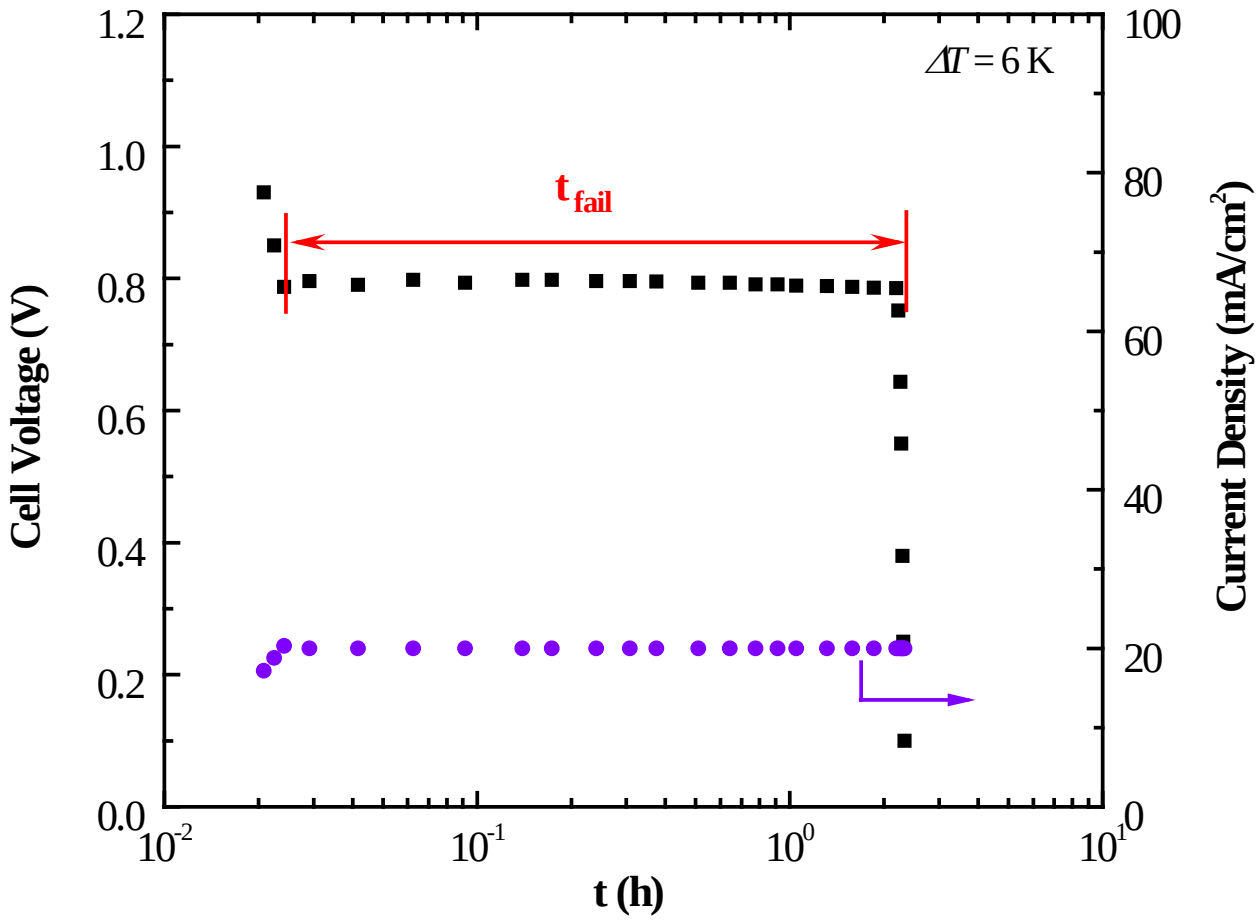

Figure 4.5. Typical evolution of MEA cell voltage during isothermal galvanostatic cold-start from 267 K. Squares denote cell voltage, whereas circles represent current density. The symbol t_{fail} labels the cell-failure time.

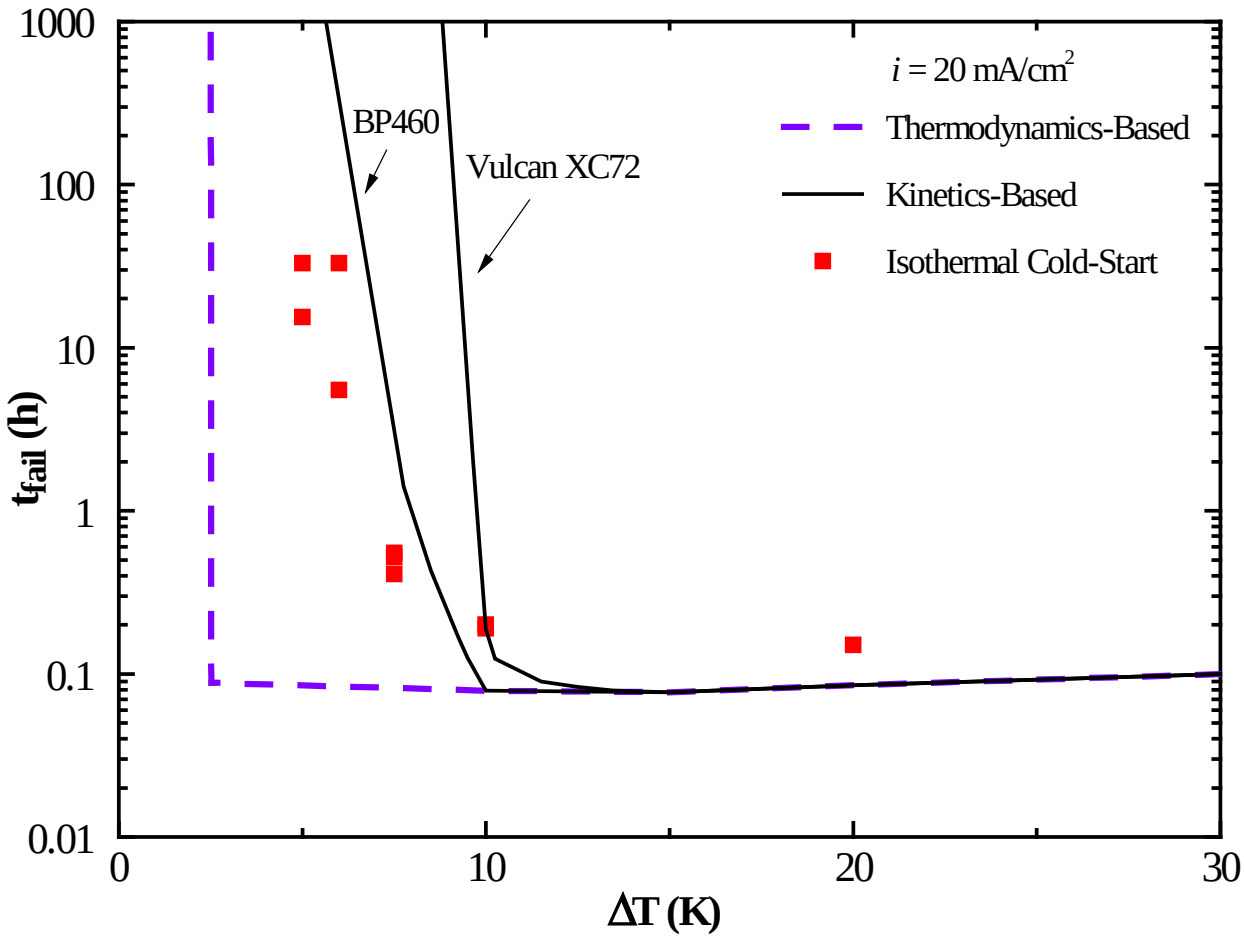

Figure 4.6. MEA-cell-failure time, t_{fail}, for isothermal galvanostatic start-up as a function of subcooling, ΔT, at a current density of 20 mA/cm^2. Solid lines are calculated using ice-crystallization kinetics for BP460 and Vulcan XC72 (with 20 wt % Pt) catalysts in a PEMFC continuum model (Appendix 4A). The dashed line is calculated using a typical thermodynamics-based rate expression (i.e., equation 4.1) [18].

4.5. Ice-Crystallization Rate Expression

To obtain a predictive ice-crystallization rate equation, $\phi(t)$ and $\bar{\tau}_i$ must be specified *a priori*. Following our previous development [20], we employ Johnson-Mehl-Avrami-Kolmogorov (JMAK) theory and classical nucleation theory (CNT). We summarize the procedure below. Additional detail is available elsewhere (i.e., see Chapter 2)[20]

Within the JMAK framework [20,25-28], $\phi(t)$ is determined by a convolution integral over nucleation and growth rates (see equation 4 of Dursch et al. [20]). For spherical, heat-transfer-limited growth under isothermal conditions in a closed system, the convolution integral reduces considerably. In this case, $\phi(t;T)$ is given by [20,21]

$$\phi(t;T) = 1 - \exp\left[-k(T)[t - \bar{\tau}_i(T)]^{5/2}\right] \tag{4.3}$$

with

$$k(T) = \frac{64\pi}{15} g(\theta) J(T) \eta_o^3(T) \alpha_L^{3/2}, \tag{4.4}$$

where α_L is liquid thermal diffusivity, $J(T)$ is the pseudo-steady-state nucleation rate, $\eta_o(T)$ is a dimensionless temperature-dependent growth parameter (see equation 9 of Dursch et al. [20]), θ is the contact angle of the ice/water/substrate triple line, and $g(\theta) = (2 + \cos\theta)(1 - \cos\theta)^2 / 4$ for heterogeneous nucleus growth on a flat surface. Equations 4.3 and 4.4 predict the ice-crystallization rates, $R_I(t;T,\phi) = \partial\phi(t;T)/\partial t$ [21], once the unknowns $J(T)$, θ, and $\bar{\tau}_i(T)$ are specified.

To obtain $\bar{\tau}_i(T)$, the definition suggested by Kaschiev [29] is adopted

$$\bar{\tau}_i(T) = \frac{1}{J(T)V_o} + \tau_g(T), \tag{4.5}$$

where V_o is liquid volume of a water-saturated cCL. The first term on the right of equation 4.5 is the expectation time for the appearance of a critical nucleus while the second term is the time required for critical nuclei to form and grow to a size detectable by the DSC. For spherical, heat-transfer-limited growth [24,29] $\tau_g(T) = (15\omega / 64\pi\, g(\theta) J(T) \eta_o^3(T) \alpha_l^{3/2})^{2/5}$, where ω, an instrument-specific constant, is 0.0173 for our DSC [21]. Thus, estimation of $\bar{\tau}_i(T)$ requires both $J(T)$ and θ.

Following our previous work [20,21], $J(T)$ is obtained from repeated τ_i measurements at a minimum of five subcoolings (e.g., see Figure 4.3). To acquire $J(T)$, a Poisson distribution is fit to measured τ_i probability distributions obtained from the repeated τ_i measurements [20,24]. CNT specifies the temperature-dependence of J [20,30,31]

$$J(T) = A\exp\left[-\frac{B}{T(\Delta T)^2}\right]. \tag{4.6}$$

Equation 4.6 indicates that a plot of $\ln J$ versus $T^{-1}(\Delta T)^{-2}$ produces a straight line with an intercept $\ln A$ and slope $-B$. Figure 4.7 confirms this behavior for the four PEMFC catalysts

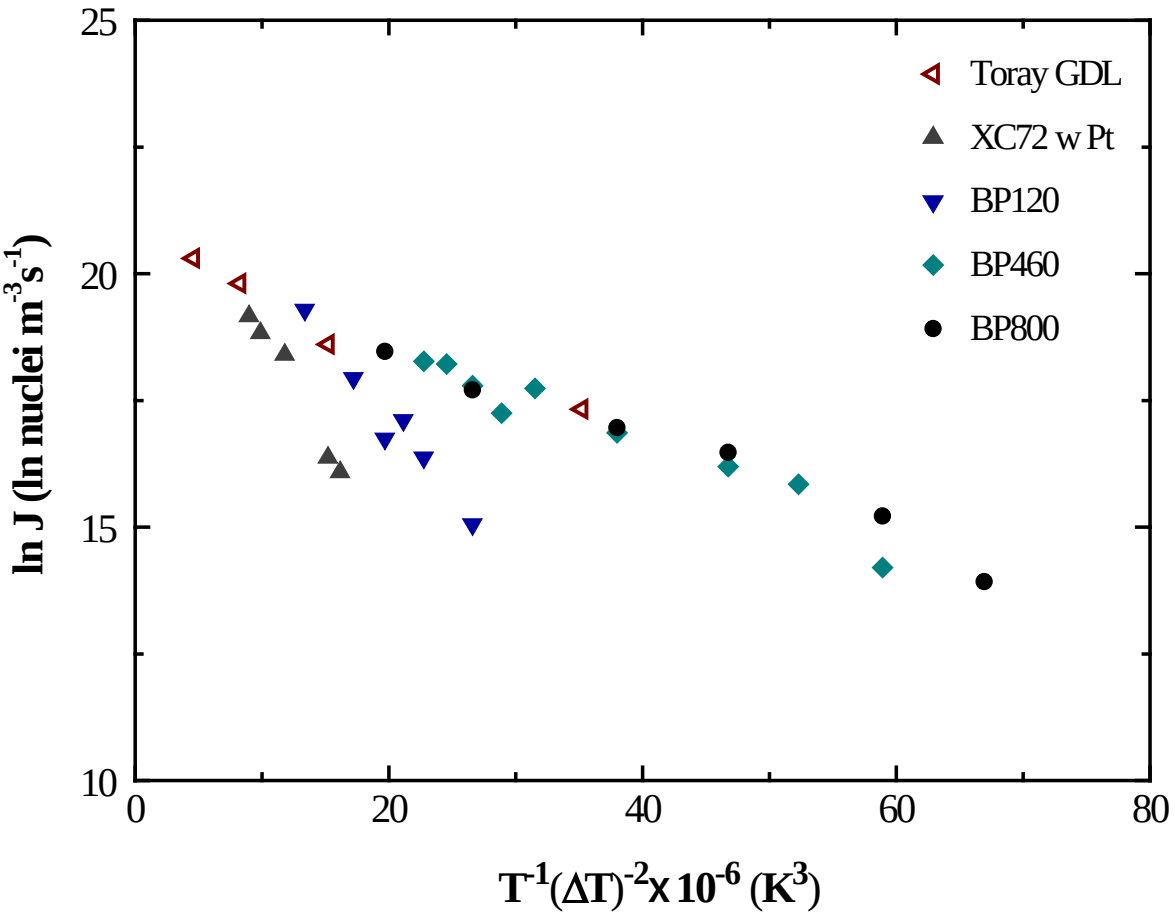

Figure 4.7. Logarithm of the nucleation rate, J, in units of nuclei/m^3/s as a function of $T^{-1}(\Delta T)^{-2}$ for a Toray gas-diffusion layer (open symbols) and four PEMFC catalysts (filled symbols). Filled symbols represents 20 wt % Pt on Vulcan XC72 (triangles), BP120 (inverted triangles), BP460 (diamonds), and BP800 (circles).

shown in Figure 4.2 (filled symbols). A Toray gas-diffusion layer (GDL) (open symbols) is included for comparison [20]. In all cases, $\ln J$ versus $T^{-1}(\Delta T)^{-2}$ is linear with $0.91 < R^2 < 0.99$, where R^2 is the square of the Pearson correlation coefficient. Obtained ice-nucleation-rate parameters, A and B in equation 4.6, are provided in Table 4.1, and their physical significance is discussed in Appendix 4B.

With $J(T)$ specified, equations 4.3-4.6 provide a predictive ice-crystallization rate valid within PEMFC cCLs. In all subsequent calculations, $\alpha_l = 1.4\times10^{-7}$ m^2/s and $\theta = 60$ and 110° for BP460/BP800 and XC72/BP120, respectively. Values of θ are discussed in detail in Appendix 4B. With these independently determined parameters, lines in Figures 4.2 and 4.4 predict $\bar{\tau}_i(T)$ and $\phi(t;T)$ for three PEMFC catalysts: BP800, BP120, and 20-wt % Pt on Vulcan XC72. In all cases, we neglect separate ice formation within the ionomer, since the fraction of freezable water is negligible compared to that in the liquid-filled voids [32]. For clarity, predictions for BP460 and Vulcan XC72 without Pt are omitted. Agreement between theory and experiment is good. Through independent assessment of $J(T)$, $\eta_o(T)$, and $\tau_g(T)$, the temperature dependences of both $\bar{\tau}_i$ and $\phi(t)$ are correctly captured. Importantly, lines in Figure 4.4 at $\Delta T = 17.5$ K show that complete ice-crystallization times are shorter for BP800 and BP120 than those for Vulcan XC72 due to an increased ice-nucleation rate (i.e., larger A and/or smaller B in Table 4.1) and consequently, a decreased $\bar{\tau}_i$.

Table 4.1. Ice-Nucleation Rate Parameters

cCL/GDL	A (× 10^{-8} nuclei m^{-3}s^{-1})	B (× 10^{-4} K^3)
Vulcan XC72	112.7	40.3
BP120	287.0	44.1
BP460	9.0	12.8
BP800	6.6	10.6
Toray GDL	[a]7.9	[a]9.4

[a] From Dursch et al. [20]

4.6. Isothermal PEMFC Cold-Start Model

4.6.1. Continuum Model:

Equations 4.3-4.6 provide an ice-crystallization rate expression valid within PEMFC catalyst layers. To investigate the importance of ice-crystallization kinetics, we compare predicted t_{fail} with the newly obtained rate expression relative to that predicted using a traditional thermodynamics-based approach (e.g., equation 4.1) [17-19] in a simplified isothermal PEMFC cold-start continuum-finite-difference model (see Appendix 4A).

Figure 4.8 illustrates the simplified 1-D geometry of the PEMFC. Dashed lines outline the spatial domain (i.e., we consider only the cCL and cGDL). Symbols a and c label the anode

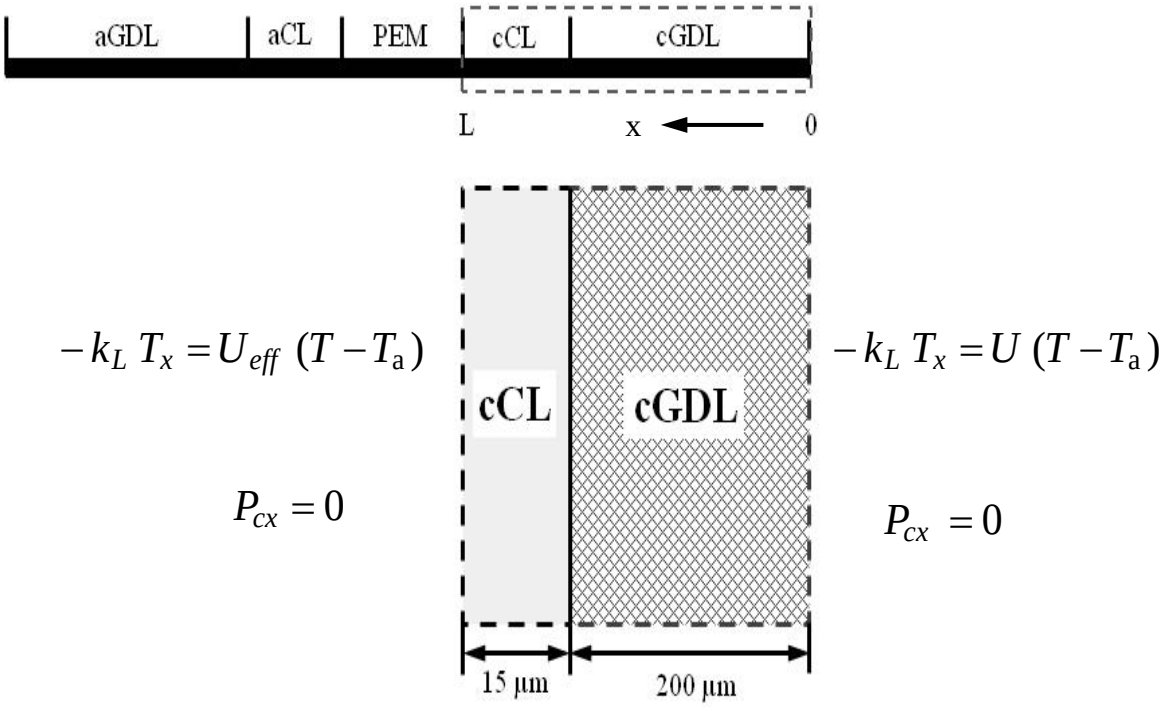

Figure 4.8. Schematic and boundary conditions for the simplified 1-D PEMFC cold-start model. Dashed lines represent the modeling domain. Subscript x indicates partial differentiation. Prefix letters a and c denote the anode and cathode, respectively.

and cathode, respectively. We neglect water transport and subsequent freezing within the anode, since the diffusivity of water in a PEM is negligible at subfreezing temperatures [5]. Meng [14], Mao et al. [15,16], Jiao et al. [17], and Balliet et al. [18,19] give more detailed 2-D and 3-D cold-start models including thermodynamics-based ice formation in both the anode and cathode. Here, we illustrate the importance of ice-crystallization kinetics.

Continuum energy and mass conservation balances are written in the cCL and cGDL for gas (G), liquid (L), and ice (I). Appendix 4A outlines the PEMFC cold-start numerical model. It is similar to those of Mao et al.[15,16] and Balliet et al. [18,19], but with important differences in the underlying physics for the ice-crystallization rate, R_I. In the current study, the ice-crystallization rate depends on the kinetics of ice nucleation and growth rather than on ice/water phase equilibria. Following our previous work [21], the ice-generation rate under pseudo-isothermal conditions, $R_I(\overline{T}_C,\phi)$ ((generated ice volume)/(water plus ice volume)/time) is given by

$$R_I(\overline{T}_C,\phi) = k(\overline{T}_C)^{2/5}[1-\phi][-\ln(1-\phi)]^{3/5} \qquad \text{for} \quad t \geq \overline{\tau}_I\,, \tag{4.7}$$

where $\overline{T}_C$ is number-average crystallization temperature, $\overline{\tau}_I$ is number-average non-isothermal induction time, ϕ is gas-free volume fraction of ice within the pores defined by $\phi \equiv S_I/(S_I+S_L)$, and $k(\overline{T}_C)$ is given by equation 4.4, but evaluated at the number-average crystallization temperature, $\overline{T}_C$ [21]. Equation 4.7 applies only for $t > \overline{\tau}_I$ (i.e., the non-isothermal induction time). $\overline{\tau}_I$ is given by [21]

$$\int_0^{\overline{\tau}_I} \frac{dt}{\overline{\tau}_i(T)} = 1\,, \tag{4.8}$$

where $\overline{\tau}_i(T)$ follows from the first term on the right of equation 4.5, as well as equation 4.6. We note that for calculation of $\overline{\tau}_i(T)$ during PEMFC cold-start, the instrument-specific growth term does not apply. In equation 4.5, $\overline{\tau}_i(T)$ depends on liquid volume in either the cCL or GDL, V_o. To eliminate the volume dependence of $\overline{\tau}_i(T)$ in the continuum MEA-cold-start model, we evaluate $\overline{\tau}_i(T)$ for large V_o (i.e., the fastest onset of ice crystallization). The approximation of "large volume" is valid since for small ΔT, $\overline{\tau}_i(T)$ depends only on $J(T)$ and not on V_o [21].

Coupled, nonlinear differential-algebraic equations (equations 4.4-4.8 and 4A.1-4A.6) are solved simultaneously subject to the boundary conditions provided in Figure 4.8. U_{eff} is the overall effective heat-transfer coefficient that includes heat conduction through the anode and external convection. In all cases, temperature is uniform at the isothermal ambient subcooling, $\Delta T = 273.15 - T_a$, where T_a is the ambient temperature. Similar to Jiao et al. [17] and Balliet et al. [18,19], the initial liquid-water saturation, S_{Lo}, is 0.34 and 0.22 in the cCL and cGDL, respectively. In both the cCL and cGDL, initial gas pressure is uniform at 101.3 kPa. Equations are solved numerically in Matlab R2010a (The Math Works Inc., Natick, MA) using finite differencing and Newton iteration to resolve nonlinearities with a tolerance of 10^{-7}, a time step of 10^{-2} s, and 50 mesh elements. A Thomas algorithm inversion scheme BAND(j) solves the resulting tridiagonal matrices [33]. All model parameters are reported in Table 4.2.

Table 4.2. Model Parameters

Parameter	cCL	cGDL
ε_o	0.6 [18]	0.8 [20]
$\overline{\rho\hat{C}}_p$ (kJ m^{-3} K^{-1})	990 [19]	970 [19]
$\bar{k}_T$ (W m^{-1} K^{-1})	1.2 [18]	1.5 [18, 35]
k_o (m^{-2})	1.6×10^{-15} [19]	3.4×10^{-12} [19]
η_s (V)	0.55 [a]	–
Π (V)	-0.012 [19]	–
U (W m^{-2} K^{-1})	100 [18]	90 [18]
$A\times10^{-8}$ (nuclei m^{-3} s^{1})	9 to 112.7	7.9 [20]
$B\times10^{-4}$ (K^3)	12.8 to 40.3	9.4 [20]

[a] calculated from measured cell voltage in Figure 4.5

4.6.2. Model Results:

Figure 4.9 displays typical calculated liquid-water saturations, S_L, as a function of time, t, at the coldest boundaries of the cCL ($x = L$) and cGDL ($x = 0$) at equal subcoolings, ΔT, of 10 K at $x = 0, L$ and $i = 20$ mA/cm^2. Solid lines reflect the proposed ice-crystallization kinetic model (i.e., equations 4.4-4.8) for the Vulcan XC72 catalyst and the Toray cGDL in Table 4.1. Initially, S_L slightly increases in both the cCL and cGDL as a result of water generation in the cCL and subsequent migration to the cGDL due to a gradient in capillary pressure. S_L continues to increase until crystallization first commences in the cGDL at the number-average non-isothermal induction time, $\bar{\tau}_{I,cGDL}$, where liquid water rapidly transforms into ice [20,21,34]. In the cCL, $\bar{\tau}_{I,cCL}$ is considerably longer than that in the cGDL due to slower ice nucleation rates (see Table 4.1). Consequently, S_L increases over a longer time period prior to freezing. S_L and T profiles at given times are omitted, as both are essentially uniform due to a small Biot number ($Bi = 0.002$) and a fast time-scale for water movement.

Conversely, dashed and dotted lines in Figure 4.9 are calculated using a thermodynamics-based approach (i.e., equation 4.1) [18]. Dashed and dotted lines correspond to $k_f = 0.25$ and 1 kg/m^{3}s, respectively [18]. In this approach, freezing begins once the local liquid temperature is less than the equilibrium freezing temperature, T_o. For $\Delta T = 10$ K, T is well below T_o within the cCL (270.2 to 271.1 K [11]) and within the cGDL (273.0 K [11,35]). Accordingly, S_L

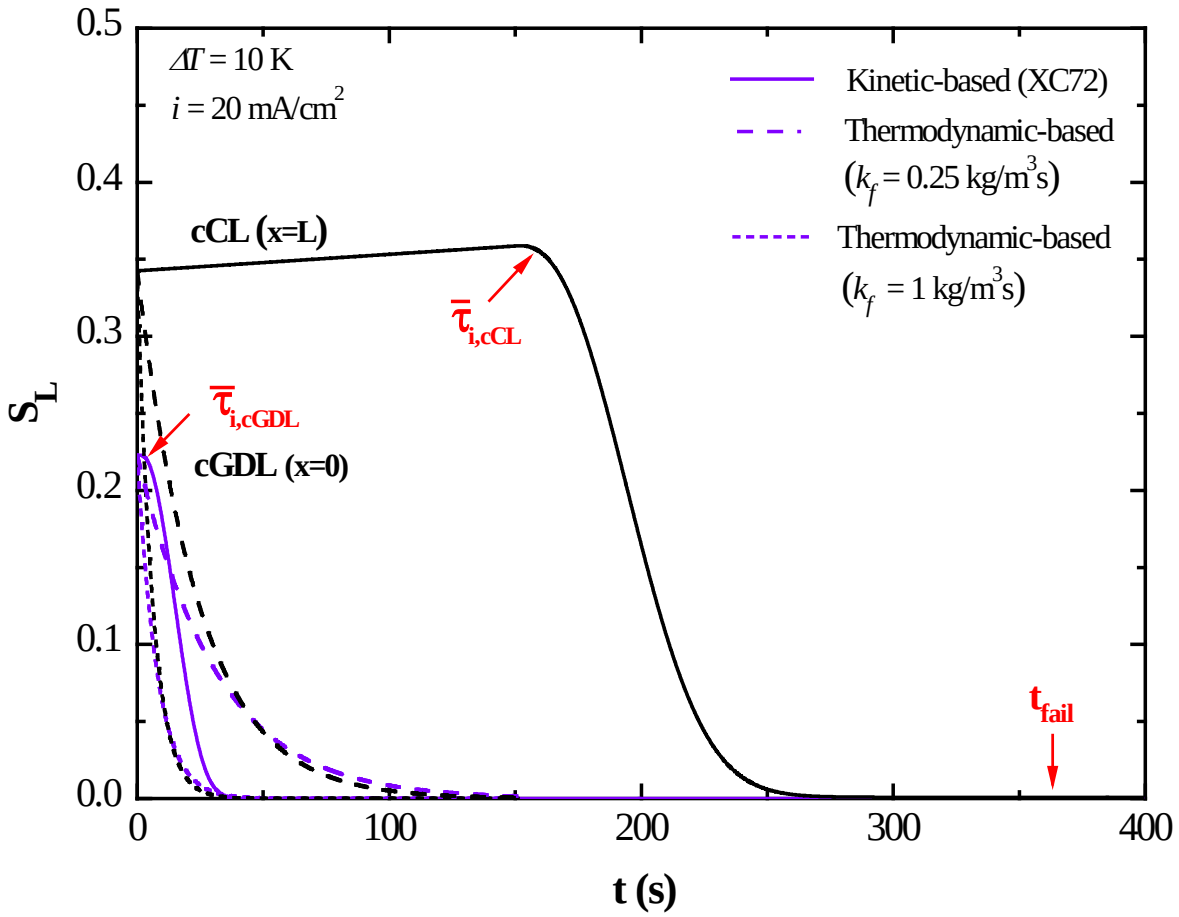

Figure 4.9. Calculated liquid-water saturation, S_L, as a function of time, t, at the coldest boundary of the cCL ($x = L$) and cGDL ($x = 0$) for equal subcoolings, ΔT, of 10 K. Solid lines are calculated using ice-crystallization kinetics for the Vulcan XC72 cCL and the Toray cGDL. Dashed and dotted lines are predicted using equation 4.1 with k_f = 0.25 and 1 kg/m^{3}s, respectively [18]. Symbols $\bar{\tau}_{I,cGDL}$ and $\bar{\tau}_{I,cCL}$ label the number-average non-isothermal induction times in the cCL and the cGDL, respectively. The symbol t_{fail} labels the MEA-cell-failure time.

decreases abruptly in both cases due to nearly immediate freezing. In this calculation, we neglect the relatively narrow pore-size distributions of the cGDL or cCL [18,19]. Figure 4.9 highlights the importance of $\bar{\tau}_I$ for forestalling freezing especially in the cCL.

The likelihood of successful cold-start depends strongly on temperature through $\bar{\tau}_I$. Thus, to elucidate those conditions for which including ice-crystallization kinetics is critical, we examine isothermal cell-failure time for various subcoolings, ΔT. We define a cell-failure time, t_{fail}, as the time when ice reaches a critical saturation, S_{Ifail}, thereby choking the cell [34]. In all cases, S_{Ifail} is taken as 0.38 or 0.55 in the cCL and cGDL, respectively. In the cCL, $S_{Ifail} = 0.38$ is obtained from a fit of measured cell voltage versus time at $\Delta T = 10$ K and $i = 20$ mA/cm^2. In the cGDL, however, $S_{Ifail} = 0.55$ is taken as the saturation when the effective oxygen diffusion coefficient reaches a limiting value [36,37], taken as 0.03 in all cases. A partially ice-saturated cCL and cGDL (i.e., $S_{Ifail} < 1$) at cell failure is consistent with experimental observation [3,4,38].

Solid and dashed lines in Figure 4.6 compare predicted to measured (symbols) t_{fail} versus ΔT for an isothermal galvanostatic cold-start. Solid lines correspond to ice-crystallization kinetics (i.e., equations 4.4-4.8) for two cCL carbon-support materials with considerably different ice-crystallization kinetics: Vulcan XC72 and BP460. The dashed line is predicted using a traditional thermodynamics-based approach with $k_f = 0.25$ kg/m^{3}s [18]. In all cases, t_{fail} decreases substantially with increasing ΔT, in good agreement with experiment. In both the kinetic and thermodynamic approaches, t_{fail} decreases to a limiting value of approximately 0.1 h. Accordingly, two limiting regimes for t_{fail} are evident in Figure 4.6. For small subcoolings (i.e., $\Delta T < 3$ K and $\Delta T < 11$ K for thermodynamic and kinetic freezing, respectively), t_{fail} is limited by freezing, whereas for larger subcoolings, t_{fail} is limited by water production. Figure 4.9 illustrates the latter case. Here, predicted t_{fail} is larger than the time required for ice crystallization (i.e., 40 and 260 s in the cGDL and cCL, respectively), since $S_I < S_{Ifail}$ upon complete crystallization of all liquid water present. S_I increases further to S_{Ifail} only as newly-generated water freezes. In Figure 4.6, measured and predicted t_{fail} is for a current density, i, of 20 mA/cm^2. Significantly, our numerical model reveals that current densities greater than 20 mA/cm^2 likewise exhibit cell-failure times with two limiting regimes, as in Figure 4.6. Furthermore, t_{fail} decreases monotonically with increasing current density in the water-production-limited regime (i.e., $\Delta T > 11$ K), as discussed elsewhere [3,6-8,19,38].

In both the cCL and cGDL, $\bar{\tau}_I$ decreases significantly with increasing subcooling (e.g., see Figure 4.2). Consequently, as subcooling extends beyond $\Delta T = 11$ K, $\bar{\tau}_I$ is negligible in both cell domains, and ice-crystallization kinetics is well approximated by the thermodynamic-based approach. We conclude that including ice-crystallization kinetics is critical in the "nucleation-limited" regime (see Figure 14 of Dursch et al. [20]) where induction times are long (i.e., from $3 \le \Delta T \le 10$ K in Figure 4.6). However, the particular ΔT that establishes the "nucleation-limited" regime relies heavily on all heat transfer and kinetic parameters (e.g., U,

U_{eff}, $\bar{k}_T$, and $J(T)$). These controlling parameters can be adjusted to lengthen $\bar{\tau}_I$, significantly delaying or even preventing ice formation [34].

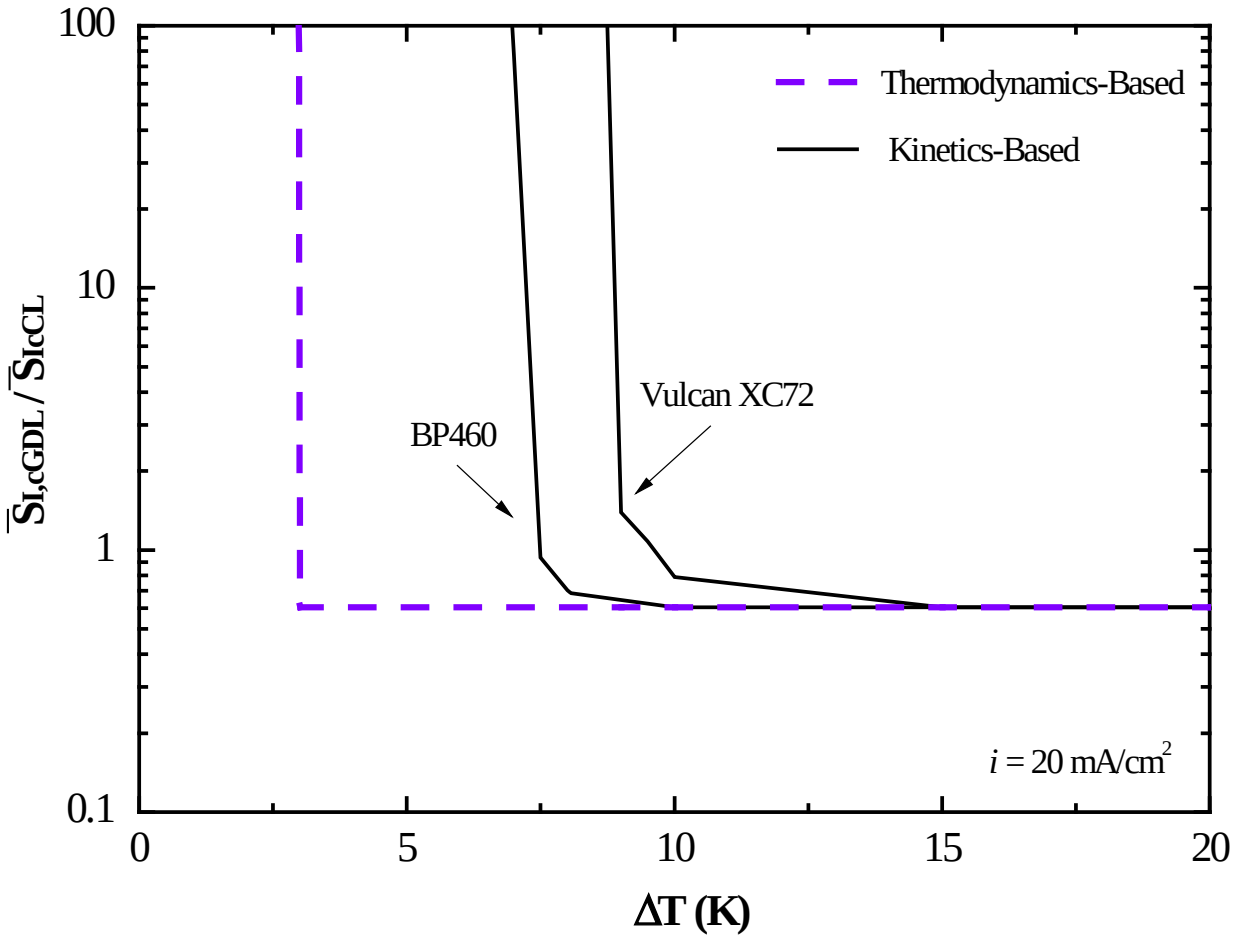

Figure 4.10. Ratio of the average ice saturation in the cGDL to that in the cCL, $\bar{S}_{I,cGDL} / \bar{S}_{I,cCL}$, as a function of subcooling, ΔT, at a current density of 20 mA/cm^2. Solid lines are calculated using ice-crystallization kinetics in the BP460 and Vulcan XC72 cCLs and the Toray cGDL. The dashed line is calculated using a typical thermodynamics-based rate expression (i.e., equation 4.1) [18].

The ice distribution at cell failure in both the cCL and cGDL depends strongly on subcooling through $\bar{\tau}_{I,cGDL}(T)$ and $\bar{\tau}_{I,cCL}(T)$. Figure 4.10 displays the ratio of spatially-averaged ice saturation in the cGDL to that in the cCL, $\bar{S}_{I,cGDL} / \bar{S}_{I,cCL}$, as a function of subcooling, ΔT, for $i = 20$ mA/cm^2. Solid lines are calculated using ice-crystallization kinetics in the BP460 and Vulcan XC72 cCLs and the Toray cGDL. The dashed line is calculated using the previous thermodynamics-based rate expression (see equation 4.1) [18]. Similar to t_{fail} in Figure 4.6, $\bar{S}_{I,cGDL} / \bar{S}_{I,cCL}$ decreases substantially with increasing ΔT in all cases. In both the kinetic and thermodynamic approaches, $\bar{S}_{I,cGDL} / \bar{S}_{I,cCL}$ decreases to a limiting value of approximately 0.6. At these subcoolings (i.e., $\Delta T > 3$K and $\Delta T > 9$ K for thermodynamic and kinetic freezing, respectively), rapid ice crystallization occurs within the cCL, preventing water migration into the cGDL. Accordingly, there are also two limiting regimes for $\bar{S}_{I,cGDL} / \bar{S}_{I,cCL}$ in Figure 4.10. For small subcoolings (i.e., $\Delta T < 9$ K), $\bar{S}_{I,cGDL} / \bar{S}_{I,cCL}$ is limited by $\bar{\tau}_{I,cGDL}(T)$, whereas for larger subcoolings $\bar{S}_{I,cGDL} / \bar{S}_{I,cCL}$ is limited by $\bar{\tau}_{I,cCL}(T)$. This finding is consistent with Ge et al. [2], who observed two limiting regimes in an operating PEMFC during cold-start using *in-situ* visible imaging. Equations 4.4-4.8 and 4A.1-4A.6 do not allow for ice propagation between the cCL and cGDL, since the shortest induction time controls cell failure. Accordingly, the two limiting regimes in Figure 4.10 emphasize the importance of ice-crystallization kinetics in both the cCL and cGDL.

4.7. Conclusions

We determine isothermal ice-crystallization rates and ice-nucleation rates from heat-flow and induction-time measurements in fuel-cell catalysts layers using differential scanning calorimetry. Isothermal ice-crystallization rates and ice-nucleation rates are obtained as a function of subcooling for four commercial carbon-support materials, with various ionomer fractions and platinum loadings. Measured induction times follow expected trends from classical nucleation theory and reveal that both the carbon-support material and ionomer fraction considerably impact the rate of ice formation. Conversely, dispersed platinum particles play little role in ice crystallization. Following our previous approach, a nonlinear ice-crystallization rate expression is obtained from Johnson-Mehl-Avrami-Kolmogorov theory.

To validate ice-crystallization kinetics within PEMFCs, we measure cell-failure time as a function of subcooling during isothermal galvanostatic cold-start in a commercial MEA. Significantly, cell-failure time decreases with decreasing temperature due to a shorter required time for ice nucleation. Using a 1D PEMFC isothermal numerical cold-start model, we compare cell-failure times predicted using the newly obtained rate expression to those predicted using a traditional thermodynamics-based approach. Cell-failure times predicted using ice-freezing kinetics are in good agreement with experiment. The PEMFC cold-start model demonstrates that ice-crystallization kinetics is critical when induction times are long (i.e., in the “nucleation-limited" regime for $T > 263$ K). However, the particular temperature that establishes the “nucleation-limited” regime relies heavily on all heat-transfer and kinetic parameters. Accordingly, these controlling parameters can be adjusted to lengthen induction times, significantly delaying or even preventing ice formation.

4.8. List of Symbols

A ice-nucleation-rate constant (nuclei/m^3/s)

B ice-nucleation-rate constant (K^3)

i current density (A/m^3)

J pseudo-steady-state nucleation rate (nuclei/m^3/s)

k overall crystallization rate constant ($s^{-2.5}$)

k_f equilibrium freezing rate constant ($kg/m^3/s$)

k_k effective permeability of phase k (m^{-2})

k_B Boltzmann constant (J/molecule/K)

P_C capillary pressure, $P_G - P_L$ (Pa)

$\dot{Q}$ heat-flow rate (mW)

r^* critical-nucleus radius (nm)

R_I ice-generation rate ((generated ice volume)/(water plus ice volume)/time)

R_S seed-particle radius (nm)

S saturation

t time (s)

t_{fail} MEA-cell-failure time (s)

T temperature (K)

T_C crystallization temperature (K)

ΔT subcooling (K)

U overall heat transfer coefficient ($W/m^2/K$)

U_{eff} effective overall heat transfer coefficient ($W/m^2/K$)

V volume (m^3)

Greek Letters

α thermal diffusivity (m^2/s)

ε volume fraction

ε_o bulk porosity

γ surface tension (mN/m)

η_o dimensionless thermal-growth constant

η_s surface overpotential (V)

θ contact angle

τ_g time for nuclei grow to an instrument-detectable size (s)

τ_i isothermal induction time (s)

τ_I non-isothermal induction time (s)

ϕ gas-free ice volume fraction

ω instrument constant, 0.0173

Ψ heterogeneous nucleation shape factor in equation 4B.1

Subscripts

a anode

c cathode

G gas

I ice

k phase

L water

o initial

4.9. Acknowledgements

This work was funded by the Assistant Secretary for Energy Efficiency and Renewable Energy, Fuel Cell Technologies Office, of the U. S. Department of Energy under contract number DE-AC02-05CH11231.

4.10. References

[1] E. Cho, J.J. Jo, H.Y. Ha, S. Hong, K. Lee, T. Lim, I. Oh, Characteristics of the PEMFC repetitively brought to temperatures below 0 °C, J. Electrochem. Soc. 150 (2003) A1667-A1670.

[2] S. Ge, C-Y. Wang, In situ imaging of liquid water and ice formation in an operating PEFC during cold start, Electrochem. Sold-State Lett. 9 (2006) A499-A503.

[3] K. Tajiri, Y. Tabuchi, F. Kagami, S. Takahashi, K. Yoshizawa, C.Y. Wang, Effects of operating and design parameters on PEFC cold start, J. Power Sources 165 (2007) 279-286.

[4] S. Ge, C.Y. Wang, Cyclic voltammetry study of ice formation in the PEFC catalyst layer during cold start, J. Electrochem. Soc. 154 (2007) B1399-B1406.

[5] Y. Hiramitsu, N. Mitsuzawa, K. Okada, M. Hori, Effects of ionomer content and oxygen permation of the catalyst layer on proton exchange membrane fuel cell cold start-up, J. Power Sources 195 (2010) 1038-1045.

[6] Y. Hishinuma, T. Chikahisa, F. Kagami, T. Ogawa, The design and performance of a PEFC at a temperature below freezing, Japan Soc. Mech. Eng. Int. J. 47 (2004) 235-241.

[7] Y. Tabe, M. Saito, K. Fukui, T. Chikahisa, Cold start characteristics and freezing mechanism dependence on start-up temperature in a polymer electrolyte membrane fuel cell, J. Power Sources 208 (2012) 366-373.

[8] P. Oberholzer, P. Boillat, R. Siegrist, R. Perego, A. Kästner, E. Lehmann, G.G. Scherer, A. Wokaun, Cold-start of a PEFC visualized with high resolution dynamic in-plane neutron imaging, J. Electrochem. Soc. 159 (2011) B235-B245.

[9] R. Satija, D.L. Jacobson, M.A. Arif, S. A. Werner, In situ neutron imaging technique for evaluation of water management sytems in operating PEM fuel cells, J. Power Sources 129 (2003) 238-245.

[10] G. Hwang, H. Kim, R. Lujan, R. Mukundan, D. Spernjak, R.L. Borup, M. Kaviany, M.H. Kim, A.Z. Weber, Phase-change-related degradation of catalyst layers in proton-exchange-membrane fuel cells, Electrochim. Acta 95 (2013) 29-37.

[11] Y. Ishikawa, T. Morita, K. Nakata, K. Yoshida, M. Shiozawa, Behavior of water below the freezing point in PEFCs, J. Power Sources 163 (2007) 708-712.

[12] Y. Ishikawa, H. Hamada, M. Uehara, M. Shiozawa, Super-cooled water behavior inside polymer electrolyte fuel cell cross-section below freezing temperature, J. Power Sources 179 (2008) 547-552.

[13] S. Ge, C.Y. Wang, Characteristics of subzero startup and water/ice formation on the catalyst layer in a polymer electrolyte fuel cell, Electrochim. Acta 52 (2007) 4825-4835.

[14] H. Meng, A PEM fuel cell model for cold-start simulations, J. Power Sources 178 (2008) 141-150.

[15] L. Mao, C.Y. Wang, Y. Tabuchi, A multiphase model for cold start of polymer electrolyte fuel cells, J. Electrochem. Soc. 154 (2007) B341-B351.

[16] L. Mao, C.Y. Wang, Analysis of cold start in polymer electrolyte fuel cells, J. Electrochem. Soc. 154 (2007) B139-B146.

[17] K. Jiao, X. Li, Three-dimensional multiphase modeling of cold start processes in polymer electrolyte membrane fuel cells, Electrochim. Acta 54 (2009) 6876-6891.

[18] R. Balliet, K.E. Thomas-Alyea, J. Newman, Water movement during freezing in a polymer-electrolyte-membrane fuel cell, ECS Trans. 16 (2008) 285-296.

[19] R. Balliet, J. Newman, Cold start of a polymer-electrolyte fuel cell I. Development of a two-dimensional model, J. Electrochem. Soc. 158 (2011) B927-B938.

[20] T.J. Dursch, M.A. Ciontea, C.J. Radke, A.Z. Weber, Isothermal ice-crystallization kinetics in the gas-diffusion layer of a proton-exchange-membrane fuel cell, Langmuir 28 (2012) 1222-1234.

[21] T.J. Dursch, M.A. Ciontea, G.J. Trigub, C.J. Radke, A.Z. Weber, Pseudo-isothermal ice-crystallization kinetics in the gas-diffusion layer of a fuel cell from differential scanning calorimetry, Int. J. Heat Mass Trans. 60 (2013) 450-458.

[22] D.C. Huang et al., Effect of dispersion solvent in catalyst ink on proton exchange membrane fuel cell performance, Int. J. Electrochem. Sci. 6 (2011) 2551-2565.

[23] A. Kusoglu, A. Kwong, K.T. Clark, H.P. Gunterman, A.Z. Weber, Water uptake of fuel-cell catalyst layers, J. Electrochem. Soc. 159 (2012) F530-F535.

[24] S. Jiang, J.H. Horst, Crystal nucleation rates from probability distributions of induction times, Crystal Growth Design 11 (2011) 256-261.

[25] M. Avrami, Kinetics of phase change I. general theory, J. Chem. Phys. 7 (1939) 1103-1112.

[26] M. Avrami, Kinetics of phase change II. transformation-time relations for random distribution of nuclei, J. Chem. Phys. 8 (1940) 212-224.

[27] W.A. Johnson, R.F. Mehl, Reaction kinetics in processes of nucleation and growth, AIME Trans. 135 (1939) 416.

[28] A.N. Kolmogorov, Selected Works of A.N. Kolmogorov, vol. 1, Kluwer Academic Publishers, Dodrecht, 1985, pp. 530-560.

[29] D. Kashchiev, Induction time and metastability limit in new phase formation, J. Crystal Growth 110 (1991) 373-380.

[30] D.R. Uhlmann, B. Chalmers, The energetics of nucleation, Ind. Eng. Chem. 57 (1965) 19-31.

[31] D. Kashchiev, Nucleation: Basic Theory with Applications, 1st ed., Butterworth-Heinemann, Oxford, 2000.

[32] H.R. Corti, F. Nores-Pondal, M.P. Buera, Low temperature thermal properties of Nafion 117 membranes in water and methanol-water mixtures, J. Power Sources 161 (2006) 799-805.

[33] J. Newman and K.E. Thomas-Alyea, Electrochemical Systems, John Wiley & Sons, New York, 2004, p. 611.

[34] T.J. Dursch, J.F. Liu, G.J. Trigub, C.J. Radke, A.Z. Weber, Ice-crystallization kinetics and water movement in gas-diffusion and catalyst layers, ECS Trans. 50 (2012) 429-435.

[35] T.J. Dursch, J.F. Liu, G.J. Trigub, C.J. Radke, A.Z. Weber, Non-isothermal melting of ice in the gas-diffusion layer of a proton-exchange-membrane fuel cell, Int. J. Heat Mass Trans. 67 (2013) 896-901.

[36] G.S. Hwang, A.Z. Weber, Effective-diffusivity measurement of partially-saturated fuel-cell gas-diffusion layers, J. Electrochem. Soc. 159 (2012) F683-F692.

[37] T. Rosén, J. Eller, J. Kang, N.I. Prasianakis, J. Mantzaras, F.N. Büchi, Saturation dependent effective transport properties of PEFC gas diffusion layers, J. Electrochem. Soc. 159 (2012) F536-F544.

[38] K. Tajiri, Y. Tabuchi, C-Y Wang, Isothermal cold start of polymer electrolyte fuel cells, J. Electrochem. Soc. 154 (2007) B147-B152.

[39] X. Li, F. Feng, K. Zhang, S. Ye, D. Kwok, V. Birss, Wettability of nafion and nafion/vulcan carbon composite films, Langmuir 28 (2012) 6698-6705.

[40] A.Z. Weber, J. Newman, Modeling transport in polymer-electrolyte fuel cells, Chem. Rev. 104 (2004) 4679-4726.

[41] A.Z. Weber, Improved modeling and understanding of diffusion-media wettability on polymer-electrolyte-fuel-cell performance, J. Power Sources 195 (2010) 5292-5304.

Appendix 4A. PEMFC Cold-Start Continuum Model

Within the cCL and cGDL, we write continuum differential energy and mass conservation balances for gas (G), liquid (L), and ice (I). In each subdomain, phase saturations sum to unity, i.e., $S_G + S_L + S_I = 1$, where the saturation of a phase k, S_k, is defined as volume of phase k per pore volume, or $\varepsilon_k / \varepsilon_o$, where ε_k is porosity of phase k and ε_o is bulk porosity. Upon thermal equilibrium among all phases [15-19], the 1-D, transient energy balance to calculate transient temperature distributions, $T(x,t)$, in each subdomain is

$$\overline{\rho\hat{C}}_p \frac{\partial T}{\partial t} = \bar{k}_T \frac{\partial^2 T}{\partial x^2} + \rho_I \varepsilon_o \Delta\hat{H}_f \left(S_L + S_I\right) R_I + \dot{Q}_{rxn} \text{ ,} \tag{4A.1}$$

where $\overline{\rho\hat{C}}_p$ is volume-averaged heat capacity, $\bar{k}_T$ is volume-averaged thermal conductivity, ρ_I is ice mass density, and R_I is the rate of ice formation ((generated ice volume)/(water plus ice volume)/time) [21]. In equation 4A.1, $\dot{Q}_{rxn} = i(\eta_s + \Pi)/L_{cCL}$ in the cCL and zero in the cGDL, where i is volumetric current density, η_s is total overpotential (calculated from measured cell voltage in Figure 4.5 [40]), L_{cCL} is cCL thickness, and Π is the Peltier coefficient [40]. The second and third terms on the right side of equation 4A.1 represent enthalpy liberation due to crystallization and reaction, respectively. Because of the low subcoolings used in the calculations, heat generation (or consumption) due to evaporation, condensation, sublimation, and deposition (i.e., frosting) are neglected. Additionally, current density in $\dot{Q}_{rxn}$ increases linearly with increasing S_G, so that higher ice and water saturations choke the electrochemical production of liquid water [19]. More involved models are discussed elsewhere [15-19].

In each subdomain, gas-, liquid-, and ice-phase saturations obey the following mass-conservation equations combined with Darcy's law [15-19]

$$\varepsilon_o \rho_G \frac{\partial S_G}{\partial t} = \frac{\partial}{\partial x}\left(\frac{\rho_G k_G[S_G]}{\eta_G} \frac{\partial P_G}{\partial x} \right), \tag{4A.2}$$

$$\varepsilon_o \rho_L \frac{\partial S_L}{\partial t} = \frac{\partial}{\partial x}\left(\frac{\rho_L k_L[S_L]}{\eta_L} \frac{\partial P_L}{\partial x} \right) - \rho_I \varepsilon_o \left(S_L + S_I\right) R_I + R_{rxn} \tag{4A.3}$$

and

$$\varepsilon_o \rho_I \frac{\partial S_I}{\partial t} = \rho_I \varepsilon_o (S_L + S_I) R_I \tag{4A.4}$$

where $R_{rxn} = iM_{H_2O}/2F$ in the cCL and R_{rxn} equals zero in the cGDL, η is viscosity, P is pressure, M_{H_2O} is the molar mass of water, and $k_k[S_k]$ is the effective permeability of phase k as a function of S_k. The first, second, and third terms on the right of equation 4A.3 represent water movement due to a gradient in capillary pressure, $P_C \equiv P_G - P_L$, water depletion due to freezing, and water generation due to reaction, respectively. The effective permeabilities in equations 4A.2 and 4A.3 follow the relation $k_k = k_o S_k^3$, where k_o is absolute permeability [19]. Following others [15-19], residual saturations are neglected. To relate capillary pressure, $P_C \equiv P_G - P_L$, to liquid saturation, capillary equilibrium (i.e., Young-Laplace) and a bundle-of-

capillaries model are used [41]. Capillary pressure-saturation relationships used in this work are identical to those measured by Kusoglu et al. [23] A detailed description of mixed-wettability for the cCL and cGDL is found in Balliet et al. [19].

Appendix 4B. Ice-Nucleation-Rate Parameters

$\phi(t;T)$ and $\bar{\tau}_i(T)$ in equations 4.3-4.5 require independent assessment of the ice/water/substrate triple line contact angle, θ. Since A is independent of θ, $J(T)$ depends on θ only through the parameter B. From CNT, B is related to the Gibbs-free energy of critical-nucleus formation, ΔG^*, by [20,30] (e.g., see equation 2A.7 of Appendix 2A)

$$B(\theta) = \frac{(\Delta T)^2 \Delta G^*}{k_B} = \frac{4\pi\gamma_{sl}^3 T_o^2 \hat{v}_I^2}{3\Delta \hat{H}_f^2 k_B} g(\theta) \tag{4B.1}$$

where k_B is the Boltzmann constant, γ_{sl} is solid/liquid interfacial energy, and $\hat{v}_I$ is ice specific volume.

From Table 4.1 and equation 4B.1, similar values of B for BP460/BP800 and a Toray GDL [21] suggest that θ for BP460/BP800 is approximately equal to that of the GDL, or $\theta = 60^\circ$. Unlike BP460/BP800, however, BP120/Vulcan XC72 has significantly decreased ice-nucleation rates (evidenced by larger B in Table 4.1). Values of B are roughly 4 times larger for BP120/Vulcan XC72 than for BP460/BP800, characteristic of an increased contact angle, θ. Equation 4B.1 demonstrates that B (and ΔG^*) increases with θ. Thus, for an increase in θ from 60 to 110° for BP120/Vulcan XC72, ΔG^* increases by a factor of 4-5, consistent with measured B values. For BP120/Vulcan XC72, a larger θ is conceivably due to an increased coverage of the ionomer, comprised of a non-ice-wetting PTFE backbone [39]. This result is similar to our previous finding where ice nucleation occurs more slowly on hydrophobic PTFE-coated GDL fibers than hydrophilic oxidized-carbon fibers [20].

To investigate further the effect of ionomer coverage on ice nucleation, the carbon:Nafion mass ratio was varied from 5:1 to 5:8 for BP800 and Vulcan XC72. Measured values of A and B, obtained as in Section 4.5, are listed in Table 4B.1. For BP800, B increases from 10.6 to 43.5 as the carbon:Nafion mass ratio increases from 5:2 to 5:8. This result suggests an increase in ionomer coverage, and consequently, an increase in θ from 60° to approximately 110°, as for BP120/Vulcan XC72. For Vulcan XC72, however, an increased carbon:Nafion mass ratio results in no further increase in B (likely due to a smaller particle surface area). Conversely for Vulcan XC72, as the carbon:Nafion mass ratio is decreased, B decreases significantly from 41.6 to 18.9. This indicates decreased ionomer coverage and, similar to BP800 (with 5:2 carbon:Nafion), a smaller value of θ.

To account for contributions of curvature and seed-particle (particle serving as a nucleation site, e.g., platinum and carbon) size to ΔG^*, we replace $g(\theta)$ in equation 4B.1 with $\Psi^3(\theta, x^*)$ (see equation 18.10 in Kashchiev [29]), where $x^* = R_S / r^*(T)$ is the ratio of seed-particle to critical-nucleus radius. For heterogeneous growth of a nucleus on a flat surface, $\Psi^3(\theta, x^*) = g(\theta)$ as expected [30]. Figure 4B.1 shows calculated dimensionless Gibbs-free energy of critical-nucleus formation, $\Delta G^* / k_B T$, versus dimensionless seed-particle radius,

$x^* = R_S / r^*(T)$, for $\theta = 60$ and 110°. Solid and dashed lines denote subcoolings of 12.5 K and 15 K, respectively. Arrows label minimum and maximum x^* for platinum (3-5 nm diameter) and the carbon support (30-50 nm diameter) within the cCLs. Several features are salient. Primary carbon particles are much larger than growing nuclei (ranging from 2-4 nm diameter depending on ΔT). Thus, in this case, $x^* >> 1$, and nuclei grow as solid segments on a flat surface, similar to those in a GDL [20,21]. Compared to the carbon support, ΔG^* is significantly larger for dispersed platinum. Since platinum particles are similar in size to growing nuclei, a larger surface area is required to maintain a given θ, increasing ΔG^*. As a result, ice nuclei form preferentially on the carbon support, in agreement with the $\bar{\tau}_i(T)$ and $\phi(t;T)$ measurements (see Figures 4.2 and 4.4). Furthermore, lines in Figure 4B.1 illustrate that ΔG^* (and B) increases with θ as discussed previously.

Table 4B.1. Ice-Nucleation Rate Parameters with Varying Carbon:Nafion Mass Ratio

Catalyst	**Carbon:Nafion Mass Ratio**	***A* (× 10^{-8} nuclei $m^{-3}s^{-1}$)**	***B* (× 10^{-4} K^3)**
Vulcan XC72	5:1	13.3	18.9
	5:2	112.7	40.3
	5:4	103.4	41.6
BP800	5:2	4.6	10.6
	5:4	110.0	17.1
	5:8	305.9	43.5

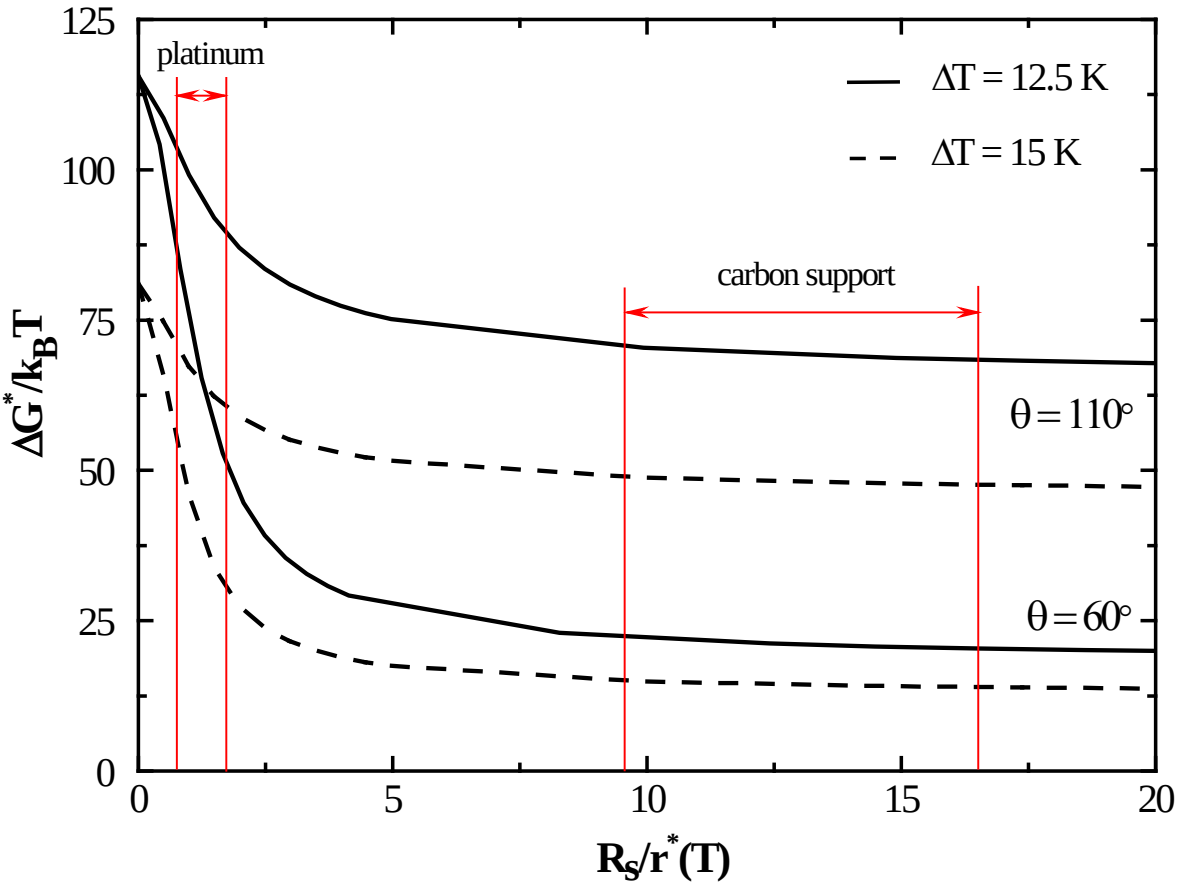

Figure 4B.1. Calculated dimensionless Gibbs-free energy of critical-nucleus formation, $\Delta G^* / k_B T$, versus dimensionless seed radius, $x^* = R_S / r^*(T)$, for ice/water/substrate contact angles of 60° and 110°, where $r^*(T)$ is the radius of a critical nucleus. Solid and dashed lines denote subcoolings of 12.5 K and 15 K, respectively. Arrows establish minimum and maximum dimensionless seed radii calculated for platinum and carbon within the PEMFC catalysts.

Chapter 5

Non-Isothermal Melting of Ice in the Gas-Diffusion Layer of a Proton-Exchange-Membrane Fuel Cell

T.J. Dursch, G.J. Trigub, J.F. Liu, C.J. Radke, A.Z. Weber, Non-isothermal melting of ice in the gas-diffusion layer of a proton-exchange-membrane fuel cell, Int. J. Heat Mass Trans. 67 (*2013*) *896-901.*

5.1. Abstract

Non-isothermal ice melting in the fibrous gas-diffusion layer (GDL) of a proton-exchange-membrane fuel cell (PEMFC) is investigated using differential scanning calorimetry (DSC). Non-isothermal ice-melting rates and ice-melting times are obtained from heat-flow measurements in water-saturated Toray GDLs at heating rates of 1, 2.5, 5, 10, and 25 K/min. In all cases, ice-melting times decrease nonlinearly with increasing heating rate. Nevertheless, melting temperatures remain at 272.9 ± 0.5 K and 272.7 ± 0.4 K for bulk ice and ice within the GDL, respectively, reiterating that melting is thermodynamic-based at a rate limited by heat transfer. The slight GDL ice melting-point depression is consistent with the Gibbs-Thomson equation for equilibrium melting using an average pore diameter of 30 μm. Ice-melting endotherms are predicted from overall DSC energy balances coupled with a moving-boundary Stefan problem, where an ice-melting front within a GDL propagates with volume-averaged properties through an effective medium. Agreement between DSC experiment and theory is excellent. The proposed model accurately predicts ice-melting endotherms for Toray GDLs with two ice saturations and for bulk ice. Further, a pseudo-steady-state analysis obtains an analytical expression for ice-melting time, which is controlled by the time for heat addition to the propagating solid/liquid interface. Significantly, the new expression elucidates parameters controlling ice melting and allows for better design of both GDL materials and heating strategies to enhance the success of PEMFC cold-start.

5.2. Introduction

Proton-exchange-membrane fuel cells (PEMFCs) show promise in automotive applications because of their high efficiency, high power density, and potentially low emissions. In successful automotive applications, PEMFCs permit rapid startup from sub-freezing temperatures, known as cold-start. In a PEMFC, reduction of oxygen to water occurs in the cathode catalyst layer (cCL). Under subfreezing conditions, water solidifies and hinders access of gaseous oxygen to the catalytic sites in the cCL, severely inhibiting cell performance [1, 2]. During cold-start, the time for recovering cell performance strongly depends on the rate of melting residual ice by reactive heat generation [3]. Elucidation of the mechanism and rate of ice melting within PEMFC porous media is, therefore, critical to rapid cell startup and high performance at low temperatures.

Because of cell failure under subfreezing conditions, much attention has been given to understanding cold-start fundamentals. To date, experimental studies of PEMFC cold-start primarily focus on characterizing overall low-temperature cell performance including:

degradation after freeze-thaw cycles [1], effects of cell material properties [2, 4-6], and *in-situ* visualization of ice formation [7]. Numerous studies show that the cell electrical potential decays rapidly at low temperatures due to ice formation at the reactive area of the cathode [1-8]. Currently, no studies focus on understanding the mechanism and rate of ice melting within PEMFC porous media. Recently, several PEMFC cold-start models have also been developed [3, 8-11]. These models, however, adopt empirical melting rate expressions from ice-saturated-soil literature [12, 13], since at this time one does not exist for PEMFC porous media.

In the past few decades, significant effort has been expended on understanding melting both experimentally and theoretically because of the enormous variety of applications, including thermal energy storage using phase-change materials [14-17], metal casting [18-20], and polymer processing and sintering [21-23]. Numerous studies focus on melting of bulk ice [24-26] and ice within porous media [27-29], especially soils, rocks, and clays, due to potential mechanical damage from frost heave. In nearly all cases [14-26], melting is described by a moving-boundary heat-transfer (Stefan) analysis. However, because the properties of fuel-cell materials differ considerably from soil media in wettability, pore size, and microstructure, proposed melting rates and mechanisms are not necessarily applicable.

This work measures and predicts non-isothermal ice melting in the fibrous GDL of a PEMFC. Ice melting is studied within the GDL because this layer is significantly ice saturated during PEMFC cold-start [3, 7, 10, 11]. We use differential scanning calorimetry (DSC) to obtain non-isothermal ice-melting rates and ice-melting times as functions of heating rate for a commercial Toray GDL with two ice saturations and for bulk ice. We predict ice-melting endotherms by solving overall DSC energy balances coupled with the moving-boundary Stefan problem, where an ice-melting front within a GDL propagates with volume-averaged properties through an effective medium. Additionally, we utilize a pseudo-steady-state analysis to obtain an analytical expression for the time for complete ice melting. Notably, this expression elucidates parameters controlling ice melting and allows for better design of both GDL materials and heating strategies to enhance success of PEMFC cold-start.

5.3. Materials and Methods

5.3.1. Sample Preparation:

Water-wetting TGP-H-060 carbon-paper GDLs were provided by Toray (Toray Corp., Tokyo, Japan). GDL samples were bored into 3.25-mm diameter circles and saturated with Ultrapure Milli-Q® (Millipore, Billerica, MA) distilled/deionized water in a home-built vacuum chamber for 1 h at 4.7 kPa. Following evacuation, excess surface water was removed by lightly blotting with Fisherbrand® weighing paper (Fisher Scientific, Pittsburgh, PA). GDL liquid-water saturations were controlled using a relative-humidity chamber [30]. Water content was determined gravimetrically; measured values were consistent with integrated peak areas generated from DSC. GDLs at two liquid-water saturations were studied: 20% and 85% [31]. Water loss by evaporation during DSC experiments was negligible. Additionally, capillary-pressure-saturation measurements showed that water does not drain from the GDLs under atmospheric pressure [32].

5.3.2. Differential Scanning Calorimetry:

A PerkinElmer 6000 DSC (PerkinElmer Inc., Waltham, MA) with a liquid-nitrogen chiller measured sample heat-flow rate over time. The DSC was calibrated as described

previously [31]. Nitrogen served as the purge gas at a flow rate of 20 mL/min. Water-saturated GDL samples, weighing between 1.4 and 2.2 mg, were placed into 20-µL PerkinElmer hermetically-sealed aluminum pans. For bulk-ice melting experiments, 8 or 19 µL of Ultrapure Milli-Q® distilled/deionized water was pipetted directly into 20-µL DSC pans. In all experiments, DSC pans were encircled by a 1-mm thick insulating polydimethylsiloxane (PDMS) ring to minimize radial heat loss. Non-isothermal melting was carried out over the temperature range of 273 to 300 K. Samples were placed into the DSC at 300 K, cooled to 235 K at 105 K/min, and held isothermally for 5 min. Following complete ice crystallization, samples were heated from 235 to 300 K at constant heating rates, β, of 1, 2.5, 5, 10, and 25 K/min. In all cases, $t = 0$ corresponds to the sample temperature, T_S, of 272 K.

5.4. Experimental Results

Figure 5.1 displays a typical melting endotherm of heat-flow rate, $\dot{Q}$ (mW), versus time, t, for bulk ice (8 µL) at a heating rate, β, of 10 K/min. For reference, furnace temperature, T_F, is plotted on the superior abscissa. The sample was heated at 10 K/min from 235 to 300 K. For clarity, heat-flow rate is shown only from 272 to 300 K. Melting commenced at 10 s (point A in Figure 5.1) corresponding to furnace and sample temperatures of 273.6 and 273.1 K, respectively. From point A, heat flow due to absorption of the enthalpy of melting is evident until complete melting is observed at point B, after which declining heat flow reflects the sensible heat necessary to raise the liquid-saturated sample temperature to the furnace temperature. Melting time, t_{melt}, is taken as that from melting onset to maximum heat-flow rate (point A to B), approximately 55 s in Figure 5.1.

Figure 5.2 shows measured melting endotherms of heat-flow rate versus time for bulk ice (8 µL) at heating rates, β, of 1 (inverted triangles), 2.5 (circles), 5 (triangles), 10 (squares), and 25 K/min (diamonds). Lines in Figure 5.2 are drawn according to theory discussed below. As β increases from 1 to 25 K/min, melting endotherms both narrow and reach greater peak heat-flow rates, consonant with identical water mass in each sample. Concurrently, the melting time, t_{melt}, decreases from 150 to 35 s. For all heating rates, however, the melting temperature is 272.9 ± 0.5 K corresponding to the melting point of bulk ice. This result suggests that melting is thermodynamic with a rate limited by heat transfer, in accordance with previous findings [14-29].

Similar measurements for two GDLs with varying ice saturation and a larger bulk ice volume (19 µL) were performed to quantify further the effect of β on the non-isothermal melting time, t_{melt}. Figure 5.3 plots non-isothermal melting time, t_{melt}, as a function of heating rate, β, for a Toray GDL with ice saturations of 80% (open diamonds) and 19% (open squares), and 8 µL (filled triangles) and 19 µL (filled circles) of bulk ice. Solid and dashed lines correspond to theory, as described below. In all cases, t_{melt} decreases monotonically with increasing β. At a given β, t_{melt} is longest for 19 µL of bulk ice and is shortest for the ice-saturated GDLs, corresponding to 1.2 µL and 0.3 µL of ice. For all β, the melting temperature of ice within the GDL is 272.7 ± 0.4 K (near bulk ice), consistent with a slight melting-point depression calculated from the Gibbs-Thomson relation with an average pore diameter of

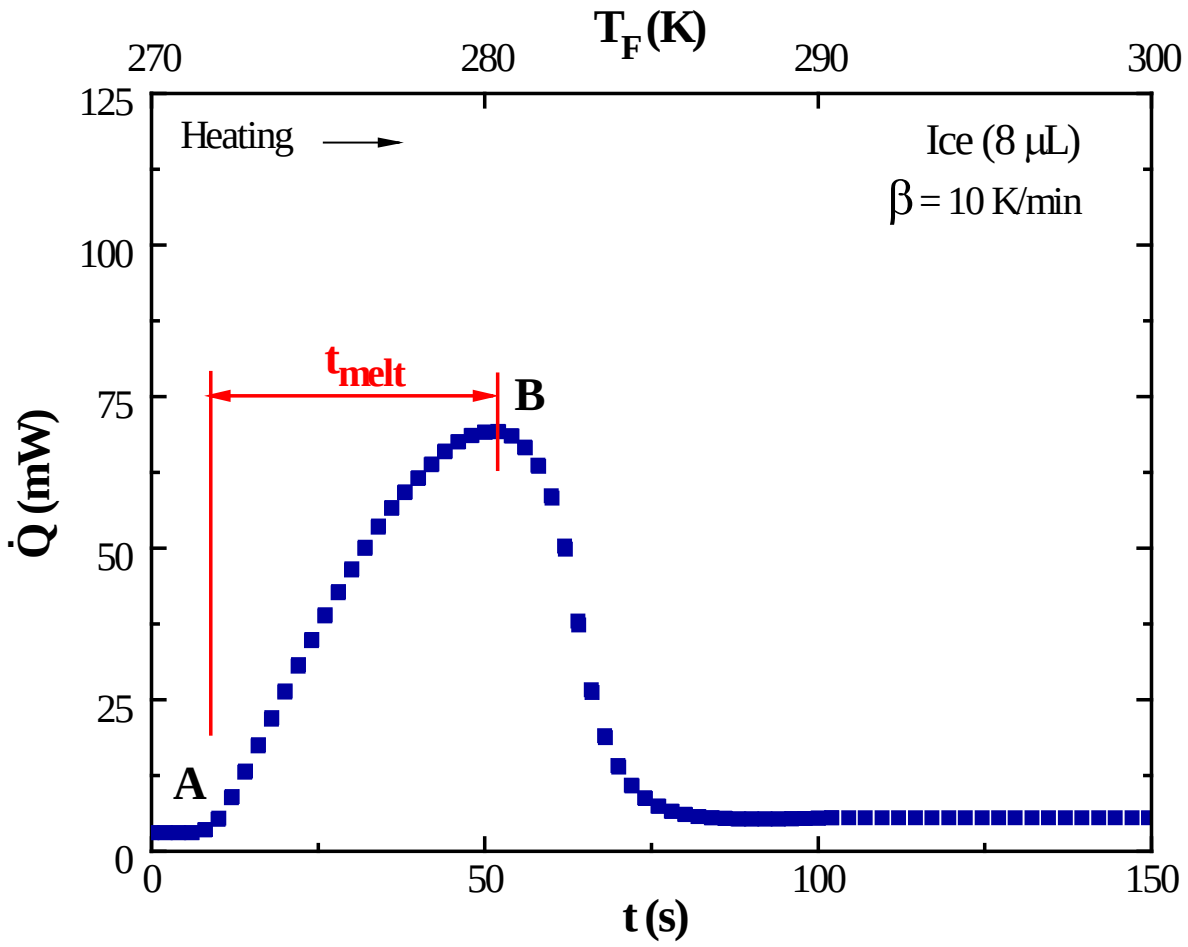

Figure 5.1. Typical non-isothermal melting endotherm of heat-flow rate, $\dot{Q}$, versus time, t, for bulk ice (8 μL) at a heating rate, β, of 10 K/min. A and B label the onset and completion of ice melting, respectively. The symbol t_{melt} defines the melting time. Furnace temperature, T_F, is shown in the upper abscissa.

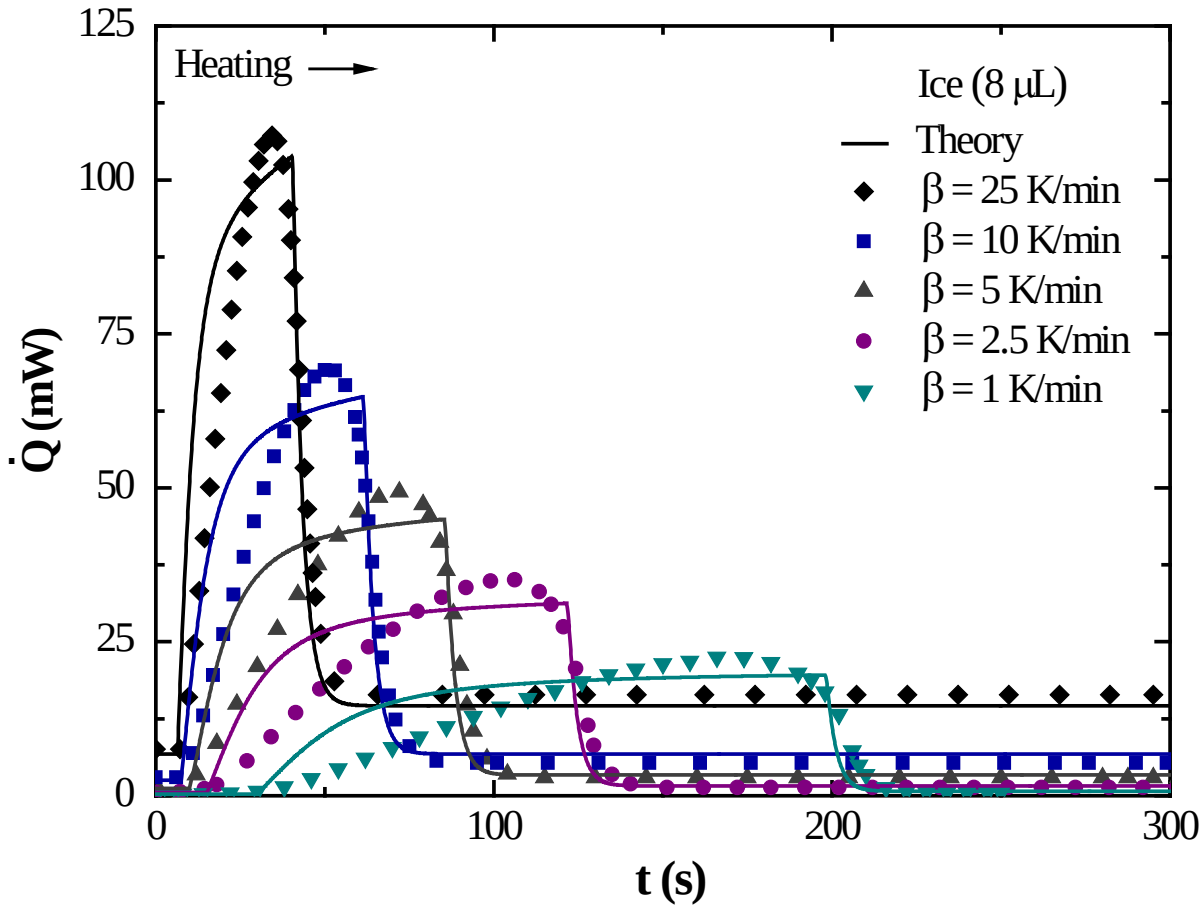

Figure 5.2. Non-isothermal melting endotherms, $\dot{Q}$ versus t, for bulk ice (8 µL) at heating rates, β, 1 (inverted triangles), 2.5 (circles), 5 (triangles), 10 (squares), and 25 K/min (diamonds). Lines are $\dot{Q}(t)$ predictions using equations 5.1-5.4.

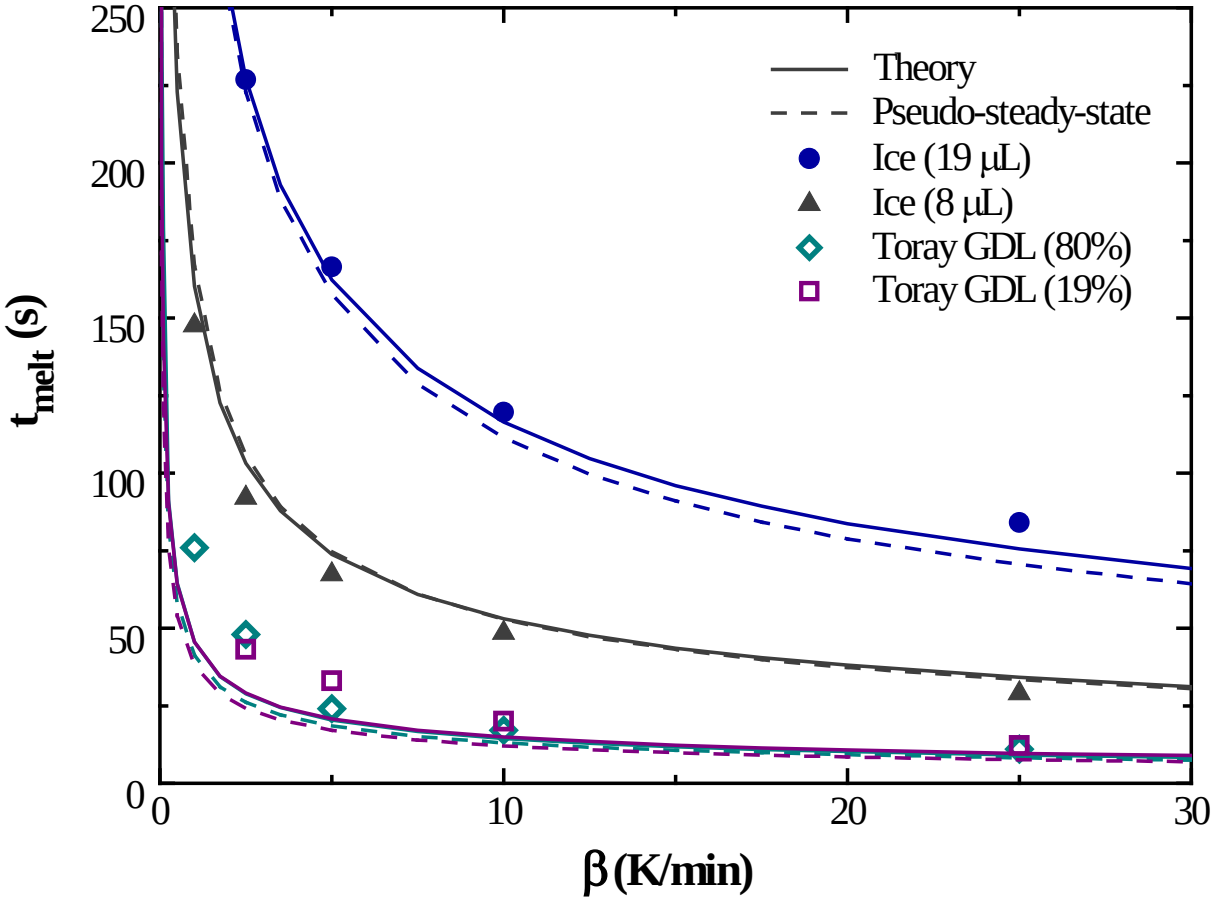

Figure 5.3. Non-isothermal melting time, t_{melt}, as a function of heating rate, β, for a Toray GDL with two ice saturations 80% (open diamonds) and 19% (open squares), and 8 (filled triangles) and 19 μL (filled circles) of bulk ice. Solid lines are calculated using equations 5.2-5.4, whereas dashed lines are calculated using equation 5.7.

30-μm [32]. This result indicates that the large pore diameters do not significantly alter the equilibrium melting temperature of ice within a GDL compared to that of bulk ice.

5.5. Non-isothermal DSC Theory

We desire quantitative prediction of DSC-measured ice-melting endotherms (i.e., heat-flow rate, $\dot{Q}$, versus time, t). DSC heat-flow rate and sample temperature, $T_S(x,t)$, are determined by solving overall energy balances coupled with the moving-boundary Stefan problem [33].

Figure 5.4 illustrates the simplified geometry for ice melting within an ice-saturated GDL of sample thickness L in a DSC pan insulated by a surrounding polydimethylsiloxane ring. At $x = 0$, heat supplied by the DSC furnace initiates ice melting at the equilibrium melting temperature, $T_S(\delta,t) = T_o$, where $\delta(t)$ denotes the time-dependent position of the advancing ice/water interface. For $x > \delta(t)$, sample temperature remains uniform at T_o during melting. For $x < \delta(t)$, however, $T_S(x,t)$ increases in time from heat supply by the DSC furnace. To establish the DSC-measured ice-melting endotherms, such as in Figure 5.2 (i.e., $\dot{Q}(t)$), $T_S(x,t)$ and $\delta(t)$ must be specified.

Heat transfer within a DSC has been thoroughly investigated [34-37]. DSC sample and reference pans are encased in a temperature-controlled furnace. Upon heating, the furnace temperature, $T_F(t)$, is increased at a constant programmed rate, here linear, $T_F(t) = T_{Fo} + \beta t$, where T_{Fo} is initial furnace temperature and β is heating rate (K/min). Instrument-reported heat-flow rate is proportional to the temperature difference between sample and reference pans [34]

$$\dot{Q}(t) = UA_p[T_R(t) - T_S(0,t)] \tag{5.1}$$

where U is the overall heat transfer coefficient, A_p is pan area in contact with the DSC platform, $T_R(t)$ is reference temperature, and $T_S(0,t)$ is sample temperature at the lower boundary of the sample pan in contact with the furnace.

As described previously [34], the product UA_p in equation 5.1 is obtained from DSC calibration using indium. Accordingly, $T_R(t)$ and $T_S(0,t)$ in equation 5.1 remain to be established. Following Eder [37], an overall energy balance describes the temperature of the reference pan

$$m_p \hat{C}_{p,p} \frac{dT_R(t)}{dt} = UA_p\left[T_F(t) - T_R(t)\right] \tag{5.2}$$

where m_p and $\hat{C}_{p,p}$ are pan mass and specific heat capacity, respectively.

To obtain $T_S(0,t)$, we adopt a 1-D moving-boundary Stefan problem [33], where a uniform liquid front propagates due to melting, at a rate limited by heat supply to the advancing solid/liquid interface. GDLs are highly porous carbon-fiber networks ($0.7 \le \varepsilon_o$ (porosity) ≤ 0.9

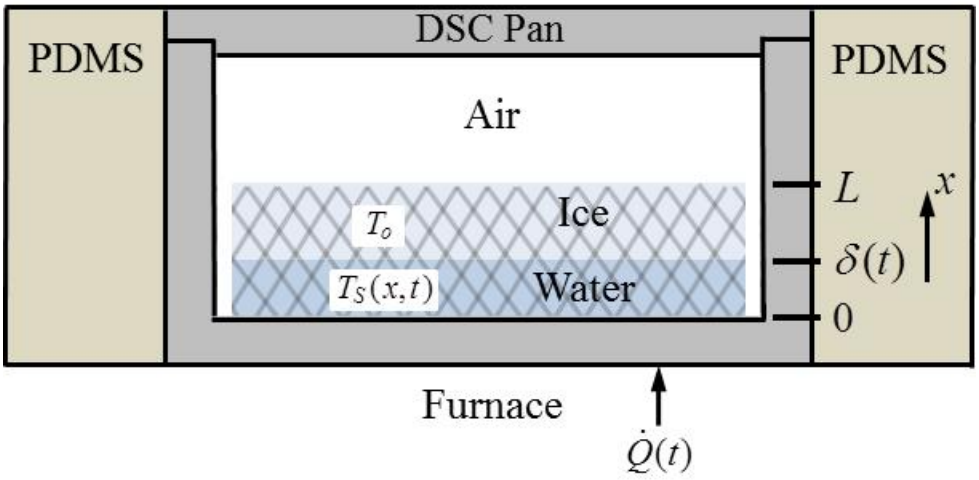

Figure 5.4. Schematic for the 1-D DSC geometry. Cross-hatching indicates presence of a GDL. Symbols $\dot{Q}(t)$ and $\delta(t)$ label DSC heat-flow rate and time-dependent position of the ice/water interface, respectively. PDMS represents a 1-mm thick insulating polydimethylsiloxane ring. Drawing is not to scale.

[31]) demanding that ice melts at a uniform equilibrium melting temperature, T_o. Accordingly, the progressing liquid front propagates with volume-averaged properties through an effective medium following a 1-D Stefan problem. $T_S(x,t)$ and $\delta(t)$ follow from liquid-phase and interfacial energy balances

$$\frac{\partial T_S(x,t)}{\partial t} = \alpha_{eff} \frac{\partial^2 T_S(x,t)}{\partial x^2} \qquad 0 < x < \delta(t) \tag{5.3}$$

and

$$\rho_L \Delta\hat{H}_f \varepsilon_o S_L \frac{d\delta(t)}{dt} = k_{eff} A_p \frac{\partial T_S(\delta,t)}{\partial x} \qquad x = \delta(t) \tag{5.4}$$

where ρ_L is liquid mass density, $\Delta\hat{H}_f$ is latent heat of fusion per unit mass of ice (taken as positive), ε_o is porosity (void volume per GDL volume), S_L is liquid-water saturation, and α_{eff} and k_{eff} are effective thermal diffusivity and conductivity, respectively. In equations 5.3 and 5.4, we neglect natural convection in the melted region of the effective medium (i.e., a low Rayleigh number [38], radial conduction due to a GDL diameter-to-thickness ratio of over 20, and heat supply through the insulating air gap surrounding the GDL due to large thermal resistance. Effective properties in equations 5.3 and 5.4 are calculated from liquid-phase, gas-phase, and carbon-fiber properties as $k_{eff} = S_L\varepsilon_o k_L + S_G\varepsilon_o k_G + (1-\varepsilon_o)k_C$ and $\alpha_{eff} = k_{eff}/(\rho\hat{C}_p)_{eff}$, where $(\rho\hat{C}_p)_{eff} = S_L\varepsilon_o\rho_L\hat{C}_{p,L} + S_G\varepsilon_o\rho_G\hat{C}_{p,G} + (1-\varepsilon_o)\rho_C\hat{C}_{p,C}$, and subscripts L, G, and C denote liquid, gas, and carbon fiber, respectively. Accordingly, for ice melting in a DSC pan, $\varepsilon_o = 1$ and $S_L = 1$, giving $k_{eff} = k_L$.

Equation 5.3 is solved numerically subject to the boundary conditions

$$UA_p\left[T_F(t) - T_S(0,t)\right] = k_{eff} A_p \frac{\partial T_S(0,t)}{\partial x} \tag{5.5}$$

and

$$T_S(\delta,t) = T_o\,. \tag{5.6}$$

Equation 5.5 specifies continuity of heat flux at the GDL/furnace boundary while equation 5.6 sets the advancing ice/water interface temperature equal to the equilibrium melting temperature, T_o.

5.5.1. Numerical solution:

To convert equations 5.3 and 5.4 from a time-dependent to a time-independent domain, a Landau transformation is adopted [24], in which a new spatial variable is defined as $\eta(x,t) \equiv x/\delta(t)$. Equations 5.1 and 5.2, and coordinate-transformed forms of equations 5.3 and 5.4 given in Appendix 5A, are solved numerically in Matlab R2010a (The Math Works Inc., Natick, MA) using finite differencing and Crank-Nicholson iteration to resolve nonlinearities with a tolerance of 10^{-7}, a time step of 10^{-2} s, and 50 mesh elements. The inversion scheme

BAND(j) solves resulting tridiagonal matrices [39]. In all cases, resulting $T_S(\eta,t)$ profiles are converted to the original coordinate systems $T_S(x,t)$ profiles based on calculated $\delta(t)$.

5.6. Discussion

5.6.1. Model Comparison to Experiment:

Figure 5.5 plots a representative sample-temperature profile, $T_S(x,t)$, calculated at times of 0, 40, 80, and 120 s for bulk ice (8 µL) heated at a rate of 2.5 K/min. From numerical solution of equations 5.3-5.6, $T_S(x,t)$ increases in time due to continued heat supply from the DSC furnace and resulting conduction through the liquid-phase. Accordingly, $\delta(t)$ advances non-linearly in time as ice continues to melt, at a rate limited by heat addition to the ice/water interface. Since the time for heat addition to the propagating solid/liquid interface is limiting compared to the time for heat conduction through the effective medium, sample temperature is linear with position, as given by equation 5B.3 of Appendix 5B. In all cases, $T_S(0,t)$ is used to calculate $\dot{Q}(t)$ following equation 5.1.

Lines in Figure 5.2 show predicted ice-melting endotherms of heat-flow rate, $\dot{Q}(t)$, versus time for bulk ice (8 µL) at heating rates of β =1, 2.5, 5, 10, and 25 K/min. All model parameters were independently evaluated and are listed in Table 5.1. Agreement is excellent between theory and experiment. With no adjustable parameters, the melting/heat transfer model quantitatively predicts $\dot{Q}(t)$ and t_{melt} for all β. Base-line heat-flow rate ($\dot{Q}(t)$, pre- and post-

Table 5.1. Model Parameters

	Aluminum Pan (*p*)	**Water (L)**	**Carbon Fibers (C)**	**Gas (G)**
$\hat{C}_p$ (J kg^{-1} K^{-1})	910 [40]	4210 [40]	710 [11]	1000 [40]
k (W m^{-1} K^{-1})	250 [40]	0.6 [40]	1.3 [41]	0.025 [40]
ρ (kg m^{-3})	2700 [40]	990 [40]	490	1.2 [40]
UA_p (W K^{-1})	0.035 [34]	_	_	_
A_p (mm^2)	9.6	_	_	_
$\Delta\hat{H}_f$ (kJ kg^{-1})	_	335.6 [40]	_	_
S_f	_	0.2, 0.85	_	0.8, 0.15
ε_o	_	_	0.8 [31]	_

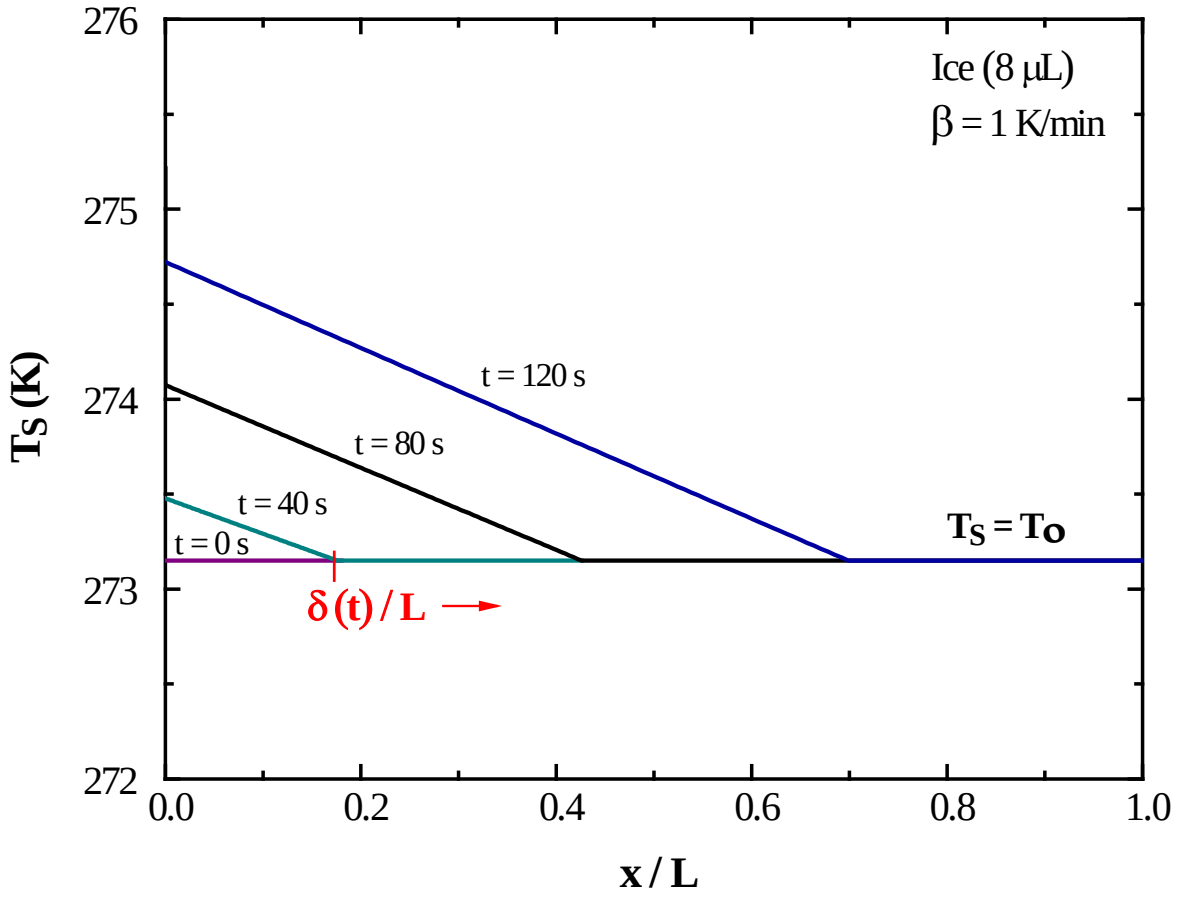

Figure 5.5. Calculated sample-temperature profile, $T_S(x,t)$, at times of 0, 40, 80, and 120 s for bulk ice (8 μL) heated at a rate of 2.5 K/min. Symbols T_o and $\delta(t)$ label the equilibrium melting temperature and normalized time-dependent position of the ice/water interface, respectively.

melting) increases linearly with β, as discussed elsewhere [34, 35]. As expected, $\dot{Q}(t)$ during melting increases more rapidly with increasing β due to greater heat supply at the sample/furnace interface. Thus, as β increases from 1 to 25 K/min, predicted t_{melt} decreases monotonically.

The proposed melting/heat transfer model also accurately predicts $\dot{Q}(t)$ and t_{melt} for two GDLs with different ice saturations and a for larger bulk ice volume (19 µL). Solid lines in Figure 5.3 are model predictions for t_{melt} (dashed lines are discussed below). For all β, melting kinetics of the ice-saturated GDLs are well predicted using the 1-D Stefan problem with volume-averaged properties (i.e., an effective medium). Significantly, this result confirms that GDL ice melts at T_o in the highly porous carbon-fiber matrix. Equations 5.3 and 5.4 constitute a new formalism to model melting of ice within GDLs of varying ice saturation during PEMFC cold-start (along with an appropriate heat-transfer model).

5.6.2. Pseudo-Steady-State Ice Melting:

To elucidate parameters controlling t_{melt}, specifically β, we utilize a pseudo-steady-state analysis [24]. Equations 5.3 and 5.4 contain two time scales: the time for heat conduction through the effective medium and the time for heat addition to the propagating solid/liquid interface. When sensible heat is negligible compared to latent heat, i.e., low effective Stefan numbers ($Ste_{eff} = (\rho \hat{C}_p)_{eff}(T_{Fo} - T_o)/\rho_L S_L \varepsilon_o \Delta \hat{H}_f$), the time for movement of the advancing solid/liquid interface is rate limiting. Accordingly, the effective-medium temperature profile is pseudo-steady as confirmed in Figure 5.5; Equation 5.3 simplifies considerably (see Appendix 5B). Under pseudo-steady-state conditions, pseudo-steady forms of equation 5.3 and equations 5.4, 5.5, and 5.6 are solved to obtain an explicit analytical expression for t_{melt}

$$t_{melt} = \left(\frac{\varepsilon_o \rho_L S_L \Delta \hat{H}_f}{\beta} \right)^{1/2} \left(\frac{L^2}{k_{eff}} + \frac{2L}{U} \right)^{1/2}, \tag{5.7}$$

where L denotes bulk-ice or GDL thickness. Figure 5.3 compares effective-medium (solid lines) and pseudo-steady (dashed lines) model-predicted t_{melt} versus β for two GDLs with varying ice saturation (19% and 80%) and two volumes of bulk ice (8 and 19 µL). As expected for bulk ice, t_{melt} decreases considerably with decreasing ice volume (V_I is related to sample thickness by $V_I = A_p L$). For the ice-saturated GDLs, however, t_{melt} is relatively insensitive to S_L, since effective thermal conductivity, k_{eff}, also decreases significantly with decreasing S_L. In all cases, excellent agreement indicates that equation 5.7 correctly scales with β, L, k_{eff}, S_L, and ε_o.

Equation 5.7 permits design of both GDL materials and heating strategies to enhance the success of PEMFC cold-start. For example, from equation 5.7 t_{melt} is decreased using thinner, less porous, more-thermally conductive GDLs. However, equation 5.7 reveals two limiting t_{melt} contributions: conduction through (L^2/k_{eff}) and heat transfer to ($2L/U$) the GDL, elucidating

that melting in even extremely thin, highly conductive GDLs is still limited by heat transfer to the GDL. Importantly, equation 5.7 allows optimization of t_{melt} through manipulation of material properties and heating strategies.

5.7. Conclusions

We determined ice-melting endotherms and ice-melting times as functions of heating rate in a fuel-cell gas-diffusion layer (GDL) using non-isothermal differential scanning calorimetry (DSC). Ice-melting rates were measured by DSC heat-flow dynamics for a commercial Toray GDL at two ice saturations and for bulk ice at heating rates of 1, 2.5, 5, 10, and 25 K/min. In all cases, ice-melting times decrease nonlinearly with increasing heating rate while melting temperatures remain 272.9 ± 0.5 K and 272.7 ± 0.4 K for bulk ice and ice within the GDL, respectively. Accordingly, melting is thermodynamic-based with a rate limited by heat transfer. The slight GDL ice melting-point depression is consistent with the Gibbs-Thomson equation using an average pore diameter of 30 μm. Importantly, this result suggests that large pore diameters do not significantly alter the equilibrium melting temperature of ice within GDLs.

Ice-melting endotherms and ice-melting times are well-predicted from overall DSC energy balances coupled with a moving boundary. Since ice melts at the equilibrium melting temperature within the highly-porous GDL, we assume that the ice-melting front propagates with volume-averaged properties through an effective medium following a 1-D Stefan problem. Agreement is excellent between theory and experiment. At all heating rates, the model accurately predicts ice-melting endotherms and ice-melting times for Toray GDLs with two ice saturations and bulk ice. To elucidate parameters controlling ice-melting times, we utilize a pseudo-steady-state analysis. For ice melting at low Stefan numbers, the time for heat addition to the propagating solid/liquid interface limits the process leading to an analytical expression for ice-melting time. Significantly, the proposed new expression allows for better design of both GDL materials and heating strategies to enhance the success of PEMFC cold-start.

5.8. List of Symbols

A_p	pan area containing DSC platform
k	thermal conductivity (W/m/K)
L	sample thickness (μm)
m	mass (kg)
$\dot{Q}$	heat-flow rate (mW)
S	saturation
Ste	Stefan number
T	temperature (K)
T_o	273.15 K
t	time (s)
U	overall heat transfer coefficient

Greek Letters

α thermal diffusivity (m^2/s)

β cooling rate (K/min)

δ time-dependent ice/water interface position

ε_o GDL porosity

η coordinate-transformed position in equations 5A.1 and 5A.2

ρ mass density (kg/m^3)

Subscripts

C carbon fibers

eff effective

F furnace

G gas

L liquid

o initial

I ice

p pan

R reference

S sample

5.9. Acknowledgements

This work was funded by the Assistant Secretary for Energy Efficiency and Renewable Energy, Office of Fuel Cell Technologies, of the U. S. Department of Energy under contract number DE-AC02-05CH11231.

5.10. References

[1] C. Chacko, R. Ramasamy, S. Kim, M. Khandelwal, M. Mench, Characteristic behavior polymer electrolyte fuel cell resistance during cold start, J. Electrochem. Soc. 155 (2008) B1145-B1154.

[2] K. Tajiri, Y. Tabuchi, F. Kagami, S. Takahashi, K. Yoshizawa, C.Y. Wang, Effects of operating and design parameters on PEFC cold start, J. Power Sources 165 (2007) 279-286.

[3] R. Balliet, J. Newman, Cold start of a polymer-electrolyte fuel cell I. Development of a two-dimensional model, J. Electrochem. Soc. 158 (2011) B927-B938.

[4] M. Oszcipok, D. Riemann, U. Kronenwett, M. Kreideweis, M. Zedda, Statistic analysis of operational influences on the cold start behavior of PEM fuel cells, J. Power Sources 145 (2005) 407-415.

[5] S. Ge, C.Y. Wang, Characteristics of subzero startup and water/ice formation on the catalyst layer in a polymer electrolyte fuel cell, Electrochimica Acta 52 (2007) 4825-4835.

[6] X.G. Yang, Y. Tabuchi, F. Kagami, C.Y. Wang, Durability of membrane electrode assemblies under polymer electrolyte fuel cell cold-start cycling, J. Electrochem. Soc. 155 (2008) B752-B761.

[7] Y. Ishikawa, H. Hamada, M. Uehara, M. Shiozawa, Super-colled water behavior inside polymer electrolyte fuel cell cross-section below freezing temperature, J. Power Sources 179 (2008) 547-552.

[8] L. Mao, C.Y. Wang, Y. Tabuchi, A multiphase model for cold start of polymer electrolyte fuel cells, J. Electrochem. Soc. 154 (2007) B341-B351.

[9] H. Meng, A PEM fuel cell model for cold-start simulations, J. Power Sources 178 (2008) 141-150.

[10] K. Jiao, X. Li, Three-dimensional multiphase modeling of cold start processes in polymer electrolyte membrane fuel cells, Electrochim. Acta 54 (2009) 6876-6891.

[11] R. Balliet, K.E. Thomas-Alyea, Water movement during freezing in a polymer-electrolyte-membrane fuel cell, J. Newman, ECS Trans. 16 (2008) 285-296.

[12] L. Bronfenbrener, E. Korin, Kinetic model for crystallization in porous media, Int. J. Heat Mass Trans. 40 (1997) 1053-1059.

[13] L. Bronfenbrener, E. Korin, Two-phase zone formation conditions under freezing of porous media, J. Crystal Growth 198 (1999) 89-95.

[14] A. Sharma, V.V. Tyagi, C.R. Chen, D. Buddhi, Review on thermal energy storage with phase change materials and applications, Renewable and Sustainable Energy Reviews 13 (2009) 318-345.

[15] B. Zalba, J. Marin, L.F. Cabeza, H. Mehling, Review on thermal energy storage with phase change: materials, heat transfer analysis, and applications, Appl. Thermal Engineering 23 (2003) 251-283.

[16] P. Lamberg, R. Lehtiniemi, A-M. Henell, Numerical and experimental investigation of melting and freezing processes in phase change material storage, Int. J. of Therm. Sciences 43 (2004) 277-287.

[17] F.L. Tan, S.F. Hosseinizadeh, J.M. Khodadadi, L. Fan, Experimental and computational study of constrained melting of phase change materials (PCM) inside a spherical capsule, Int. J. Heat Mass Trans. 52 (2009) 3464-3472.

[18] H. Hu, S.A. Argyropoulos, Mathematical modeling of solidification and melting: a review, Modelling. Simul. Mater. Sci. Eng. 4 (1996) 371-396.

[19] A.F. Albu, V.I. Zubov, Mathematical modeling and study of the process of solidification in metal casting, Comp. Math. Math. Phys. 47 (2007) 844-862.

[20] F. Stella, M. Giangi, Melting of a pure metal on a vertical wall: numerical simulation, Num. Heat Trans. Part A 38 (2000) 193-208.

[21] J. Qu, G. Zeng, Y. Feng, G. Jin, H. He, X. Cao, Effect of screw axial vibration of polymer melting process in single-screw extruders, J. Appl. Poly. Sci. 27 (2006) 3860-3876.

[22] B. Crist, Small-angle X-ray scattering and polymer melting: a model study, J. Poly. Sci. Part B: Poly. Physics 39 (2001) 2454-2460.

[23] A. Greco, A. Maffezzoli, Polymer melting and polymer powder sintering by thermal analysis, J. Therm. Anal. Calorimetry 72 (2003) 1167-1174.

[24] V. Alexiades, A.D. Solomon, Mathematical modeling of melting and freezing processes, Hemisphere Publishing, Washington, D.C., 1993. pp. 155-160.

[25] T. Kousksou, A. Jamil, Y. Zeraouli, J.-P. Dumas, DSC study and computer modeling of the melting process in ice slurry, Thermochimica Acta 448 (2006) 123-129.

[26] T. Hirata, Y. Makino, Y. Kaneko, Analysis of close-contact melting of octadecane and ice inside isothermally heated horizontal rectangular capsule, Int. J. Heat Mass Transfer 34 (1991) 3097-3106.

[27] K. O'Neill, The physics of mathematical frost heat models: a review, Cold Regions Science and Technology 6 (1983) 275-291.

[28] X. Zhang, T.H. Nguyen, Melting of ice in a porous medium heated from below, Int. J. Heat Mass Transfer 34 (1991) 389-405.

[29] M. Kaviany, Principles of Heat Transfer in Porous Media, second ed., Springer-Verlag, New York, 1995. pp. 656-674.

[30] G.S. Hwang, A.Z. Weber, Effective-diffusivity measurement of partially-saturated fuel-cell gas-diffusion layers, J. Electrochem. Soc. 159 (2012) F683-F692.

[31] T.J. Dursch, M.A. Ciontea, C.J. Radke, A.Z. Weber, Isothermal ice crystallization kinetics in the gas-diffusion layer of a proton-exchange-membrane fuel cell, Langmuir 28 (2012) 1222-1234.

[32] J.T. Gostick, M.A. Ioannidis, M.W. Fowler, M.D. Pritzker, Wettability and capillary behavior of fibrous gas diffusion media for polymer electrolyte membrane fuel cells, Journal of Power Sources 194 (2009) 433-444.

[33] H.S. Carlsaw, J.C. Jaeger, Conduction of Heat in Solids, second ed., Oxford University Press, Oxford, 1959 (Chapter 11).

[34] T.J. Dursch, M.A. Ciontea, G.J. Trigub, C.J. Radke, A.Z. Weber, Pseudo-isothermal ice-crystallization kinetics in the gas-diffusion layer of a fuel cell from differential scanning calorimetry, Int. J. Heat and Mass. Trans. 60 (2013) 450-458.

[35] G.W.H. Hohne, W.F. Hemminger, H.J. Flammersheim, Differential scanning calorimetry, second ed., Springer, Heidelberg, 2003. pp. 31-63.

[36] G. Lamberti, Importance of heat transfer phenomena during DSC polymer solidification, Int. J. Heat Mass Trans. 41 (2004) 23-31.

[37] C.H. Wu, G. Eder, H. Janeschitz-Kriegl, Polymer crystallization dynamics, as reflected by differential scanning calorimetry. Part 2: Numerical simulations, Colloid. Polym. Sci. 271 (1993) 1116-1128.

[38] W.M. Deen, Analysis of Transport Phenomena, first ed., Oxford University Press 1998 pp. 488-493

[39] J. Newman, K.E. Thomas-Alyea, Electrochemical Systems, third ed., John Wiley & Sons, 2004 pp. 614-619.

[40] F.P. Incropera, D.P. Dewitt, T.L. Bergman, A.S. Lavine, Fundamentals of Heat and Mass Transfer, sixth ed., John Wiley & Sons, 2007 pp. 928-951.

[41] E. Sadeghi, N. Djilali, M. Bahrami, Effective thermal conductivity and thermal contact resistance of gas diffusion layers in proton exchange membrane fuel cells. Part 1: Effect of compressive load, J. Power Sources 196 (2011) 246-254.

Appendix 5A. Coordinate-Transformed Equations

To overcome the ice-melting moving boundary, we define the new dimensionless variable $\eta(x,t) \equiv x/\delta(t)$ [24]. Coordinate-transformed equations 5.3 and 5.4 are

$$\delta^2(t)\frac{\partial T_S(\eta,t)}{\partial t} = \alpha_{eff}\frac{\partial^2 T_S(\eta,t)}{\partial \eta^2} + \delta(t)\eta\frac{\partial T_S(\eta,t)}{\partial \eta}\frac{d\delta(t)}{dt} \qquad 0<\eta<1 \qquad (5A.1)$$

and

$$\rho_L \Delta\hat{H}_f \varepsilon_o S_L \delta(t)\frac{d\delta(t)}{dt} = k_{eff}\frac{\partial T_S(1,t)}{\partial \eta}. \qquad \eta = 1 \qquad (5A.2)$$

Eq. (A1) is subject to the coordinate-transformed boundary conditions

$$UA_p\delta(t)\left[T_F(t) - T_S(0,t)\right] = k_{eff}A_p\frac{\partial T_S(0,t)}{\partial \eta} \qquad (5A.3)$$

and

$$T_S(1,t) = T_o. \qquad (5A.4)$$

Appendix 5B. Pseudo-Steady-State Ice Melting

To elucidate the limiting melting time scale, equations 5.3 and 5.4 are non-dimensionalized to give

$$Ste_{eff}\frac{\partial T_S^*(x^*,t^*)}{\partial t^*} = \frac{\partial^2 T_S^*(x^*,t^*)}{\partial x^{*2}} \qquad (5B.1)$$

and

$$-\frac{d\delta^*(t^*)}{dt^*} = \frac{\partial T_S^*(\delta^*,t^*)}{\partial x^*}, \qquad (5B.2)$$

where $x^* = \frac{x}{L}$, $t^* = Ste_{eff}\,\frac{\alpha_{eff}\,t}{L^2}$, $T_S{}^* = \frac{T_S - T_o}{T_{Fo} - T_o}$, $\delta^* = \frac{\delta}{L}$, and $Ste_{eff} = \frac{(\rho\hat{C}_p)_{eff}\,(T_{Fo} - T_o)}{\rho_L S_L \varepsilon_o \Delta\hat{H}_f}$ is the liquid-phase Stefan number within the effective medium, and T_{Fo} is furnace temperature at the melting onset. When sensible heat is negligible compared to latent heat, $Ste_{eff} << 1$. For ice melting within our fibrous GDL, Ste_{eff} is at most equal to 0.08 (for $T_{Fo} - T_o = 1$ K at $\beta = 25$ K/min). Thus, the left side of equation 5B.1 is neglected. Accordingly, equation 5B.1 solves analytically with boundary conditions $T_S{}^*(\delta^*, t^*) = 0$ and $Bi_{eff}\left[T_F^*(t^*) - T_S^*(0,t^*)\right] = \partial T_S^*(0,t^*)/\partial x^*$ to give

$$T_S{}^*(x^*, t^*) = \frac{Bi_{eff}\,T_F^*(t^*)}{1 + Bi_{eff}\,\delta^*}\left[\delta^* - x^*\right], \tag{5B.3}$$

where $Bi_{eff} = UL/k_{eff}$ is effective-medium Biot number and $T_F{}^*(t^*) = (T_F(t) - T_o)/(T_{Fo} - T_o)$. To solve for t_{melt}, equation 5B.2 is integrated from 0 to δ^*, with $T_F(t) = T_{Fo} + \beta t$ and $T_S^*(x,t)$ given by equation 5B.3, resulting in dimensional form

$$k_{eff}\,\delta + \frac{U\delta^2}{2} = \frac{Ste_{eff}\,\alpha_{eff}\,U}{(T_{Fo} - T_o)}\left[(T_{Fo} - T_o)t + \frac{\beta}{2}t^2\right]. \tag{5B.4}$$

Since $\beta t^2/2 >> (T_{Fo} - T_o)t$ and $\delta(t_{melt}) = L$, equation 5B.4, after rearrangement, reduces to equation 5.7 of the text.

Chapter 6

Conclusion

6.1. Summary

To be successful in automotive applications, proton-exchange-membrane fuel cells (PEMFCs) must permit rapid startup with minimal energy from subfreezing temperatures [1-4]. Achieving such startup is difficult in practice, due to potential flooding, sluggish reaction kinetics, durability loss, and rapid ice crystallization [5-8]. Despite its importance, few studies focus on the fundamentals of ice formation during cold-start. A limited fundamental understanding of the role of ice-crystallization kinetics during PEMFC cold-start impedes progress in developing procedural strategies and advanced materials for improved cell performance at subfreezing temperatures. In an effort to advance knowledge in this field, this thesis focuses on the rate of ice-crystallization kinetics in water-saturated PEMFC porous media and on the role of ice-crystallization kinetics during PEMFC cold-start.

Differential scanning calorimetry (DSC) introduced in Chapters 2-4 provides new understanding of ice-crystallization kinetics in water-saturated PEMFC porous media. To understand what parameters govern the kinetics of ice crystallization in gas-diffusion (GDLs) and catalyst layers (CLs), the dependence of ice-crystallization and ice-nucleation rates on subcooling, cooling rate, and surface wettability was investigated. Subcooling is the most important driver of ice formation, and, therefore, plays a central role in PEMFC cold-start. To obtain an expression for the rate of ice formation, a nonlinear ice-crystallization rate expression was developed from the Johnson-Mehl-Avrami-Kolmogorov (JMAK) framework, in which the heat-transfer-limited growth rate was determined from the moving-boundary Stefan problem. Predicted ice-crystallization rates agree well with experiment. Validated rate expressions are thus available for predicting ice-crystallization kinetics in GDLs and CLs.

Membrane-electrode assembly (MEA) cold-start experiments featured in Chapter 4 measure MEA cell-failure time during isothermal galvanostatic cold-start. Using a simplified PEMFC isothermal cold-start continuum model, MEA cell-failure times predicted using the newly obtained rate expressions are compared to those predicted using a traditional thermodynamics-based approach. From this comparison, conditions were identified under which including ice-crystallization kinetics is critical and to elucidate the impact of freezing kinetics on low-temperature PEMFC operation. The numerical model illustrates that cell-failure times increases with increasing temperature due to a longer required time for ice nucleation. Hence, ice-crystallization kinetics is critical when induction times are long (i.e., in the “nucleation-limited" regime for $273 > T > 263$ K). Cell-failure times predicted using ice-freezing kinetics agree well with the isothermal MEA cold-start experimental results. These findings demonstrate a significant departure from cell-failure times predicted using a thermodynamics-based approach.

Experiments on ice melting in Chapter 5 measure ice-melting rates in water-saturated gas-diffusion layers with careful attention to heat transfer and melting physics. Our findings demonstrate that melting is thermodynamics-based with a rate limited by heat transfer. As a result, ice-melting endotherms are well predicted from overall DSC energy balances coupled with a moving-boundary Stefan problem, where an ice-melting front within a GDL propagates with volume-averaged properties through an effective medium. Importantly, the newly proposed

model elucidates parameters controlling ice melting and allows for better design of both GDL materials and heating strategies to aid PEMFC cold-start.

6.2. Future Work

Despite the important new information on ice-crystallization kinetics during PEMFC cold-start in Chapters 2-4, questions still remain. Fortunately, there are several ways in which the framework developed in the present work can be expanded to improve cell performance at subfreezing temperatures. In this section, we present a few examples which are thought to be high priority.

6.2.1. PEMFC Cold-Start Modeling and Experiments:

In Chapter 4, a simplified PEMFC isothermal cold-start continuum model is presented to validate ice-crystallization kinetics in PEMFCs. As discussed in Appendix 4A, however, the proposed cold-start model contains several simplifying assumptions. For example, the cold-start model assumes a uniform current density in the cathode CL and neglects water transport and freezing in both the anode and PEM. Clearly, more involved cold-start models (e.g., Balliet and Newman [6,9]) must be modified to include ice-crystallization kinetics. Further MEA cold-start experiments are also required to validate ice-crystallization kinetics over a range of PEMFC operating conditions. Two examples discussed in Chapter 4 are: (1) repeated MEA cell-failure time measurements at a given subcooling to investigate ice-crystallization statistics, and (2) MEA cell-failure time measurements as a function of current density. Further research coupling cold-start modeling and experiments could provide valuable insights into procedural strategies and materials design for improved PEMFC cold-start performance.

6.2.2. Ice-Crystallization Kinetics in State-of-the-Art Materials:

In Chapters 2-4, validated ice-crystallization rate expressions are posed for predicting ice formation in traditional PEMFC porous media. The ice-formation model focuses on conventional gas-diffusion and catalyst layers; however, nucleation and growth kinetics are readily extended to other non-traditional GDLs and CLs. Examples include: carbon cloth GDLs, Freudenberg GDLs, and “state-of-the-art materials” such as nanostructured thin-film (NSTF) CLs. Of particular importance are NSTF CLs, which were designed to reduce precious-metal loadings [10]. These CLs contain platinum-coated “whiskers” of a stable organic pigment and are 20-40 times thinner than conventional platinum-on-carbon porous CLs. Unfortunately, a disadvantage of decreased thickness is the tendency to flood/plug during low-temperature operation due to diminished water/ice-uptake capacity. Due to the relative scarcity of knowledge about the mechanisms and kinetics of ice crystallization in non-traditional PEMFC porous media, much remains to be discovered.

6.2.3. Effect of External Mechanical Vibrations on Ice-Nucleation Rates:

In Chapters 2-4, ice-nucleation rates are obtained from repeated induction-time measurements in a differential scanning calorimeter that is, for the most part, isolated from mechanical vibrations. In Appendix 6A, we present preliminary experiments demonstrating that applied mechanical vibrations can significantly enhance ice-nucleation rates, especially at low subcoolings. Additional research is necessary to investigate the effect of mechanical vibrations on ice-nucleation rates in PEMFC porous media.

6.3. References

[1] V. Mehta, J.S. Cooper, Review and analysis of PEM fuel cell design and manufacturing, J. Power Sources 114 (2003) 32-53.

[2] B. Smitha, S. Sridhar, A.A. Khan, Solid polymer electrolyte membranes for fuel cell applications - a review, J. Membrane Sci. 259 (2005) 10-26.

[3] H. Li, Y. Tang, Z. Wang, Z. Shi, S. Wu, D. Song et al., A review of water flooding issues in the proton exchange membrane fuel cell, J. Power Sources 178 (2008) 103-117.

[4] W. Schmittinger, A. Vahidi, A review of the main parameters influencing long-term performance and durability of PEM fuel cells, J. Power Sources 180 (2008) 1-14.

[5] Hydrogen, Fuel Cells & Infrastructure Technologies Program; Multi-Year Research, Development and Demonstration Plan, U.S. Department of Energy, 2007.

[6] R. Balliet, J. Newman, Cold start of a polymer-electrolyte fuel cell I. Development of a two-dimensional model, J. Electrochem. Soc. 158 (2011) B927-B938.

[7] K. Tajiri, Y. Tabuchi, F. Kagami, S. Takahashi, K. Yoshizawa, C.Y. Wang, Effects of operating and design parameters on PEFC cold start, J. Power Sources 165 (2007) 279-286.

[8] T.J. Dursch, G.J. Trigub, R. Lujan, J.F. Liu, R. Mukundan, C.J. Radke, A.Z. Weber, Ice-crystallization kinetics in the catalyst layer of a proton-exchange-membrane fuel cell, J. Electrochem. Soc. 161 (2014) F199-F207.

[9] R. Balliet, J. Newman, Cold start of a polymer-electrolyte fuel cell III. Optimization of operational and configurational parameters, J. Electrochem. Soc. 158 (2011) B948-B956.

[10] R. Balliet, J. Newman, Cold-start modeling of a polymer-electrolyte fuel cell containing an ultrathin cathode, ECS Trans. 41 (2011) 201-220.

Appendix 6A. Effect of External Mechanical Vibrations on Ice-Nucleation Rates

T.J. Dursch, G.J. Trigub, J.F. Liu, C.J. Radke, A.Z. Weber, Effect of External Vibrations on Non-Isothermal Ice-Nucleation Rates, AIChE Annual Meeting, Nov. 5th, 2013, San Francisco, CA.

Chapters 2-4 demonstrate that ice-nucleation rates can be obtained from DSC induction-time measurements. In nearly all cases, large driving forces (e.g., subcoolings of 10-30 K in Figures 2.6 and 4.2) are required for sufficiently large nucleation rates and, consequently, measurable induction times (within experimental limitations). In this appendix, we study the effect of an external driving force, specifically, applied mechanical vibrations, on ice-nucleation rates of bulk water. Preliminary results show that external vibrations can significantly enhance ice-nucleation rates, especially at low subcoolings when induction times are long.

Appendix 6A.1. Mechanical-Vibration Apparatus:

Figure 6A.1 schematically illustrates the experimental mechanical-vibration apparatus. 10-100 µL of distilled/deionized (DDI) water, placed in a thermally insulating Plexiglas cylinder (inner diameter of 1 cm with a wall thickness of 3 cm) mounted on a thermally conductive aluminum disc, was cooled from below by a copper heat exchanger containing a recirculating water-ethylene glycol mixture. To induce vibrations in the DDI water, an aluminum or copper cylindrical weight (3.1 cm in diameter and 9.5 cm in height) was released from heights ranging

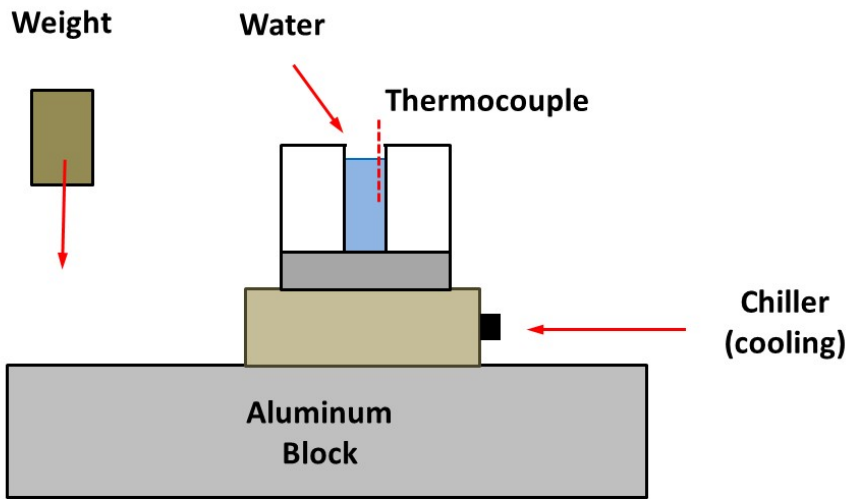

Figure 6A.1. Schematic for the mechanical-vibrations apparatus. Drawing is not to scale.

from 2.5 to 30 cm onto an aluminum block supporting the Plexiglas cylinder and copper heat exchanger. In all cases, the cylindrical weight was released every 5 s, 4 cm from the Plexiglas cylinder. Similar to DSC experiments, the water (sample) temperature was measured until complete ice crystallization. Here, the thermocouple was immersed in the water and affixed to the Plexiglas cylinder interior. As in Section 3.3.2, the non-isothermal induction time is defined as the time elapsed between when the sample temperature reaches 273 K and the onset of crystallization.

Appendix 6A.2. Experimental Results:

Figure 6A.2 displays measured induction times as a function of subcooling for 50 μL of bulk water with (open symbols) and without (filled symbols) applied mechanical vibrations. Dotted lines are drawn from classical nucleation theory extended to include work input from mechanical vibrations, as discussed below. Several features are salient. Induction times follow trends expected from classical nucleation theory, as detailed in Chapters 2-4. For example, induction times follow a Poisson distribution and monotonically decrease with increasing subcooling. Importantly, in all cases, work input from mechanical vibrations yields substantially shorter induction times (and therefore, larger ice-nucleation rates), dramatically so at low subcoolings. We report the maximum work input from mechanical vibrations as the gravitational potential energy, $PE = mgh$, of the dropped weight.

Appendix 6A.3. Discussion:

To investigate the dependence of induction time on mgh in Figure 6A.2, mechanical work was done on the system in three ways: (1) a copper cylinder was released from a set height, setting a potential energy of PE = 0.05 J; (2) an aluminum cylinder was released a larger height than the copper cylinder, such that that the potential energy remained at a constant PE = 0.05 J; and (3) the aluminum cylinder was released from half the height of the copper cylinder to halve potential energy, PE = 0.001 J.

No theory is currently available to predict the role of vibrations in ice nucleation. We postulate that mechanical work done on the bulk-water system enhances ice nucleation by reducing the Gibbs-free energy barrier of critical-nucleus formation (ΔG^*). Accordingly, we define an effective Gibbs-free energy barrier, ΔG^*_{eff}, as ΔG^* less a fraction of the maximum gravitational potential energy, $fmgh$, or

$$\Delta G^*_{eff} = \Delta G^* - fmgh \tag{6A.1}$$

where f represents the fraction of gravitational potential energy input into the bulk water from the applied vibrations.

By way of example, Figure 6A.3 plots the calculated dimensionless Gibbs-free energy barrier of critical-nucleus formation, plotted as $\ln[\left|\Delta G^*_{eff} / k_B T_o\right| + 1]$, versus subcooling for ice nucleation in bulk water with work input from mechanical vibrations. Similar to Figure 6A.2, Figure 6A.3 reveals that mechanical vibrations significantly decreases ΔG^*_{eff} (i.e., enhances ice nucleation) at low subcoolings $\Delta T < 5$ K. Dotted lines in Figure 6A.2 are drawn using equation 6A.1 with f taken as a constant value of 10^{-21}. In all cases, agreement is excellent, indicating that measured induction times are qualitatively predicted by classical nucleation theory extended

to account for work input from mechanical vibrations. Unfortunately, the miniscule value of f suggests that only an extremely small fraction of the maximum gravitational potential energy is transferred to the liquid water. Future work hinges upon design of an apparatus that allows for precise measurement of the actual work done on the bulk-water system.

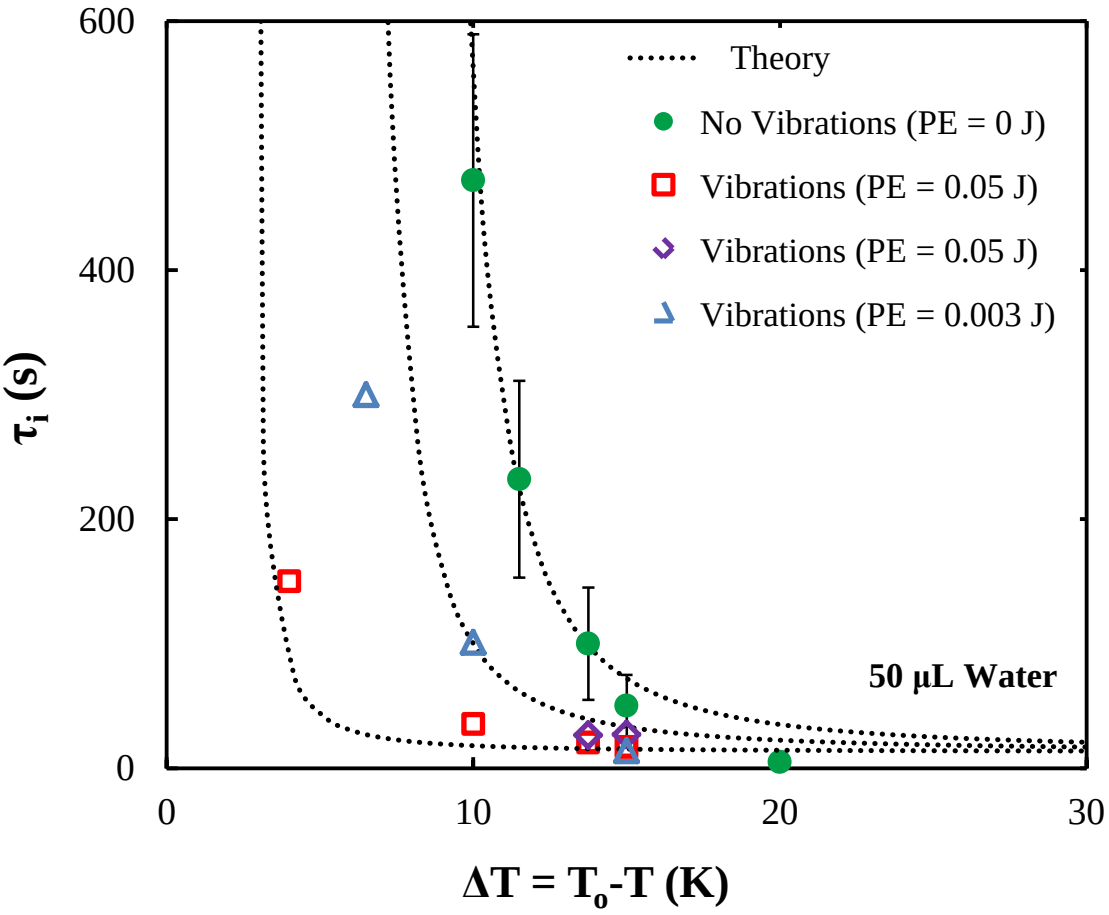

Figure 6A.2. Induction time as a function of subcooling for 50 µL of bulk water with (open symbols) and without (filled symbols) applied mechanical vibrations. Typical error bars indicate the maximum range of observed induction times (n = 6). Dotted lines are drawn from classical nucleation theory extended to include work input from mechanical vibrations.

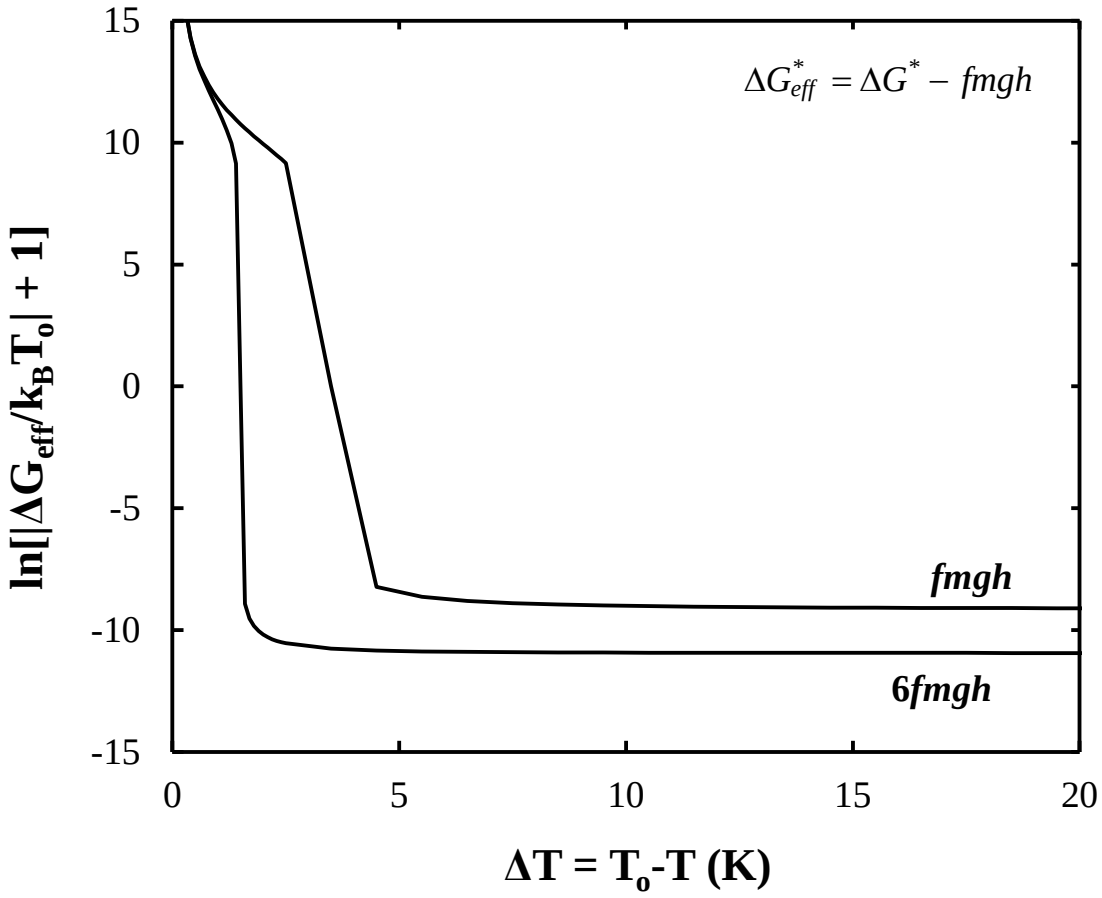

Figure 6A.3. Calculated dimensionless effective Gibbs-free energy of critical-nucleus formation, $\Delta G^*_{eff} / k_B T_o$, versus subcooling for ice nucleation in bulk water with work input from mechanical vibrations. *f* represents the fraction of gravitational potential energy input into the bulk water from the applied vibrations.